Temperature dependent aspects of the Compact High Energy Camera (CHEC-S) Front-End Electronic (FEE) calibration

Master's Thesis in Physics

Presented by
Johannes Schäfer
12.03.2019

Erlangen Centre for Astroparticle Physics
Physikalisches Institut II
Friedrich-Alexander-Universität Erlangen-Nürnberg

Supervisor: Prof. Dr. Stefan Funk

Abstract

The Compact High Energy Camera (CHEC) has been developed for CTA and its use in one of the proposed telescope designs is still under discussion. Its newest iteration (CHEC-S) features silicon photomultipliers as part of the signal chain. The TeV Array Readout with GSa/s sampling and Event Trigger (TARGET) Application Specific Integrated Circuit (ASIC) is a key component of the camera trigger- and data-path. These TARGET-ASICs are part of the Frond-End Electronic modules of which 32 are installed in CHEC-S. During operation, temperatures between $\approx 22°C$ - $46°C$ are measured for these within the camera. This poses a problem for the calibration of the modules, that has been performed at a fixed temperature of $23°C$. Within the scope of this thesis, a temperature dependency of the transfer-functions is observed with deviations exceeding 80 Analog-to-Digital-Converter (ADC)-counts in a temperature range between $20°C$ - $50°C$. The effects of these deviations on the fractional charge resolution of CHEC-S is estimated and results indicate that modules may not fulfill the CTA requirement when no correction for the temperature dependent transfer-function is applied. Also peaks in the charge spectrum are estimated to shift up to 16.90% depending on the illumination level due to the observed temperature effects. The temperature dependency of the transfer-functions could partly be traced back to the Wilkinson ADC circuit where a shift of the Wilkinson-ramp is observed. By shifting the Wilkinson-ramp, a mean residual relative deviation of below 5% is achieved in the above mentioned temperature range. Two other methods for correcting this effect are tested and proven to be effective. With applied correction the modules again fulfill the requirement even after a temperature change and the deviation is greatly reduced. An additional investigation of the timing resolution of CHEC-S shows an expected improvement of the timing resolution with illumination levels. The requirement set for CTA is fulfilled for all observed illumination levels.

Contents

1 Introduction

Gamma-ray astronomy is a very interesting field of astro-particle physics to study Very High-Energy (VHE) events in the universe. These manifest themselves in form of gamma-radiation (photons). Gamma-ray astronomy promises answers to interesting astrophysical questions regarding the origin and role of VHE photons and processes that happen near extreme objects such as neutron stars or black holes. However, detection of VHE photons is not an easy task. To this end, Imaging Air Cherenkov Telescopes (IACTs) have been developed. These image so called Cherenkov-flashes which are produced by the interaction between a VHE (primary) photon and the atmosphere [1, 2]. However, Cherenkov-flashes are very brief events, lasting only a few nanoseconds. Therefore, highly specialized and fast cameras are required for imaging. One of the most recent designs is the Compact High Energy Camera with Silicon photo-multipliers (CHEC-S) developed for the Cherenkov Telescope Array (CTA). An introduction to and overview of the concept of Cherenkov-flashes, CTA and CHEC-S is provided in the following Sections.

1.1 Cherenkov radiation

In this section a brief introduction to Cherenkov radiation is provided and the resulting phenomenon of Cherenkov-flashes and their connection with IACTs is explained. A primary photon ($E > 20\,\mathrm{GeV}$ [1]) that enters the atmosphere produces a electron-positron pair via pair-production in the vicinity of an atmospheric atomic nucleus. The resulting particles can travel faster than the local speed of light in the medium. This results in the emission of optical blue Cherenkov-light. The emission angle θ_c of this light depends on the refraction index n of the medium as well as the speed β of the particle. θ_c is calculated as

$$\theta_c = \arccos\left(\frac{1}{n\beta}\right). \tag{1}$$

Both the electron as well as the positron emit bremsstrahlung photons on their way through the atmosphere. These can again produce electron-positron pairs. The process continues until the energy of the photon is no longer sufficient for electron-positron pair production. The complete process is called an electromagnetic shower with the produced light being identified as a Cherenkov-flash which happens on a timescale of $\approx 5\,\mathrm{ns}$. IACTs are used to detect the emitted Cherenkov light on the ground. This process is illustrated in Figure 1 below.

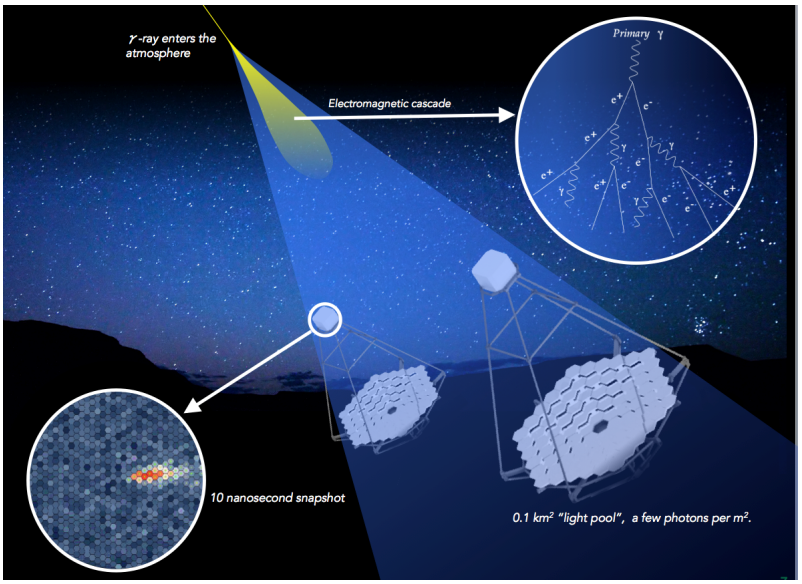

Figure 1: Illustration of imaging a Cherenkov-flash, induced by a primary photon, with IACTs [3].

The energy of the primary photon can be reconstructed by analysing the detected shower image (compare Figure 1 above). Reconstruction of the sources position is also possible by using multiple Cherenkov telescopes [4].

1.2 Cherenkov Telescope Array (CTA)

In this Section, a short overview of the Cherenkov Telescope Array (CTA) project is given. CTA will be the future generation of IACTs and construction has already begun. CTA will be able to cover an energy range from 20 GeV up to 300 TeV as well as improve upon the sensitivity of existing projects such as H.E.S.S., MAGIC or VERITAS by one order of magnitude [5, 1].
CTA will feature two array sites with different telescope sizes to cover the entire sky as well as the goal energy range respectively. One array will be located in the southern hemisphere in Paranal (Chile) and the other on La Palma (Spain) to cover the northern hemisphere. The proposed CTA layout for both arrays, shown in Figure 2 below, features telescope of different sizes. The Large Size Telescopes (LSTs), Medium Size Telescopes (MSTs) and Small Size Telescopes (SSTs).

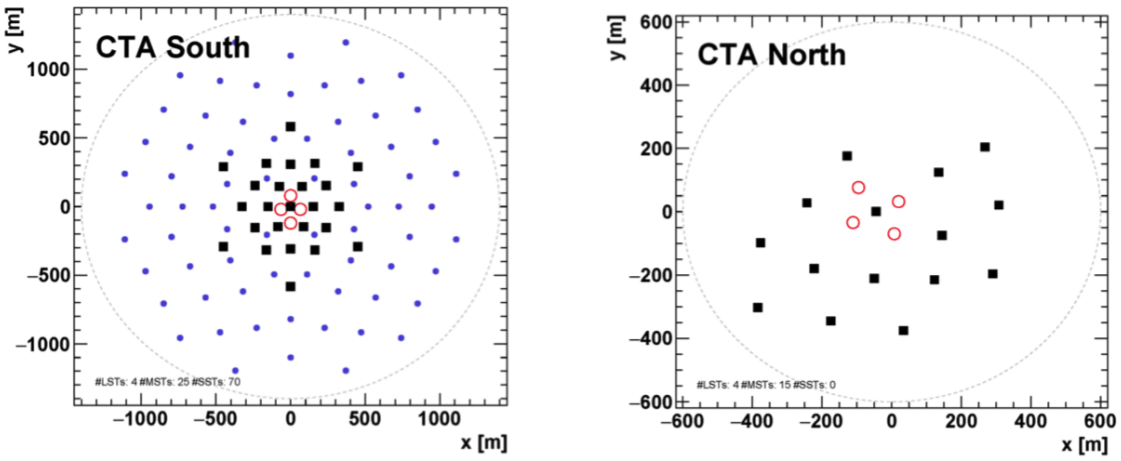

Figure 2: Proposed layout of both CTA arrays. LSTs are represented by red circles, MSTs by black suqares and SSTs by blue dots [1].

Primary photons, that produce Cherenkov-flashes in the atmosphere, follow a power-law. Thus, their flux decreases with increasing energy. The three different telescope types are used to address different regimes of the goal energy range (compare Figure 2 above). All of these telescope designs use segmented mirrors which constitute the complete mirror surface. Segmented mirrors are used since they can be produced cheaper and with a higher precision than a large non-segmented mirror.

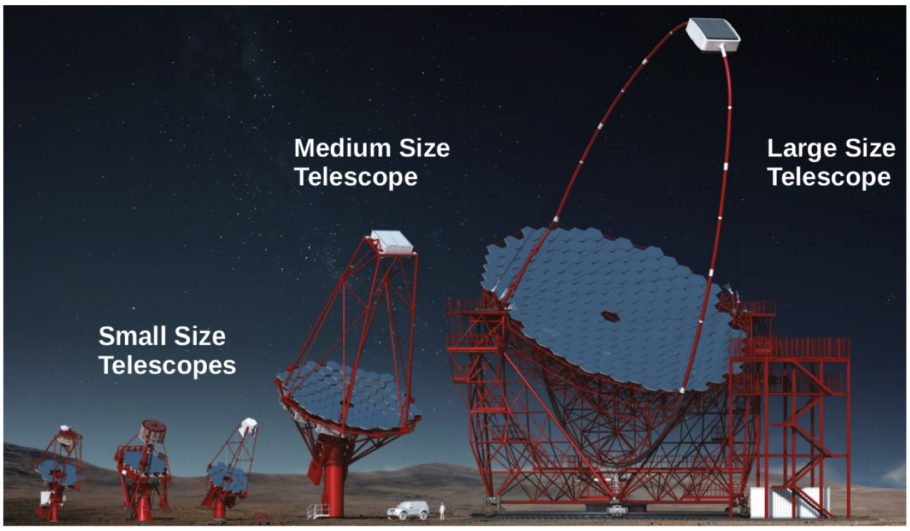

Figure 3: Schematic view of the proposed designs for the LST, MST and SST [2].

LSTs are intended to be used for the $20 - 100\,\mathrm{GeV}$ energy range [1]. Here, the amount of produced Cherenkov-light is rather small due to the low initial primary photons energy.

However, one can expect more flashes to occur per unit time and area due to the higher flux compared to higher energies. Therefore, LSTs feature large mirrors with a diameter of $d_{LST} = 23\,m$ and can be positioned close together [6]. Both the northern and the southern array will feature 4 LSTs each. MSTs cover the energy range $100\,GeV - 10\,TeV$ [1]. Cherenkov-flashes are brighter due to higher primary photon energies. Thus, the mirrors can be constructed with a smaller diameter ($d_{MST} = 12\,m$) and still collect enough light [7]. Due to the lower flux, more MSTs spaced out over a larger area are required to capture enough Cherenkov-flashes. This is seen in the proposed layout as the MST sub-array has a size of $\approx 1\,km^2$ featuring 15 MSTs in the northern and 25 MSTs in the southern array (compare Figure 2) [2].
This process of shrinking the mirror size and increasing the spacing between as well as the number of telescopes continues with the SSTs. These cover the highest energies between $10\,TeV - 300$ TeV intended to be observed with CTA [1, 8]. SSTs are exclusively used in the southern array which, due to its location, is able to observe the galactic plane where sources of higher energetic VHE photons are expected. The southern array accommodates 70 SSTs distributed over an area of $\approx 7\,km^2$ (compare Figure 2) [2]. The physical design for the SSTs is not yet fixed and currently there are three proposed designs. These can be seen in Figure 4 below.

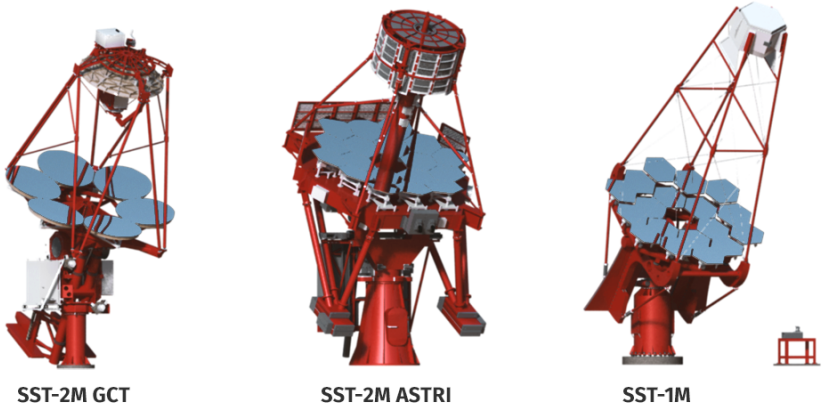

Figure 4: The three different proposed SST telescope designs SST-1M, SST-2M GCT and ASTRI [3].

All the SST designs, illustrated in Figure 4 above, use a main mirror of $d_{SST} \approx 4\,m$ diameter. The SST-1M follows a parabolic single mirror design. This so called Davies-Cotton design is also used in existing telescopes such as H.E.S.S, MAGIC or VERITAS. On the other hand, SST-2M GCT and ASTRI adopt a two mirror Schwarzschild-Couder (SC) design with a $\approx 2\,m$ spherical secondary mirror. The SC-design is more cost effective and leaves more of the telescope budget to be invested in more novel camera technologies and telescopes in

general. The Compact High Energy Camera (CHEC) is one of the newest camera designs and will be described in more detail in the upcoming Sections [9, 7].

2 Compact High Energy Camera (CHEC)

CHEC is one of the cameras that has been developed for the SST-2M designs. Due to its compact design the camera is also compatible with the ASTRI telescope. Whether CHEC will be used and if so for which telescope is still under discussion. The legacy version of CHEC (CHEC-M) used Multi-Anode Photomultipliers (MAPMs). The newest iteration of the camera (CHEC-S), with which this thesis is concerned, adopts Silicon Photomultipliers (SiPMs). A picture of the CHEC-S prototype, currently located at the Max Planck Institute for Nuclear Physics (MPIK) in Heidelberg, can be seen in Figure 5 below.

Figure 5: CHEC-S prototype at the MPIK in Heidelberg.

As stated in Section 1.1 above, Cherenkov-flashes emit photons with optical wavelength. However, this poses a problem, as there is still a considerable Night Sky Background (NSB) caused by man-made or other non-terrestrial sources. To reduce the NSB, it must be able to record data in a time frame similar to that of the to be observed signal. This represents a considerable technical challenge considering Cherenkov-flashes which only last a few nanoseconds. The construction and function of CHEC-S are described in the upcoming Sections.

2.1 Construction

CHEC-S features 32 SiPM tiles with 64 pixels each for a total of 2048 pixels in the complete camera. The SiPM tiles are based on Hamamatsu S12642-1616PA-50 and provide 256 individual 3x3 mm^2 pixels. CTA requires an angular pixel size of $\approx 0.2^\circ$ achievable by 6x6 mm^2 pixels. To this end, four Hamamatsu pixels are directly grouped together to form a pixel of the size required by CTA [5, 10]. The curvature of the focal plane is dictated

by the telescope optics and follows a spherical surface. The SiPM tiles as well as other important components can be seen in the CAD explosion model of CHEC-S in Figure 6 below.

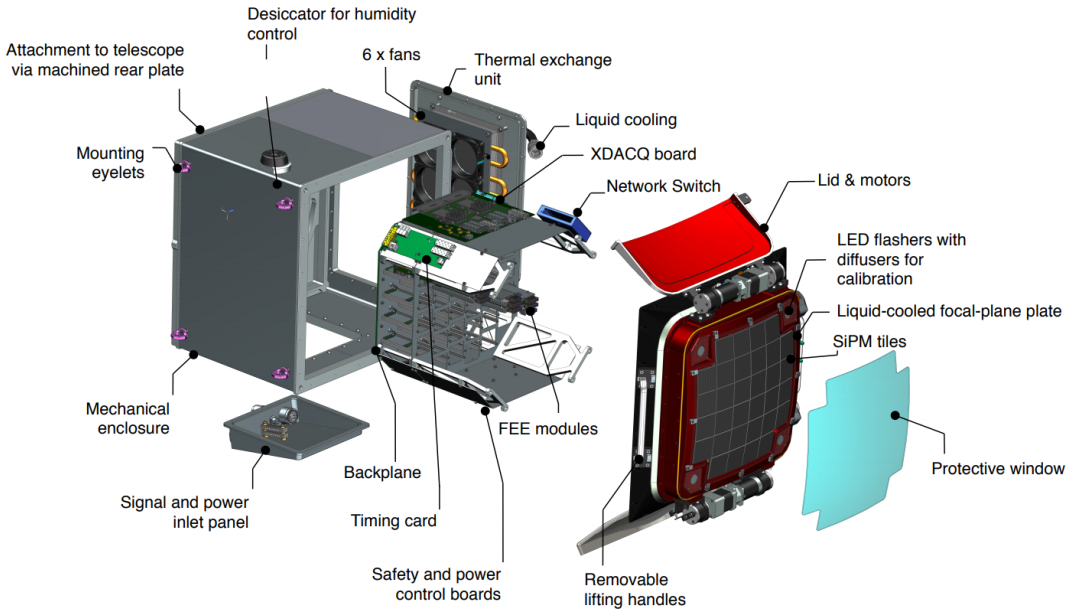

Figure 6: CHEC-S CAD explosion model with important parts highlighted [11].

The camera and the corresponding electronics are set-up in a very modular fashion. This allows for easy exchange of components in the case of failure and component wise testing. The housing provides 32 slots for Front-End-Electronic modules (FEE-Modules). These provide additional amplification as well as signal shaping, triggering and 1 GSa/s sampling of the SiPM signal. The latter provides suppression of the NSB due to the rate difference between the Cherenkov-flash signal and the NSB in the time frame mentioned in Section 1.1 above. The SiPM tiles are attached to the FEE-Modules via cable connections to accommodate the curvature of the focal plane.
All 32 FEE-Modules are plugged into the Backplane board. It handles the trigger information of the FEE-Modules, supplies a clock signal and power. The data-acquisition (XDACQ) board provides 10 Gbps fiber data link from the camera to the outside world. All of these components are placed in a sturdy hermetically sealed housing that maintains an atmospherically stable environment and structural support for the camera components [12, 5, 9, 13, 14, 11].
The FEE-Modules consist of two main components. The first one is the SiPM-assembly with the SiPM itself, a heat-sink and a pre-amplifier. The other is the TARGET-Module, that is attached to this assembly via flexible cables (compare Section 2.1). It provides the

shaping for incoming SiPM pulses, triggering and sampling. A picture of the FEE-Module with highlighted components can be seen in Figure 7 below.

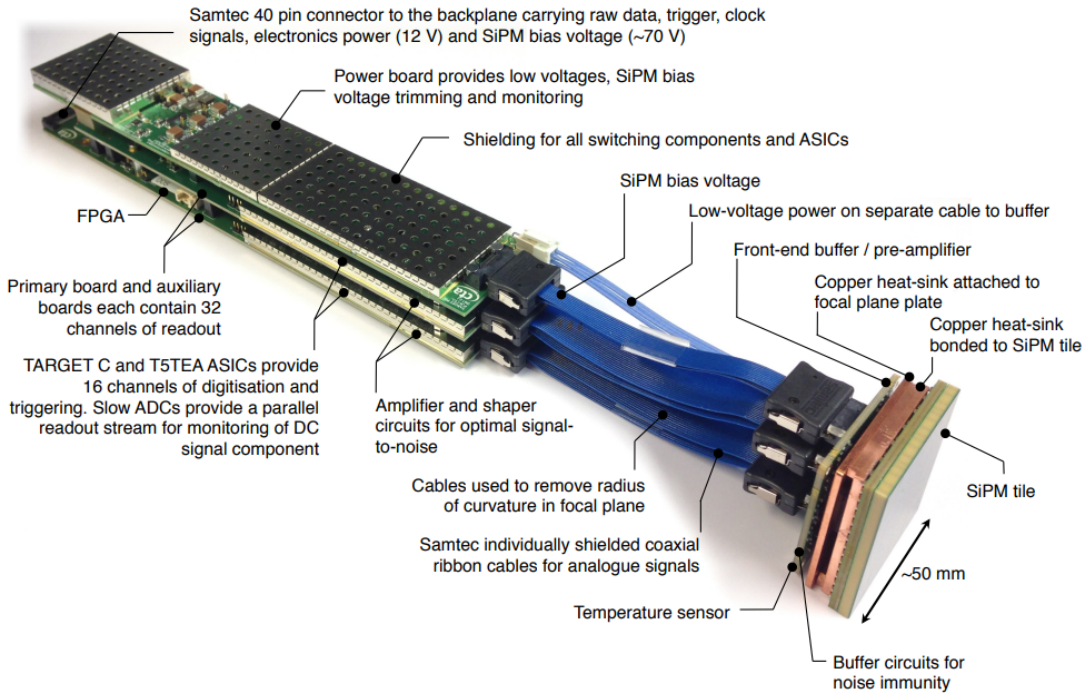

Figure 7: Front-End Electronic Module [15].

The TARGET-Module is named after the TARGET Application-Specific Integrated Circuit (ASIC), which is used as the main component of the TARGET-Modules. To control and program these ASICs a Field Programmable Gate Array (FPGA) is integrated on the TARGET-Module. As seen in Figure 7 above, the TARGET-Module is split up into three different Printed Circuit Boards (PCBs). From top to bottom these are the power-, auxiliary- and primary-board. There are a total of four TARGET ASICs used on the primary-and auxiliary board.

2.2 TeV Array Readout with GSa/s sampling and Event Trigger (TARGET)

The TARGET-ASIC sits at the core of the TARGET-Module. Thus, an overview of its structure as well as its functionality is given in this Section. TARGET stands for TeV Array Readout with GSa/s sampling and Event Trigger (TARGET) ASIC and is custom made for the triggering, full-waveform sampling and readout of Cherenkov telescopes while providing high-performance for a low cost per signal-channel. Several designs for this ASIC have been developed. The previous design, called TARGET7, incorporated the trigger- and sampling-path into one ASIC. The latest version splits these tasks into two standalone

ASICs, T5TEA and TARGET C respectively. This reduces interference between the two [16, 12] while also enabling better performance. The designation TARGET-ASIC is still used and refers to the combination of both ASICs in the latest design.
Four TARGET-ASICs, with 16 channels each, are used in one TARGET-Module. With the aforementioned FPGA, a big range of settings and parameters can be adjusted for T5TEA and TARGET C. Most of these are set using 12−bit values between $0 - 4095$, resulting in voltages between $0 - 2.5\,\mathrm{V}$ produced by integrated Digital-to-Analog Converters (DACs) [12]. Other settings are controlled using 1−bit or 6−bit values. Both T5TEA and TARGET C are now described in greater detail.

2.2.1 T5TEA

T5TEA is responsible for the trigger-path. Pairs of four channels (pixels in the camera) are summed together via an analog sum to form a so called trigger-group (super-pixel). The ASICs receive the amplified, inverted and shaped SiPM signal. The summed up signal for each super-pixel is compared to a variable threshold. A (first-level) trigger-signal for this super-pixel is issued, when the signal crosses the trigger-threshold. A depiction of a super-pixel signal that results in a trigger can be seen in Figure 8 below [17, 9].

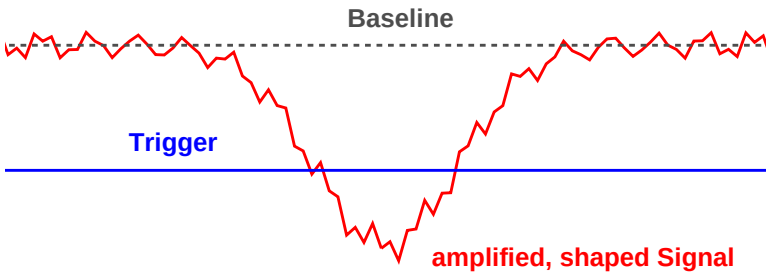

Figure 8: Illustration of a noisy, shaped and amplified SiPM signal that results in a trigger [18].

The position of the trigger-threshold as well as the position of the baseline (pedestal) (signal without SiPM pulse) can be changed using the above-mentioned settings. The threshold can be set as low as $\approx 2.5\,\mathrm{mV}$ while still triggering on a signal and not on pedestal noise. This is well below the signal that is produced by a single photo-electron (p.e.) ($\approx 4\,\mathrm{mV}$) [18, 12]. Thus, T5TEA enables single p.e. triggering.

2.2.2 TARGET C

The task of TARGET C is sampling and digitization of incoming signals. The ASIC consists of three main parts. The Wilkinson Analog-to-Digital Converters (ADCs) as well as sampling- and storage-arrays.

The operation of TARGET C does not differ significantly from that of its last predecessors. Thus, a schematic block diagram of TARGET5, seen in Figure 9 below, is used to illustrate the working principle of TARGET C.

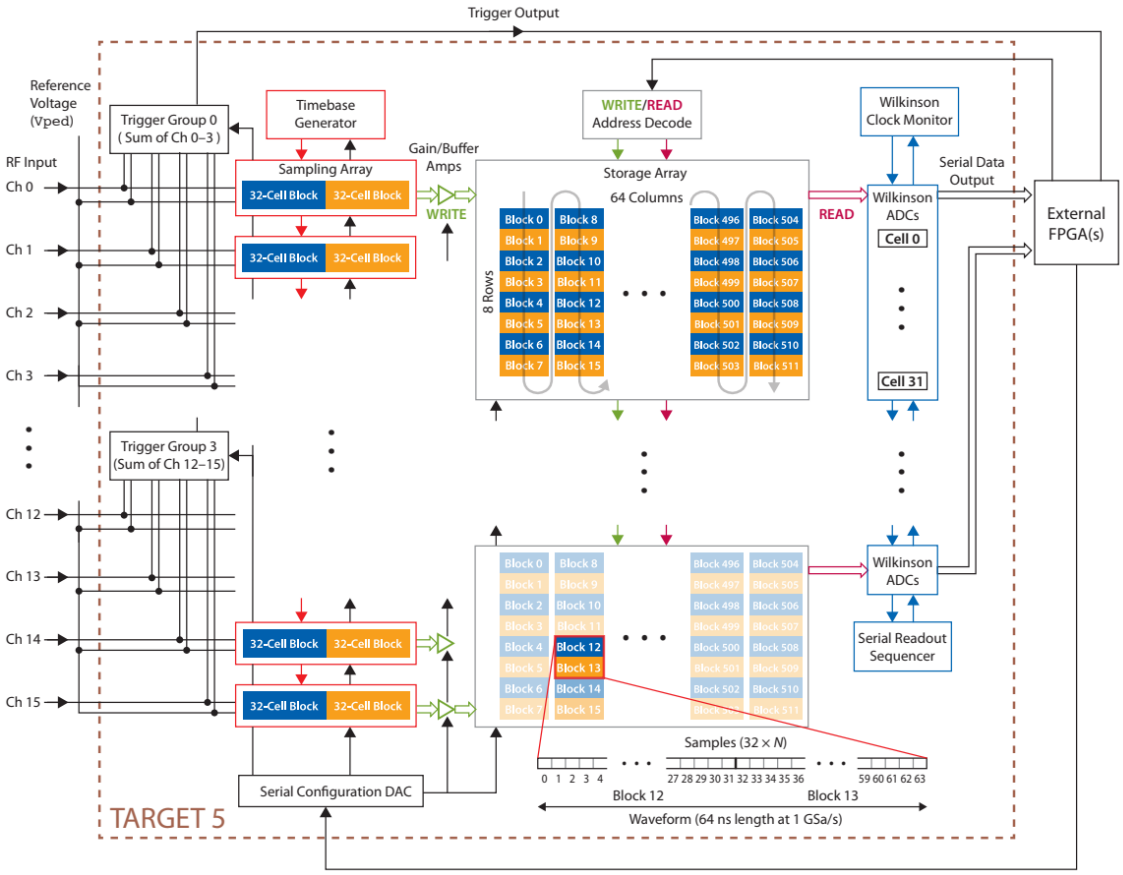

Figure 9: Block diagram of the TARGET5 ASIC with highlighted key components [19].

Each of the 64 channels has one sampling and one storage-array. A 64-cell switched-capacitor array is used to ensure dead-time free sampling. It consists of 64 capacitors (cells) split into two blocks of 32 cells each. Here each cell is a unique capacitor. The two blocks of the sampling array operate in a so called ping-pong fashion. While a part of the incoming waveform is sampled in one block, the other block can write its stored contents into the storage-array. The roles of each block reverse in the second half of the cycle.
The storage-array again consists of 512 blocks for a total of 16384 cells arranged in 8 rows and 64 columns. Assuming a sampling rate of 1 GSa/s this accounts to $\approx 16\,\mu s$ of waveform storage (look-back time). Since the expected (shaped) SiPM signals have a FWHM of $\approx 10\,ns$ the look-back time is sufficiently long to store waveforms until a (second-level) trigger-decision is made (see Section 2.3).

For each channel, 32 cells can be digitized simultaneously by the Wilkinson ADC once a trigger-signal is issued. A key part of the Wilkinson ADC is the Wilkinson-ramp. It is generated by charging a separate capacitor with a constant current. For digitization of a single storage-array cell, a 12-bit counter starts at the same time as the Wilkinson-ramp. The cell that gets digitized as well as the Wilkinson ADC capacitor are connected to the inputs of a comparator. The 12−bit counter stops when the voltage of the Wilkinson-ramp and that of the storage-array cell are equal. The value of the 12-bit counter is the digital value representation of the voltage of the storage-array cell. Random blocks within the storage-array can be digitized at any given time. This enables time dependent selection of events and more complicated trigger-system scenarios [20, 16, 19].

2.3 Working principle of CHEC-S

Pixels in CHEC-S form groups of four, so called super-pixels (compare Section 2.2.1). first-level trigger-signals from the TARGET-Modules get sent to the Backplane. Once a coincidence between two neighboring super-pixels is found within a 2 ns time-frame a second-level (camera wide) trigger is issued. The TARGET-modules digitize a 128 ns large time-frame around the event, such that the complete waveform is visible. This time-frame can be adjusted between 32 ns − 448 ns but is often set to 96 ns for testing purposes. A so called event-packet, containing the digitized waveform, is sent to the XDACQ board where it is buffered and sent out to the camera server that writes the culminated data to disk for further analysis.
When working with a telescope array more complicated triggering setups are possible. This reduces background while increasing spatial resolution. In case of CTA, coincidences of multiple telescopes can be used. Here, trigger information from different telescopes is gathered and a trigger decision is made. The large storage-array of TARGET C allows for enough look-back time to accommodate the comparatively long time it takes to produce a multi-telescope trigger decision. In single telescope operation the trigger decision is made very quickly. Thus, only a subset of 4096 storage-array cells is used. For CTA the SSTs are operated in single telescope mode while the MSTs rely on multi-telescope coincidences [17].

2.4 TARGET-Module temperatures while in operation

While CHEC-S is in operation its components produce heat which needs to be dissipated. As seen in previous sections, the design of the camera incorporates a liquid cooling solution with external chiller. The focal plane of the camera and therefore the SiPMs are directly liquid cooled. This approach results in a temperature stability of $\pm 1^{\circ}$C for the focal plane in the relevant time spans [15]. The modules as well as the rest of the electronics inside the camera are air cooled from the bottom of the housing. The thermal exchange unit is also attached to the liquid cooling loop. The thermal exchange unit as well as its position can be seen in the CAD explosion model of the camera in Figure 6. This one-sided cooling approach produces a stable temperature gradient in the camera while in operation. For

better illustration of this effect, multiple data sets of the prototype camera, so called Runs, are selected and the contained information about the temperatures of all modules primary boards is represented graphically. The temperature distribution for one of the selected Runs can be seen in Figure 10 below. Graphs for other Runs share a similar distribution and can be found in Appendix A.4.

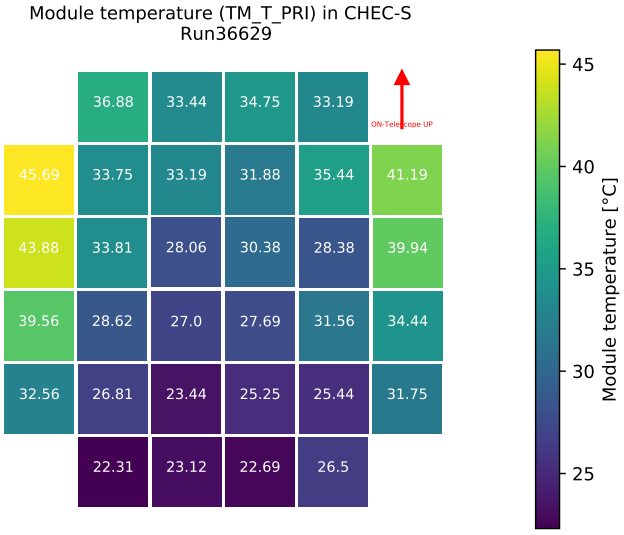

Figure 10: Temperature of FEE-Modules while taking data for example Run.

In the case of the example Run the temperature range extends from ≈22°C to ≈46°C. The locations of the coldest modules coincide with the position of the cooling assembly. The air heats up on its way through the camera. Thus, resulting in a less effective cooling for modules that are located at the top of the camera. In addition, the structural design of the housing leads to a build-up of air in the corners. The decreased airflow in these areas results in higher module temperatures.
It is suspected that this temperature gradient might have an effect on the cameras calibration or more specifically the calibration of the TARGET-Modules which is performed at a fixed temperature. The exact nature of the gradients influence on the TARGET-Modules calibration is studied in this thesis.

3 Calibration using transfer-functions

To deduce the impact of the temperature gradient of the TARGET-Modules inside CHEC-S, as observed in Section 2.4 above, the default calibration procedure for a single TARGET-Module needs to be understood. The setup as well as the calibration procedure is explained in this Section. Components of CHEC-S, in particular the TARGET-Modules, need to be evaluated as part of a fixed testing protocol. This includes tests of functionality as well as calibration of the TARGET-Modules. This calibration is mandatory to successfully reconstruct the energy of a primary photon that produces an observed Cherenkov-flash. As mentioned previously, the complete waveform of a received signal gets stored and is read out in units of ADC-counts. To reconstruct the primary photons energy the p.e. equivalent must be known for each sample of the waveform.
Since the p.e. equivalent is not directly accessible the voltage of each sample is used. To this end, every TARGET-Module is calibrated using a transfer-function. It assigns each ADC-value of a given storage-cell a corresponding voltage value so the waveforms can be reconstructed with the intended units. Each TARGET-Module has a unique designation, the so called SN-number, of the form SNXXXX where X can be a number between $0 - 9$. The TARGET-Module will just be refereed to as module from here on out. The procedure of how to generate these transfer-functions is described in the following.

3.1 Setup for recording transfer-functions

As stated previously, modules are calibrated at a pre-determined fixed temperature of $T_{ref} = 23°C$. Due to how the measurements in this thesis are performed the reference temperature is changed to $T_{ref} = 20°C$. Observed effects remain the same. To calibrate modules at a fixed temperature the calibration is conducted within a temperature chamber, seen in Figure 11 below. It enables the temperature to be regulated with an accuracy of $\pm 0.1°C$ in a temperature range between $-70°C$ and $175°C$.

Figure 11: Temperature-Chamber used for module calibration.

To acquire the needed transfer-functions data must be recorded with a module at different known input amplitudes. From this data the transfer-functions can be generated later on. The SiPM-assembly does not produce input amplitudes of known size and thus is not used. Instead input signals for the module are generated using a function generator (Keysight 33611A). The output of the SiPM-Assembly, including amplification, has been measured and the resulting signal parameterized. It is used as a template with tunable amplitude for the function generator. A depiction of the parametrized pulse can be seen in Figure 12 below.

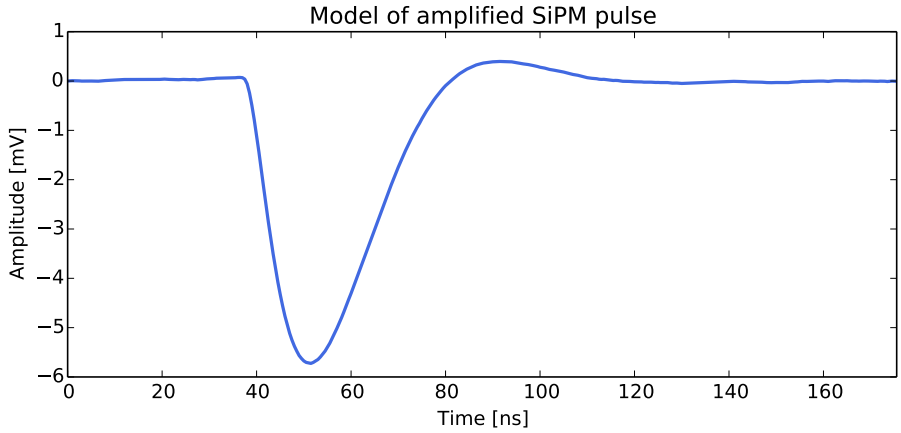

Figure 12: Parameterized output signal of the SiPM-assembly for an example amplitude [17].

As seen in Figure 12 above, a signal pulse expected from the SiPM-Assembly lasts approximately 170 ns. The used function generator provides settings for sampling speed, samples in the signal and distance between two signals for an arbitrary waveform. The sampling rate of the signal is set to 500 MSa/s and the total pulse length to 100 Sa. With these settings the produced pulse has a width of 200 ns which is close to the actual width seen in Figure 12 above. The interval between pulses (burst rate) is set to 330µs which determines the frequency with which data is written to disk. Thus, the value is chosen such that the write speed of the disk used to store data is not exceeded. The output of the function generators could now be attached to each channel separately. However, to speed up testing a special splitter board has been developed by Dr. Adrian Zink. It splits and buffers the functions generators signal into 32 separate signals with the same amplitude as the input signal. These signals are forwarded to the module by the standard ribbon cable that normally connects the SiPM-Assembly to the module. To cover all 64 channels of the module two of these splitter boards are used. A picture of these two assembled splitter boards can be found in Figure 13 below.
The splitter board also offers the possibility to only turn on specified channels. However, when channels are turned off additional crosstalk is introduced in the disabled channels since the practically infinitely large terminal resistance produces signal reflections for these channels. Nevertheless, this effect does not occur when recording transfer-functions since all channels are active.

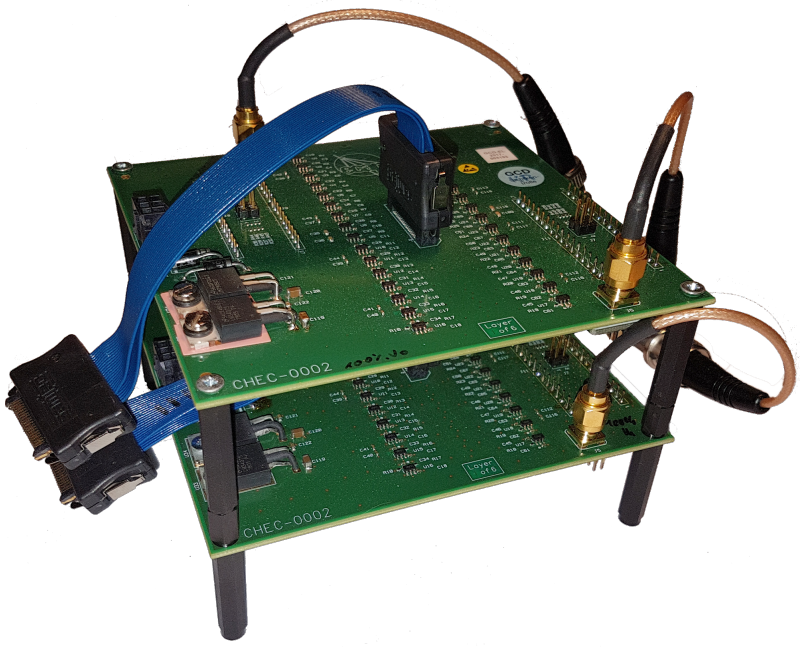

Figure 13: Two splitter boards assembled together for a total of 64 output channels.

Also the Backplane does not fit into the temperature chamber and a stand alone adapter is used to interface with the module. It provides power, trigger in- and outputs, a clock signal as well as a data connection via fiber optics. A picture of the stand alone adapter can be seen in Figure 14 below.

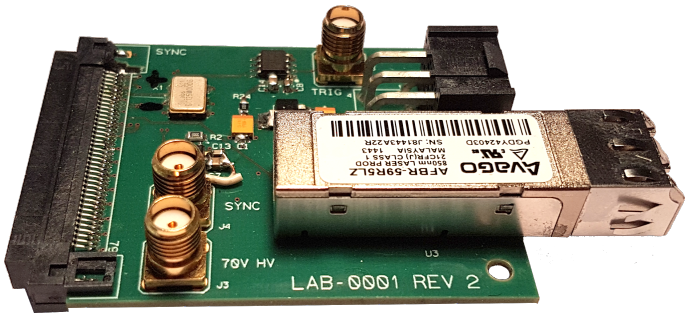

Figure 14: Module stand alone adapter.

The TRIG-input of the stand alone adapter, seen in Figure 14 above, emulates a trigger signal. Hence, the module will begin digitization of stored data when a signal is applied to this input. The sync-output of the function generator that produces a signal each time a pulse is generated is connected to the TRIG-input. The complete setup for recording transfer-functions can be seen in Figure 15 below.

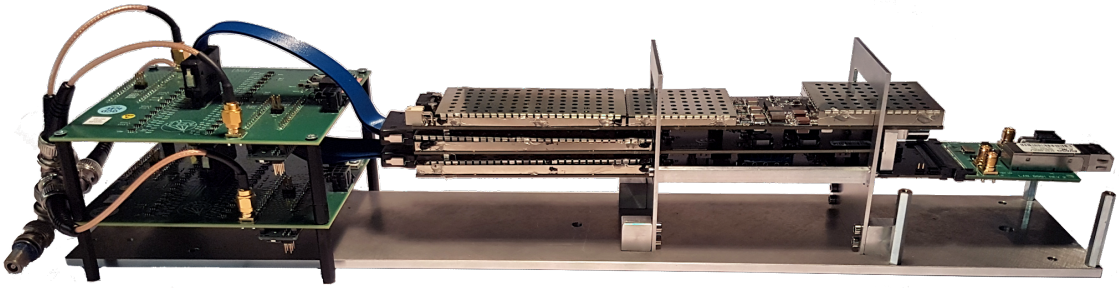

Figure 15: Setup to record transfer-functions outside the temperature chamber.

The setup seen in Figure 15 above gets installed into the temperature chamber (see Figure 16 below). Cable feed-throughs are closed with an insulating foam plug and a fan is added to enhance airflow through the module. A schematic view of the setup can be found in Figure 17 below.

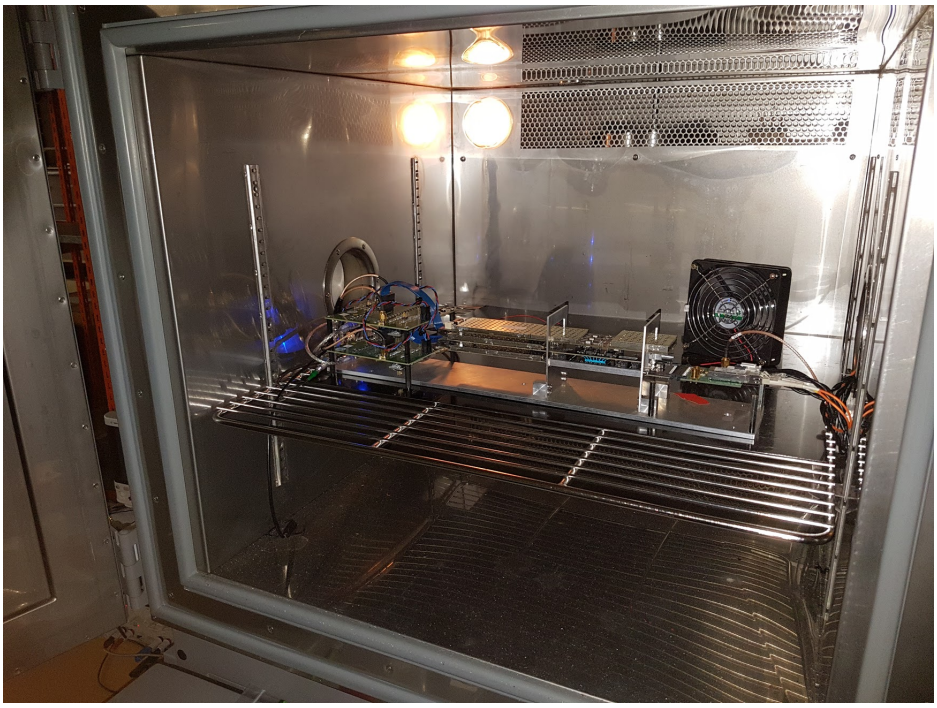

Figure 16: Setup to record transfer-functions inside the temperature chamber.

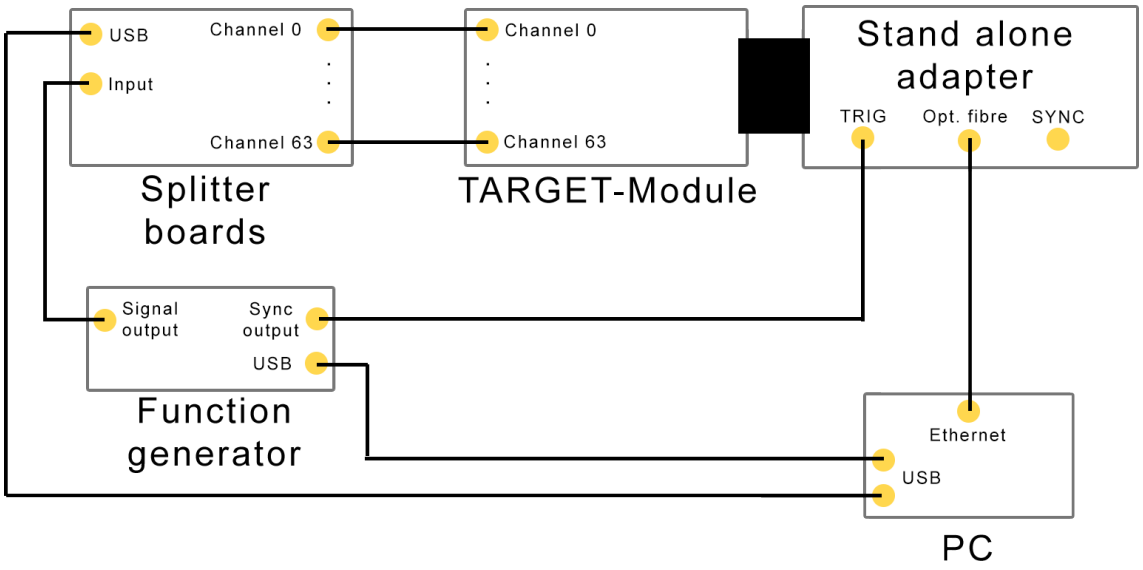

Figure 17: Schematic setup for recording transfer-functions.

3.2 Generating transfer-functions

With the setup, as described in Section 3.1 above, data can be recorded. This Section focuses on how data is recorded and how transfer-functions can be generated from this recorded data. Module SN0072 is used for this. When the module is initialized standard as well as module specific parameters are loaded. To ensure the correct setting of trigger thresholds, the position of the pedestal of all channels must be equal. As mentioned in Section 2.2.1, the position of pedestal of each channel can be adjusted using a parameter called VPED. The associated parameter values were determined during the commissioning process. The procedure used to generate transfer-functions is now described in more detail for a single channel. The concept remains the same for all of the 64 channels of the module.

3.2.1 Waiting period for thermal equilibrium

To guarantee a measurement at the correct temperature one has to estimate the time until a thermal equilibrium is achieved between the module and the air inside the chamber. The camber is set to 20°C and the module is left in there over night to ensure an equilibrium has been reached. A temperature sensor is installed on the primary board of the module. It is monitored over time while changing the set temperature of the chamber from 20°C to 25°C. The resulting plot can be seen in Figure 18 below.

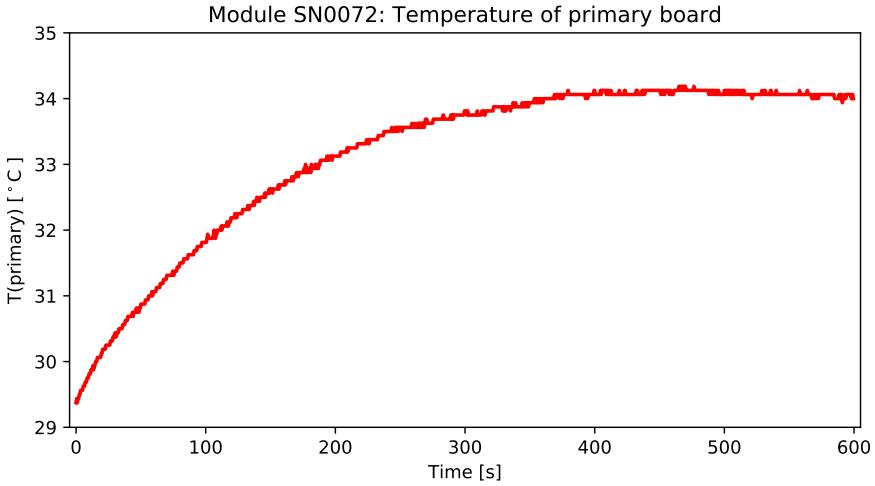

Figure 18: Temperature of modules SN0072 primary board over time while taking data. Temperature change from 20°C to 25°C in the temperature chamber.

From Figure 18 above, one can conclude that an equilibrium state is reached within $\approx 360\,\mathrm{s} = 6\,\mathrm{min}$ after changing the temperature from 20°C to 25°C. The measured ambient temperature inside the laboratory is $\mathrm{T_{lab}} = (17 \pm 3)^{\circ}\,\mathrm{C}$. Thus, a waiting period of 10 min

should suffice for the module to acclimatize to 20°C, when installing it into the temperature chamber setup. Also an offset of ≈ 9°C between set chamber and module temperature can be observed. The module heats up during operation. Due to insufficient heat dissipation the measured module temperature is offset compared to the ambient temperature.

3.2.2 Data taking

After the module temperature has reached an equilibrium state data can be recorded. A transfer-function is required for each cell in the used storage-array of TARGET C. This is due to the fact that each cell in the storage- and sampling array is a small capacitor and capacitance differences occur between the different cells influencing the stored ADC-value. Every time a pulse is generated a trigger-signal is issued by the sync output of the function generator (event) and the stored waveform in each channel is read out. Within these waveforms the ADC-value of the signal peak must be determined as well as in which cell of the storage-array the peak is located. Therefore, at least one ADC-value for each input amplitude and each of the 4096 cells in the used storage-array of TARGET C is required to later determine the transfer-function of each storage-array cell.
As mentioned in Section 2.2.2, TARGET C provides a sampling speed of $1\,\mathrm{GSa/s} = 1\,\mathrm{Sa/ns}$. Together with the set period between two function generator pulses (burst rate) of $330\,\mu\mathrm{s}$, TARGET C would sample 80 full passes and 2319 cells to the storage-array in between two pulses. This scheme continues for as long as the function generator is turned on. Assuming that the sampling speed of TARGET C remains unchanged one can determine that only 256 out of 4096 cells get hit with a peak.
For all cells in the storage-array to be hit the burst rate must to be a multiple of 4097. In this case, the TARGET C would complete one full write passes and 1 cell before the next signal peak occurs. However, the disk used to store the data cannot handle this rate. However, the clock of the module is only accurate to within 20 ppm. Taking this into account the sample rate can vary $\pm 6.6\,\mathrm{ns}$ over the rather large timescale of $330\,\mu\mathrm{s}$ between pulses. Assuming the actual variance is evenly distributed between $0 - 6.6\,\mathrm{ns}$ the number of hits per cell can be calculated. The number of hits after 300000 events can be seen in Figure 19 below.

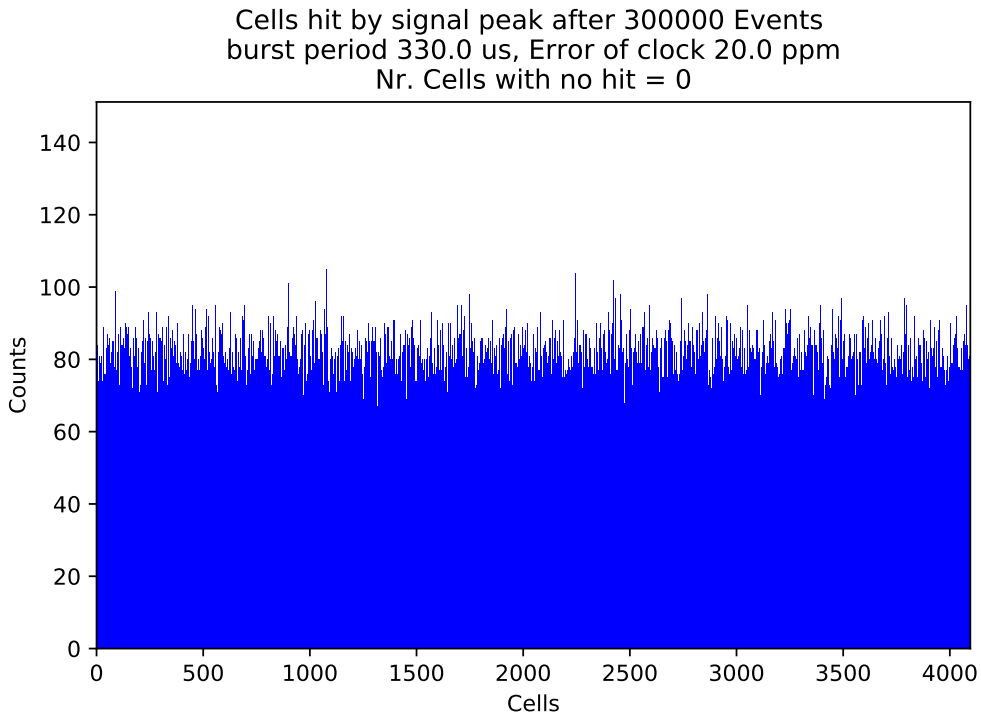

Figure 19: Number of hits per cell in the TARGET C storage-array taking into account variations in the sampling rate.

As seen in Figure 19 above, all cells are hit at least 50 times. From this, one can estimate the error of the calculated mean ADC-value of a storage-cell. Due to noise, the AD-conversion is affected with an error of $\sigma_{\mathrm{ADC}} = 1.6\,\mathrm{ADC\text{-}counts}$ [17]. For a mean value over 50 measurements this error is reduced to $\sigma_{mean} = \frac{\sigma_{ADC}}{\sqrt{50}} \approx 0.2$ ADC-counts. Thus, taking 300000 events provides enough statistics per cell to calculate the mean ADC-value per input amplitude sufficiently accurate. Input amplitudes ranging from $0 - 2500\,\mathrm{mV}$ are used. A list of all used amplitudes can be found in Appendix A.1.
When a trigger signal is issued a 96 ns time window starting at the position where sampling currently occurs within the storage-array is digitized (compare Section 2.3). However, the signal path length of the trigger-path results in a delay of the trigger signal. Thus, digitization would start too late and the waveform would not lie within the readout window. This can be corrected for by using a FPGA setting called TRIGGERDELAY. It is set to 399 and shifts the readout window in the storage-array, such that the signal is again within the readout window. For every amplitude 300000 events are recorded and the resulting data saved. The term "sample" is used to reference the steps within a readout windows from here on out. The data recorded in the way described above is referred to as r0-data. The zero indicates that no additional processing has taken place. The first event for three different amplitudes can be seen in Figure 20 below.

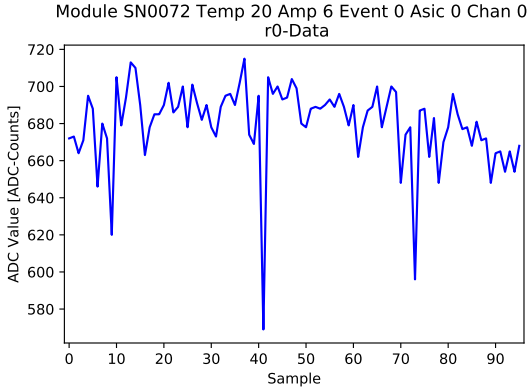

(a) Event 0 with an input amplitude of 6 mV for module SN0072 ASIC 0 channel 0 .

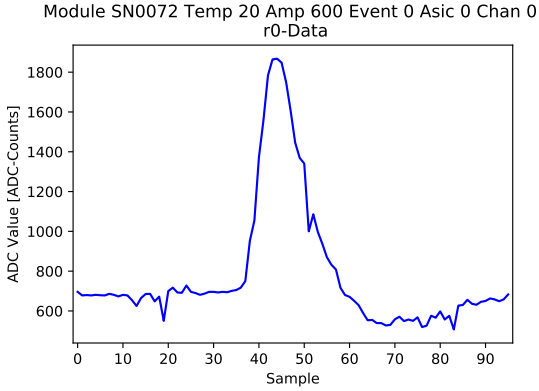

(b) Event 0 with an input amplitude of 600 mV for module SN0072 ASIC 0 channel 0.

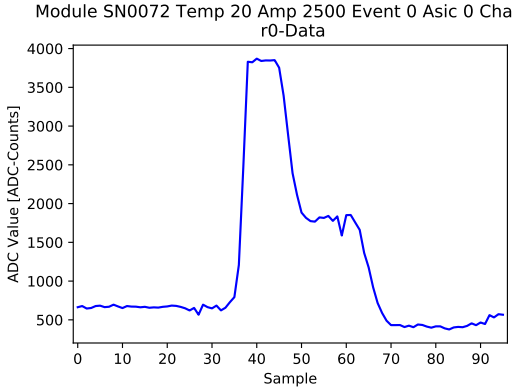

(c) Event 0 with an input amplitude of 2500 mV for module SN0072 ASIC 0 chan 0.

Figure 20: First event of a given amplitude for module SN0072 ASIC 0 channel 0 using r0-data.

As seen in Figure 20c above, the peak for 2500 mV is cut off while the pulse in general features an extension to the right. This effect is produced by the shaper located on the module when operated in its saturation regime. The extension to the right increases in size with increasing input amplitude. Also pulses for small input amplitudes are not visible in the r0-data due to cell-to-cell variations in the storage-array and the ≈ 680 ADC-count offset seen Figure 20. To compensate for this one can use pedestal correction.

3.2.3 Pedestal correction

Pedestal correction can be applied to r0-data to remove cell-to-cell variations in the storage-array and to remove the signal offset.

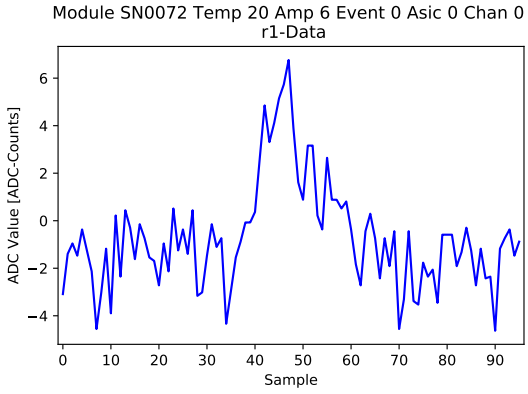

(a) Event 0 with an input amplitude of 6 mV for module SN0072 ASIC 0 channel 0.

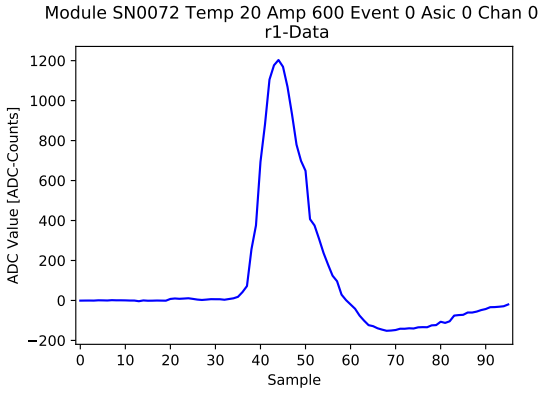

(b) Event 0 with an input amplitude of 600 mV for module SN0072 ASIC 0 channel 0 .

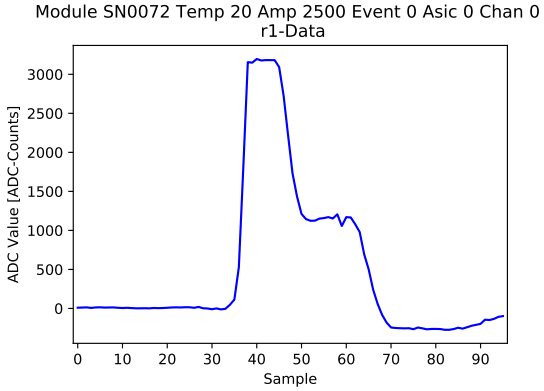

(c) Event 0 with an input amplitude of 2500 mV for module SN0072 ASIC 0 channel 0.

Figure 21: First event of a given amplitude for module SN0072 ASIC 0 channel 0 using r1-data.

Using the recorded data with zero input amplitude (output of function generator turned off) one can determine the voltage offset of every cell in the storage-array (pedestal) (compare Section 2.2.1). This pedestal can be subtracted after the data has been recorded. The result is so called r1-data. The same events, seen in Figure 20 above, are shown after pedestal calibration in Figure 21 above. One can see that the cell-to-cell variation has been greatly reduced when comparing the r0-data (see Figure 20) with the r1-data (see Figure 21). Also the signal peaks of small amplitudes are now visible and can be used later while the signal has been shifted down towards zero since the voltage offset has been removed.

3.2.4 Calculating transfer-functions

From the recorded and pedestal calibrated r1-data one can now calculate the values for the transfer-function. A script, initially developed by David Jankowsky and modified by the author, is used to calculate transfer-functions and save the resulting values. Due to a difference in signal shape (see Figure 21 above), different approaches are required to extract the pulse position and value for small and large amplitudes. How the values for the transfer-functions are calculated with this script is now explained.

For input amplitudes between $42 - 1800\,\mathrm{mV}$ a fit function can be used to extract the peak position and its ADC-value. Events in these input amplitude ranges look similar in shape to the event seen in Figure 21b above and do not enter the shapers saturation regime. Using a method developed by David Jankowsky, the undershoot of the pulse can also be incorporated into the fit function to incorporate additional information about negative-amplitudes into the transfer-function. However, not all amplitudes in the range mentioned above are used to extract information about the undershoot. A list of all amplitudes used as well as their corresponding negative amplitude value can be found in Appendix A.3. The process is split into two parts. In the first part, the signal transit-times are determined for each channel. To this end, the first 200 events for each channel and amplitude are fitted with the sum of two Landau distributions. The script used for this is written in C++ and uses Root which provides a predefined Landau distribution. Each Landau distribution provides three free parameters for amplitude, position and width. Initial values for these parameters can be found in Appendix A.2. An example fit can be found in Figure 22 below.

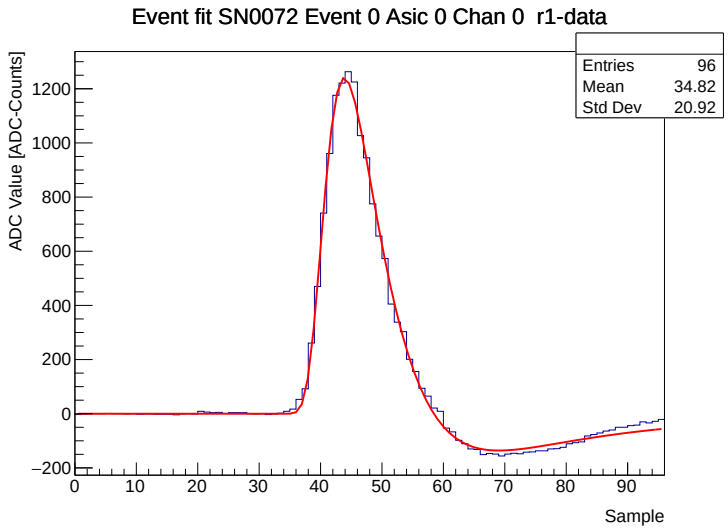

Figure 22: Double-landau fit (red) of event 0 of module SN0072 ASIC 0 channel 0 for an input amplitude of 600 mV.

Using these 200 fits the mean peak position inside the readout-window is calculated for both the positive and negative peaks as well as for each amplitude and channel. The mean peak position within the readout window contains information about the signal transit-time for each channel.
In the second part each event for channel 0 is fitted with the above mentioned fit function and the peak position is determined. The sample, used to read out the ADC-value of a given channel is then calculated. This is done by calculating the signal transit-time difference between the given channel and channel 0 and adding it to the fitted peak position. The acquired ADC-value at this new peak position is assigned to the corresponding storage-array cell. The latter is determined by reading out the position of the events first sample in the storage-array (where the readout window of the event starts within the storage-array). Using the previously calculated sample one can determine the storage-array cell where the peak is located. As seen in Figure 19 above, each cell gets hit by a peak multiple times. The mean over all these extracted ADC-values corresponding to one storage-array cell is calculated for each amplitude and storage-array cell and stored. For pulse amplitudes below 42 mV the mean peak positions determined for 42 mV are used directly to look up the ADC-value and similarly for amplitudes above 1800 mV. The results are transfer-functions for all cells in the storage-array. For the analysis conducted in this thesis, the transfer-functions are written to disk. The transfer-functions for all 4096 storage-array cells of channel 0 can be seen in Figure 23b below.

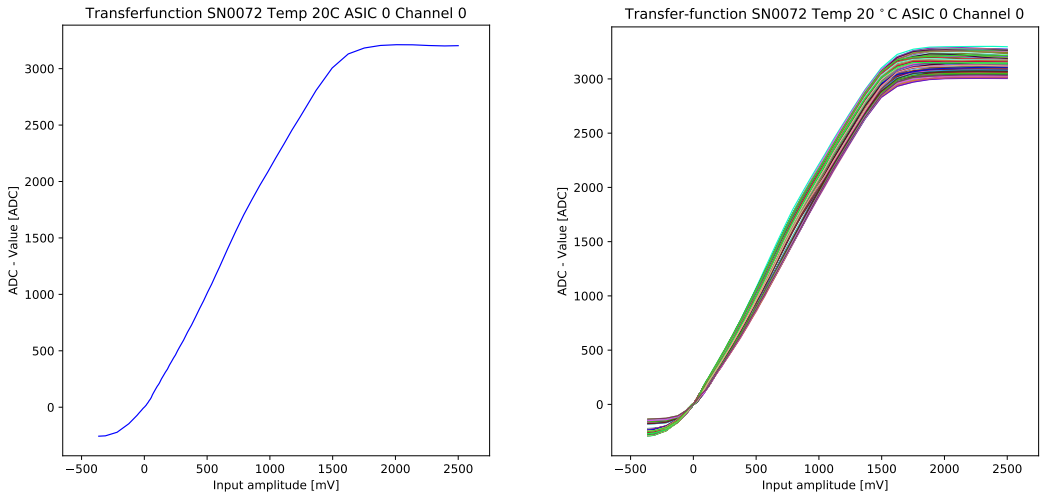

(a) Transfer-function for one cell

(b) Transfer-function for all 4096 cells

Figure 23: Transfer-function of module SN0072 ASIC 0 channel 0 at 20°C.

The characteristics of the transfer-function can be identified more easily by using the transfer-function of a single cell (see Figure 23a). One can identify a linear region between $0 - 1500\,\mathrm{mV}$. For larger input amplitudes, the shaper begins to saturate. As discussed previously, this leads to events like the once shown in Figure 21c above where the peak is cut off. Thus, the determined peak ADC-value does not change anymore with increasing input amplitude. This leads to the observed saturation behavior of the transfer-functions. As seen in Figure 23b above, the transfer-functions for different storage-array cells differ from each other but show the same overall shape. The procedure discribed above is repeated for all 64 channels of the module. To use the calculated transfer-functions with CHEC-S a lookup is generated using a script developed by Jason Watson (University of Oxford).

4 Temperature dependency of transfer-functions

Now that the procedure of how to generate transfer-functions is known one can investigate their temperature dependency. The observed temperature gradients of the modules while the camera is in operation have been determined in Section 2.4. The maximum and minimum temperatures can be used to determine the temperature range of interest in which the temperature dependency should be investigated. The range selected for SN0072 is 5°C - 50°C with a step-size of 5°C. Temperature below 20°C are included to get a more complete overview of the transfer-functions temperature dependency if it exists.
Data is taken for the above mentioned temperatures with enough time in between measurements for the module to stabilize its temperature. The files recorded at 10°C and 25°C were corrupted and are therefore not used in the further analysis.

The recorded data is pedestal calibrated for each temperature separately. This removes temperature dependent pedestal offsets of the transfer-function but other changes remain. When the camera is in operation, new pedestals are recorded and applied frequently. Thus, an analysis where data is pedestal calibrated for each temperature separately shows effects that would be seen in the camera. Following the procedure described in Section 3.2 transfer-functions are generated using the r1-data. The mean transfer-function is calculated for each temperature using all 4096 transfer-functions of a single channel. The deviation TF(T) - TF(20°C) between the transfer-function at a given temperature TF(T) and the one at the reference temperature TF(20°C) is a measure for the degree of deviation. The resulting deviation is then graphically represented over input amplitude and temperature. This can be seen in Figure 24 below. These kinds of graphs will be referred to as “deviation-plots”.

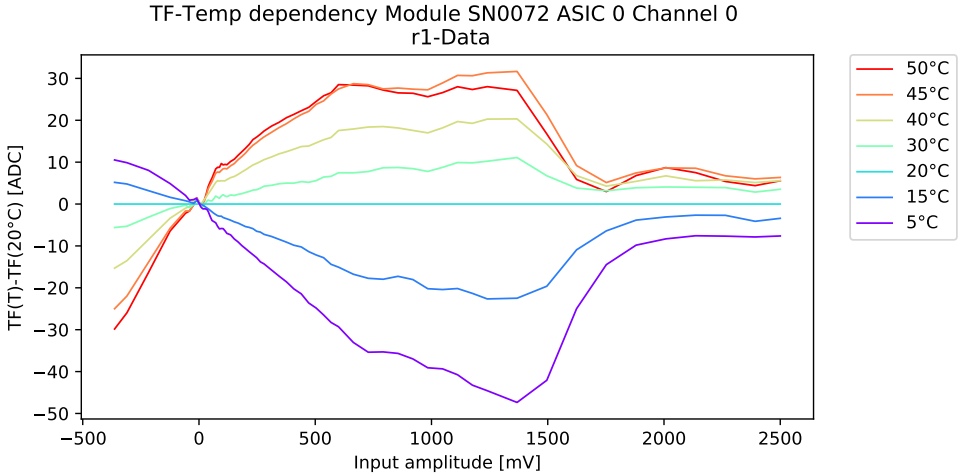

Figure 24: Deviation of the mean transfer-function at a given temperature TF(T) from TF(20°C), the one recorded at the reference temperature, for module SN0072 ASIC 0 channel 0.

As seen in Figure 24 above, a temperature dependency of the transfer-function can clearly be identified. The extracted ADC-counts increase with ambient temperature for positive input amplitudes. When the transfer-function leaves its linear region for input amplitudes exceeding $\approx 1500\,\mathrm{mV}$ the deviation decreases. As discussed in Section 3.2.4, the transfer-function flattens in this region due to shaper saturation. The transfer-functions for temperatures larger than 20°C saturate earlier. When entering this regime, the deviation between both TF(T) and TF(20°C) decreases and then remains approximately constant. This is due to the fact that peak amplitudes in the stored waveforms do no longer increase significantly with input amplitude (compare Figure 21c) due to the above mentioned shaper saturation. All other channels share a similar behavior and examples can be seen in Appendix A.5. Due to their similar structure a mean deviation graph can be calculated over all channels. The result can be seen in Figure 25 below.

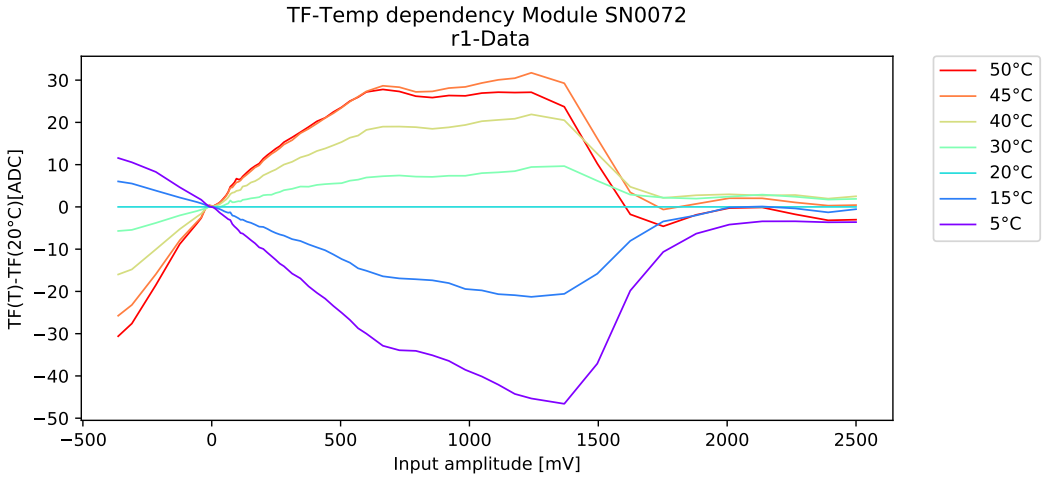

Figure 25: Deviation of the mean transfer-function at a given temperature TF(T) from TF(20°C), the one recorded at the reference temperature, for module SN0072.

The values in Figure 25 above are calculated using the mean over all channels for one amplitude and temperature. The corresponding standard deviation (STD) can be found in Figure 26 below.

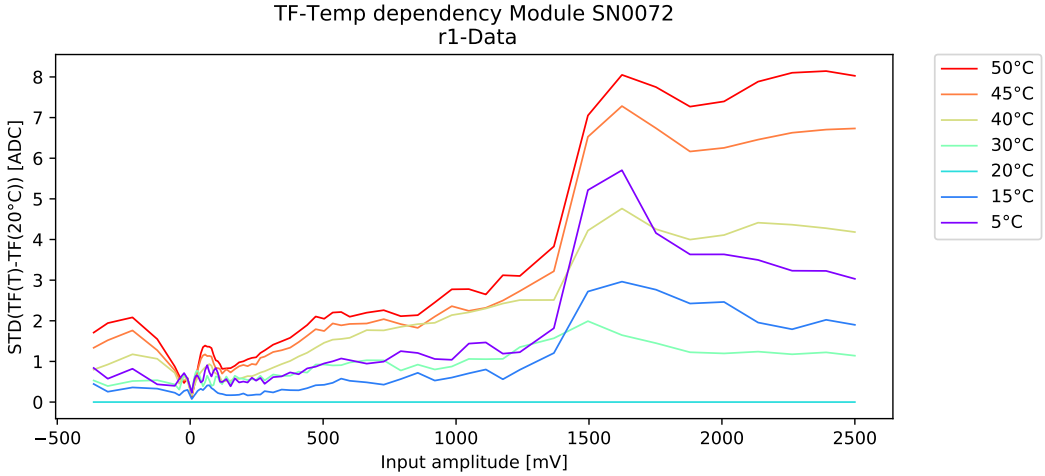

Figure 26: Standard deviation of the mean transfer-function at a given temperature TF(T) from TF(20°C), the one recorded at the reference temperature, for module SN0072.

The standard deviation shown in Figure 26 above ranges from $0 - 2$ ADC-counts for small input amplitudes and up to 8 ADC-counts for large input amplitudes. However, for these large input amplitudes the transfer-function itself has a value well above 2000 ADC-counts resulting in a sub 1% deviation from the transfer-functions value. The same holds for small input amplitudes. Thus, calculating the mean deviation-plot for a single module is sufficient to characterize the overall temperature dependency of the transfer-functions.
This process is repeated with three other modules (SN0040, SN0038 and SN0024) using different temperature ranges to rule out the possibility that this is an isolated effect. The results for all tested modules can be found in Appendix A.6 while the one for module SN0040 can be seen in Figure 27 below.

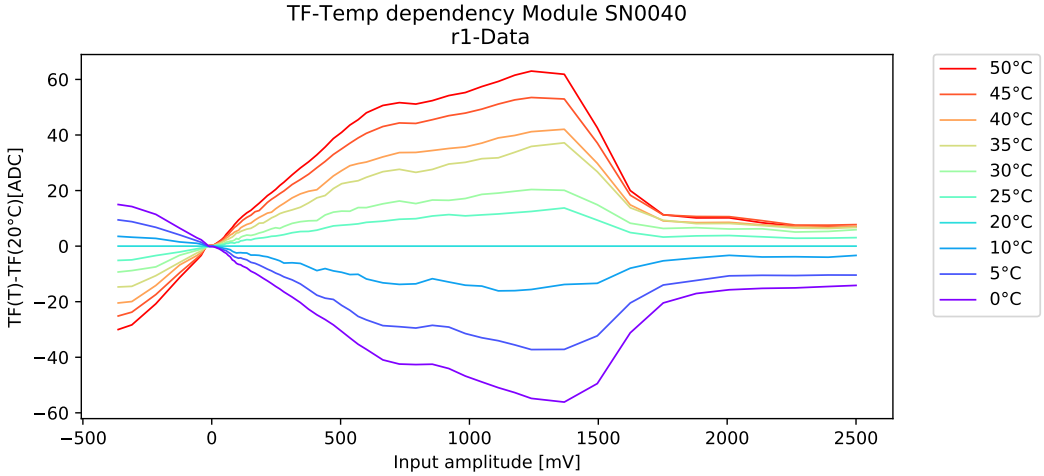

Figure 27: Deviation of the mean transfer-function at a given temperature TF(T) from TF(20°C), the one recorded at the reference temperature, for module SN0040.

Despite a difference in magnitude of the deviation between modules, one can identify a general trend when comparing the deviation plots of all four modules. This yields the result that a temperature-dependency of the transfer-functions is defiantly present with deviations ranging up to 80 ADC-counts (see Appendix A.6) for large input-amplitudes.

5 Influence of temperature dependency on charge resolution

As concluded in Section 4 above, a temperature dependency of the transfer-functions is clearly identified. However, the effects that could result from this deviation are not yet clear. In this Section, the impact of this deviation on the charge resolution of CHEC-S is investigated and compaired to the requirement set by CTA. The charge resolution is an important aspect for CHEC-S. It indicates how well the camera can separate individual charges (levels of illumination) from one another. Here, charge is defined as the integral of an event within a given area around the signal-peak. This integral is sensitive to changes in the amplitudes of extracted events. Thus, the temperature dependency of the transfer-functions, seen in Section 4, has a direct influence on the charge resolution of the CHEC-S. First, the effect of the temperature dependence on the charge spectrum is estimated. To this end, Runs of the camera-prototype with different known mean levels of illumination are used. These have been recorded at the MPIK in Heidelberg in laboratory conditions with a laser. The used Runs also provide information about the temperature of every modules primary- and auxiliary board. This can later be used to determine the amount of deviation that needs to be subtracted for each TARGET ASIC in the camera. The charge spectrum of every Run can be extracted via a pre-defined script on a per-channel basis. The charge spectrum of a single channel for Run43513 with a mean illumination level of 1.25 p.e can be found in Figure 28 below.

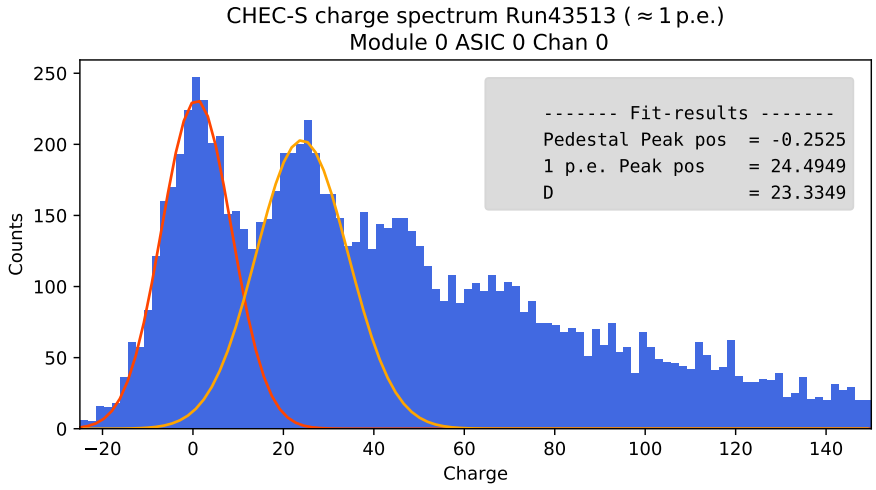

Figure 28: Charge spectrum of CHEC-S Run43413 (≈ 1 pe).

The first peak in the spectrum is the pedestal peak followed by the 1 p.e. peak and peaks of higher levels of illumination. These first two peak positions are determined using two

Gaussian fits and the distance between the pedestal- and 1 p.e. peak D = 23.3349 mVns is calculated. D can be used to estimate a p.e illumination level given a certain charge.
Now the impact of the transfer-functions temperature dependency is estimated. To this end, the deviation-plot of module SN0040 is used since it provides information for more temperatures. The deviation data is normalized using the largest deviation. The deviation curve for each temperature is parameterized by a polynomial g(T, x) of 16th order where T is the temperature and x the input amplitude. The polynomials order is chosen such that the resulting fitted polynomials trace the deviation curves well enough which is not the case for lower orders. The resulting polynomials as well as the normalized deviation-plot can be seen in Figure 29 below.

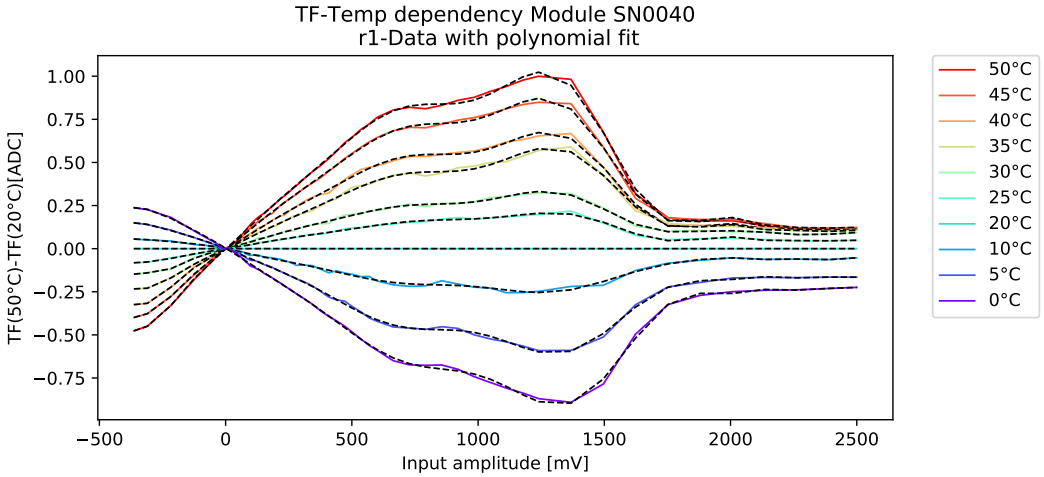

Figure 29: Normalized mean transfer-function deviation relative to 20°C for module SN0040 with polynomial fit of 16th order for each temperature.

The polynomials do not reproduce the deviation perfectly but the overall form is retained and this is sufficient to estimate the effect the deviation has on the charge-spectrum. To correct the deviation in the camera Run, each sample of every waveform is corrected by subtracting a value B·g(T, x). Where T is the temperature of the ASIC the event was registered in and B a scaling factor. The polynomial $g(T_{near})$ of the temperature T_{near} closest to a parameterized temperature is chosen. B is used to specify the largest possible correction.
The correction is greatest around 1200 mV or 300 p.e., assuming 4 mV/p.e. [17] and modules with the highest temperatures. To see the effect of the largest observed corrections Run43479 with an expected illumination level of 318.97 p.e is selected. For this Run module 28 in the camera shows the highest temperature T = 43.21°C of all camera modules. For this module, the corrections are applied for B between $0-80$ with a step-size of 5. The resulting charge spectrum for such large amplitudes is Gaussian. The charge spectrum of Run43479 for module 28 channel 0 for B = 0 can be seen in Figure 30 below.

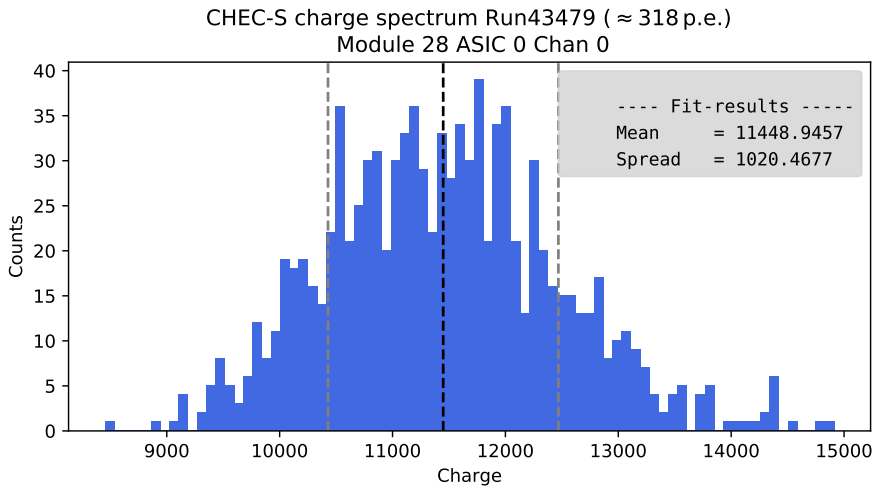

Figure 30: Charge spectrum of CHEC-S Run43479 (≈ 319 p.e.) for B = 0.

The mean and the standard deviation are determined for each scaling factor B. The mean and spread of the charge spectrum for module 28 ASIC 0 Channel 0 can be seen in Figure 31 below.

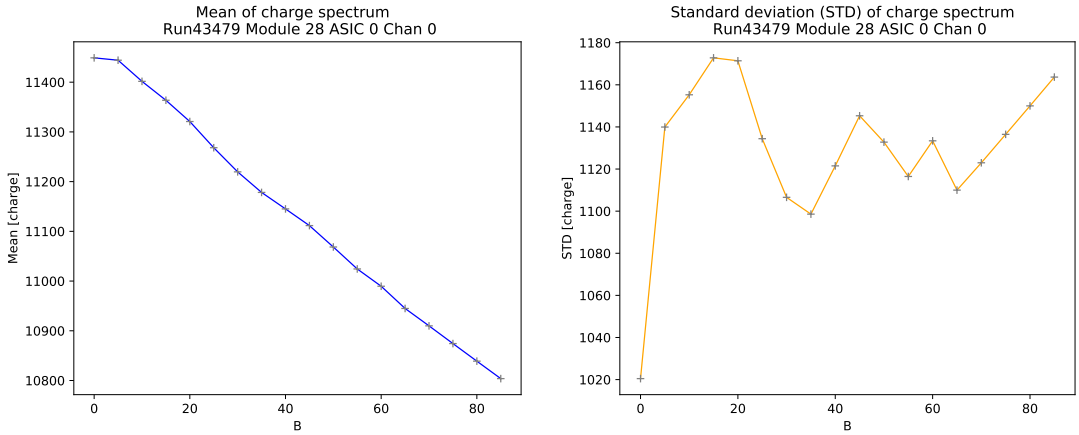

(a) Mean of charge spectrum Run43479 module 28 ASIC 0 Channel 0.

(b) STD of charge spectrum Run43479 module 28 ASIC 0 Channel 0.

Figure 31: Mean and standard deviation (STD) of charge spectrum Run43479 (average illumination level of 318.97 p.e) module 28 ASIC 0 Channel 0 for different scaling factors B.

As seen in Figure 31 above, the mean of the charge spectrum shifts towards lower values for increasing scaling factor B. The deviation plots shown in Appendix A.6 suggest that expected scaling parameters could lie anywhere between $B = 30 - 80$.

In the case, that B = 80 the mean of the charge spectrum needs to be shifted by 383.7713 mVns or 16.4462 p.e. (5.16%) to be at the at the correct position as suggested by the parameterized deviation plot. For B = 0 no correction is applied and a jump in the standard deviation of the charge spectrum can be observed when going to non zero B values. After the initial jump the standard deviation fluctuates but remains rather stable. This process is repeated for Run43502 with an average illumination level of 20.13 p.e and the result can be seen in Figure 32 below.

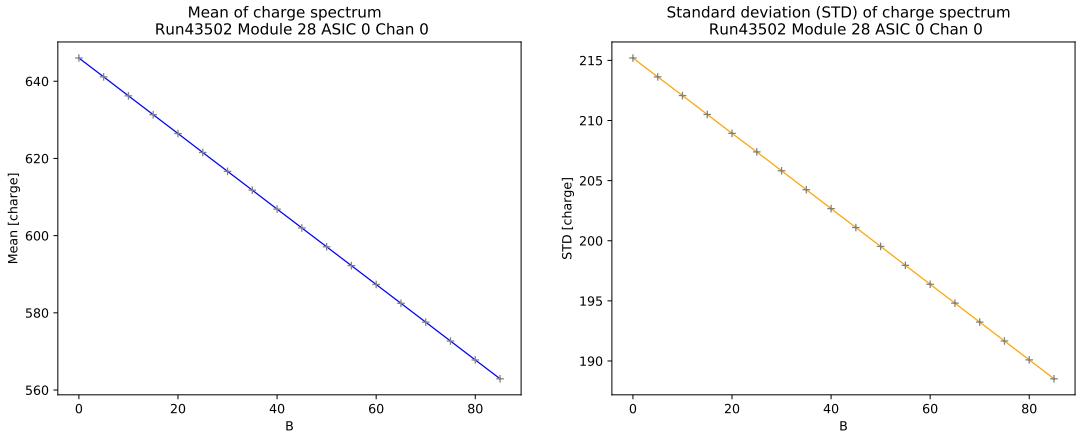

(a) Mean of charge spectrum of Run43502 module 28 ASIC 0 Channel 0.

(b) STD of charge spectrum of Run43502 module 28 ASIC 0 Channel 0.

Figure 32: Mean and standard deviation (STD) of charge spectrum Run43502 (average illumination level of 20.13 p.e) module 28 ASIC 0 Channel 0 for different scaling factors B.

Run43502 shows a similar behavior for the mean of the charge spectrum with a deviation of 3.4013 p.e. or 16.90% for B = 80 while the standard deviation also decreases. From this estimation one can conclude that without correcting for the temperature dependency of the transfer-functions illumination peaks of the charge spectrum could be identified incorrectly by somewhere between $\approx 5\% - 16.90\%$ with the shift increasing towards lower levels of illumination.
These spectrum peak shifts contribute to the total charge resolution of the camera and due to their magnitude the effect of the temperature dependent transfer-function on the total charge resolution is investigated further for a single module. The fractional charge resolution $\Delta Q/Q$ of module SN0024 at 23°C has been calculated by David Jankowsky using Equation 2 below [21].

$$\frac{\sigma_I}{I} = \frac{\Delta Q}{Q} = \sqrt{\sigma^2_{\text{TARGET}} + \frac{(1+\text{ENF})^2}{Q} + \frac{T_{\text{Int}} \cdot \text{NSB}_{\text{Rate}}}{Q^2} + \sigma^2_{\text{sys}}} \tag{2}$$

Here σ_I/I is the fractional intensity resolution, σ^2_{TARGET} is the fractional charge resolution of TARGET, ENF = 0.2 the excess-noise factor, $T_{Int} = 5\,ns$ the integration time and σ^2_{sys} the remaining systematic errors which are assumed to be zero [21]. The term (1+ENF) includes the Poisson limit. NSB_{Rate} was chosen to be 125 MHz. The fractional charge resolution for module SN0024 is calculated for a multitude of charges Q. However, only a CTA requirement for the fractional intensity resolution exists [17]. Due to camera restrains a detected charge of 1 p.e. = 4 photons in terms of Intensity. Thus, the charge Q can be rescaled to Intensity I.

Using this information one can compare the calculated fractional intensity resolution of the module at 23°C to the requirement set for CTA. To estimate the effect of an ambient temperature change from 23°C to 50°C on the compliance with the CTA requirement one uses the deviation-plot for module SN0024. The latter shows the deviation relative to 20°C which is close to the temperature at which the fractional intensity resolution is calculated. The absolute percentage deviation of the transfer-function relative to the input amplitude is calculated and can be seen in Figure 33 below.

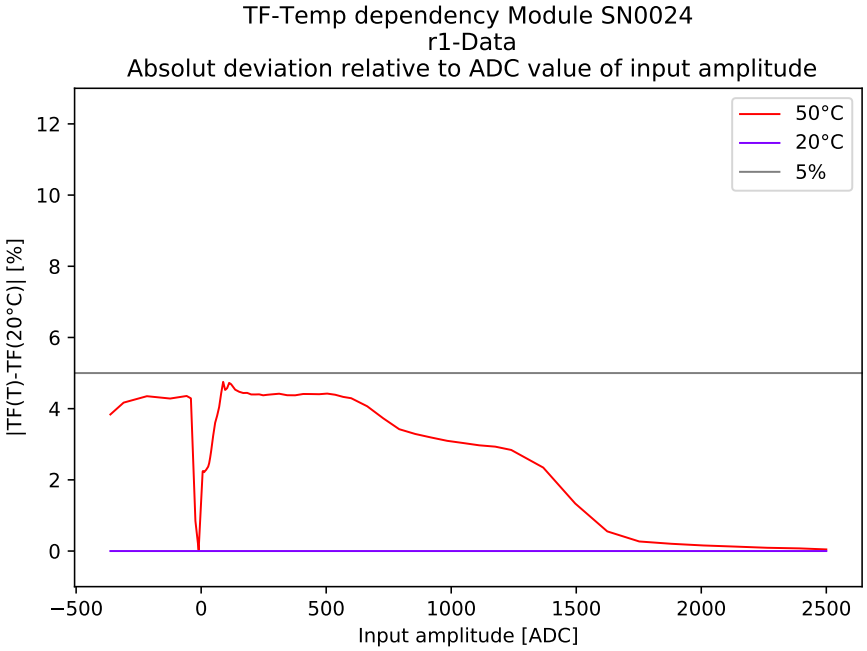

Figure 33: Absolute percentage deviation of the mean transfer-function at a given temperature TF(T) from TF(20°C), the one recorded at the reference temperature, for module SN0024 using r1-data.

The intensity I is calculated for each input amplitude shown in Figure 33 above and the corresponding percentage error is used as the systematic error σ_{sys} in Equation 2 for the relative intensity resolution.

The result can be seen in Figure 34 below which shows the estimated shift of the modules fractional intensity resolution after changing the ambient temperature from 23°C to 50°C with highlighted CTA requirement.

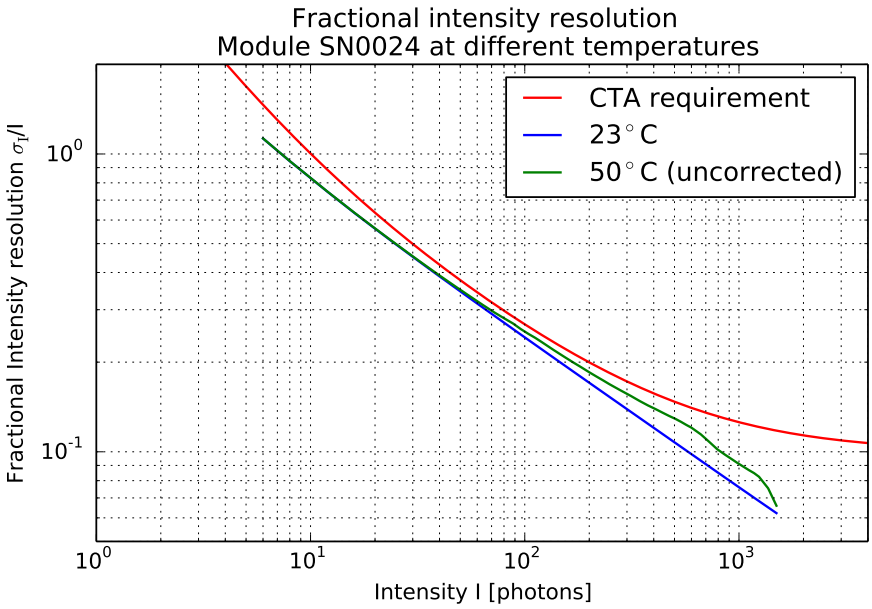

Figure 34: Module SN0024 fractional intensity resolution at 23°C (David Jankowsky) and 50°C when no correction is applied with highlighted CTA requirement [22].

As seen in Figure 34 above, the estimated fractional intensity resolution for module SN0024 at 50°C still fulfills the CTA requirement despite showing a significant increase with Intensity. Especially for small intensities between $11 - 130$ photons the estimated fractional intensity resolution comes close to crossing the CTA requirement. However, the possibility that other modules may show larger deviations cannot be ruled out and may result in some modules no longer fulfilling the CTA requirement. Also other not yet known systematics may further increase the deviation. The analysis conducted in this Section suggests that the fractional intensity resolution of the camera is also affected by the temperature dependency of the transfer-functions and for some modules might lie above the CTA requirement especially for small amplitudes. Thus, a method is required to correct for this effect.

6 Origin of temperature dependency

The origin of the transfer-functions temperature dependency needs to be understood to correct this effect not only successfully but effectively. Several components on-board the module might show a temperature dependent behavior. The components of the module that would contribute the most to the observed temperature dependent behavior are examined in the upcoming Sections. Since some modules had to be sent back to MPIK in Heidelberg other modules are used in the upcoming Sections.

6.1 Temperature dependency of transfer-functions using r0-data

The r1-data used for the deviation plots in Section 3.2.4 does not show all effects of the temperature dependency. To get a more complete view, r0-data must be used. This type of data is not pedestal calibrated and therefore also includes changes that would otherwise not be visible.
The necessary data for the transfer-functions is extracted via a fit to the waveforms of the r1-data as described in Section 3.2.4. This however is problematic for r0-data. As explained in Section 3.2.3, the pedestal calibration removes cell-to-cell variations as well. These variations greatly reduce the quality of the fit or make it completely impossible in the case of small input amplitudes where the peak might not even be visible (compare Figure 20a). As a workaround, both the r1- and r0-data sets are used. While the r1-data is utilized to calculate transfer-functions as described in Section 3.2 the peak positions within the read-out window are written to file. These saved peak positions are looked up in the non-calibrated r0-data and the ADC-value of the corresponding sample is stored. Thus, no fitting is required. The process of calculating the data for the deviation-plots remains the same. The result for module SN0072 can be seen in Figure 35 below.

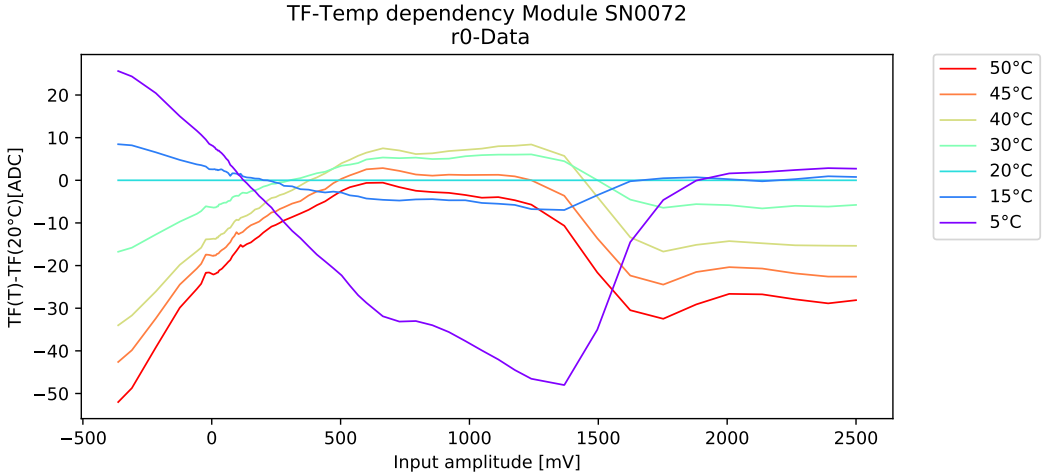

Figure 35: Deviation of the mean transfer-function at a given temperature TF(T) from TF(20°C), the one recorded at the reference temperature, for module SN0072 using r0-data.

The shape of the deviation, seen in Figure 35 above, for a given temperature remains the same when transitioning from r1- to r0-data. The missing pedestal calibration can be seen for all temperatures since the deviations do no longer coincide at the pedestal. This process is repeated with the three other modules SN0040, SN0038 and SN0024 and different temperature ranges. The result for SN0040 can be seen in Figure 36 below and those of the other modules can be found in Appendix A.6.

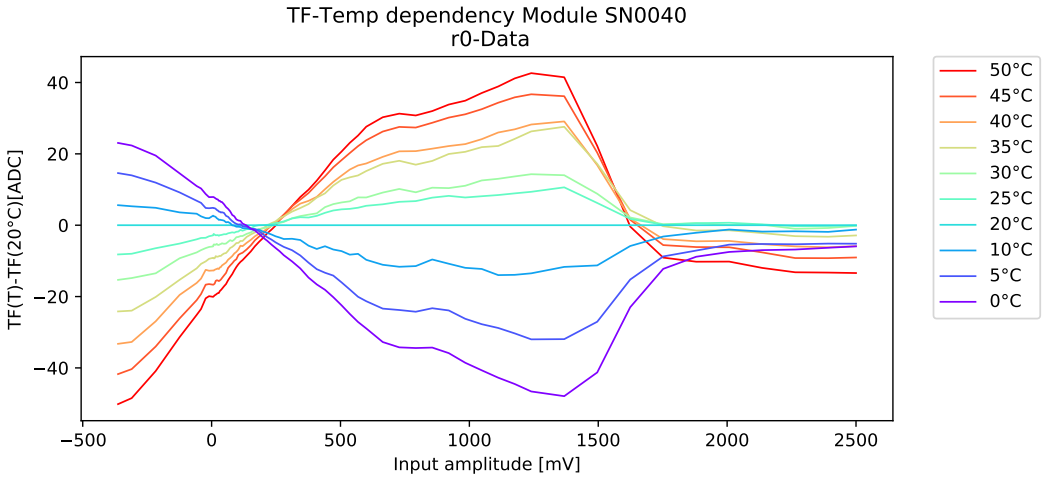

Figure 36: Deviation of the mean transfer-function at a given temperature TF(T) from TF(20°C), the one recorded at the reference temperature, for module SN0040 using r0-data.

The other tested modules show a similar behavior as module SN0072 with a visible pedestal shift. This hints towards a temperature dependence of the digitized pedestal.

6.2 Temperature dependency of the pedestal

As seen in Figure 35 and Figure 36 above, the ADC-counts at the pedestal change with temperature. Assuming that no other parts of the digitization chain is affected by temperature change a possible origin of this behavior would be a temperature dependent pedestal voltage. This would influence the position of the signal on a per channel basis and therefore the values of the transfer-function. For this measurement, module SN0072 is used. The pedestal voltage of each channel is measured at test-points on the module using a digital multimeter. Data is taken between 20°C - 50°C with a step-size of 5°C. After every temperature change the module is again given sufficient time to thermally stabilize. The temperature of the modules primary board over time can be seen in Figure 37 below.

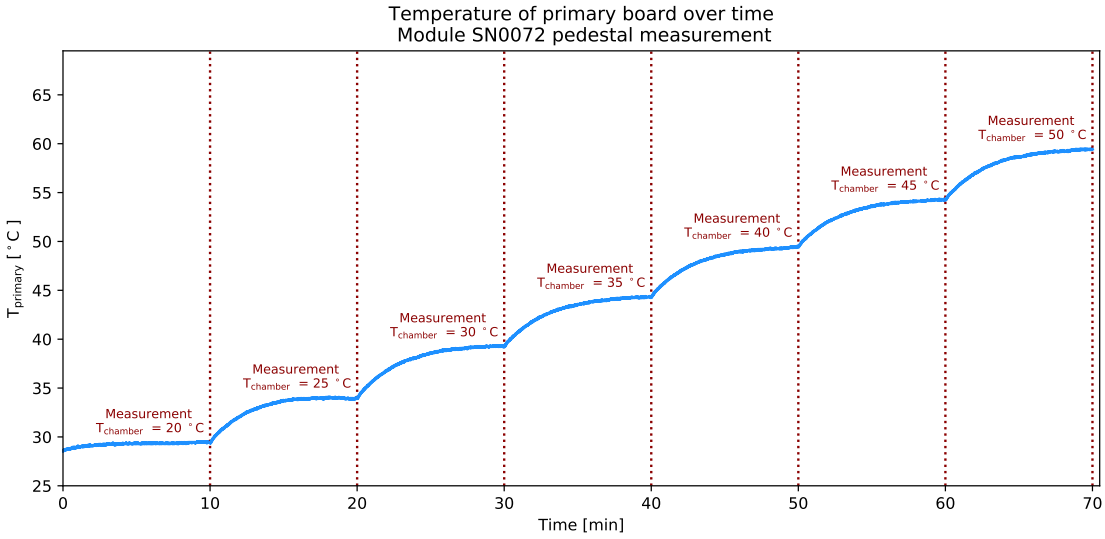

Figure 37: Module SN0072 primary board temperature over time with highlighted positions where the measurement starts.

The dotted lines in Figure 37 above indicate where the measurement for a given temperature took place. The pedestal voltage is measured 100 times at these points and the mean as well as the standard deviation is calculated. The procedure is repeated for five consecutive channels starting with channel 0 of ASIC 0. The results can be seen in Figure 38 below where the standard deviation is used for the error bars.

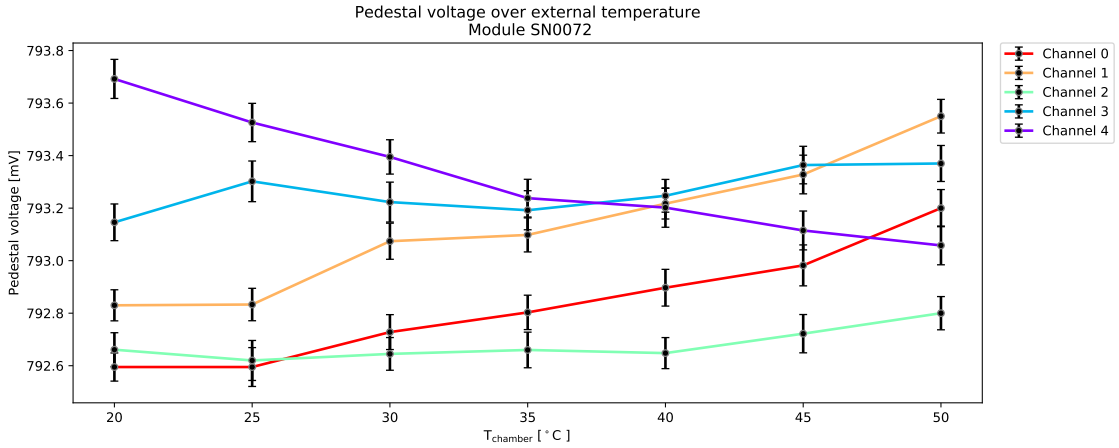

Figure 38: Pedestal voltage of channel $0-4$ for module SN0072 ASIC 0 over temperature of the temperature chamber.

From the data shown in Figure 38 above no general trend can be identified. The largest deviations for each channel D_{max} are calculated and can be found in Table 1 below.

Channel	$\mathbf{D_{max}}$ **[mV]**	$\mathbf{D_{max}}$ **[%]**	$\mathbf{D_{max}}$ **[ADC-counts]**
0	0.61	0.08	1.5
1	0.72	0.09	1.8
2	0.14	0.02	0.4
3	0.22	0.03	0.6
4	−0.61	−0.08	−1.5

Table 1: Largest observed pedestal deviation D_{max} for module SN0072 measured in the temperature range 20°C - 50°C.

To calculate the deviation D_{max} in ADC-counts, as seen in Table 1 above, one assumes 0.4 mV/ADC-count. This is an approximation which comes close to the actual value that will be determined in a later Section. From the deviation plot of module SN0072, as seen in Figure 36 above, one expects a pedestal change of ≈ 20 ADC-counts between 20°C and 50°C. Thus, the observed shift in pedestal voltage cannot explain the observed, digitized pedestal shift in the deviation plots. The latter exceeds the measured one by more than an order of magnitude.
With a mean deviation of -0.03 ± 0.06 ADC-counts for four channels it can be concluded, that the pedestal voltage is not dependent on the temperature when calculating the mean transfer-function. Ruling out this possible source, other components must be the origin of the observed temperature dependency of the transfer-function.

6.3 Temperature dependency of the supply voltage

Another possible source for the temperature dependence is the modules supply voltage. If the supply voltage changes then parts on the module may be operated outside their specifications. Since the sampling and storage process depend on the charging of small individual capacitors this process could be impaired as well. The supply voltage is produced by a Power Management IC (PMIC) voltage regulator (LT3045EDD) [17]. The deviation between output- and set-voltage with temperature, as shown in the data-sheet of this component, can be seen in Figure 39 below.

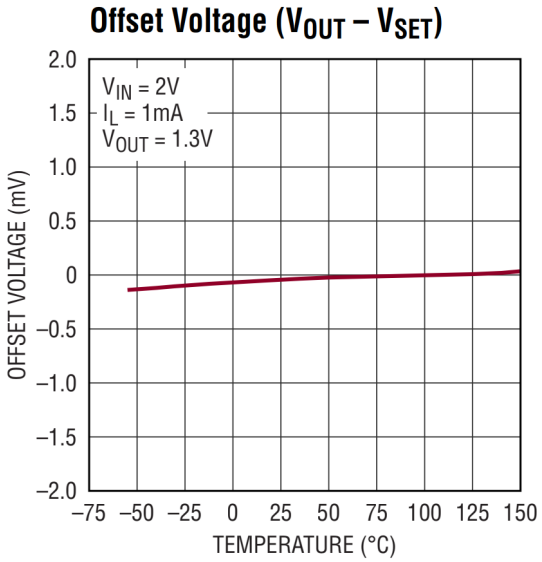

Figure 39: Deviation between output- and set-voltage of PMIC voltage regulator (LT3045EDD) with temperature [23].

The deviation between output- and set-voltage is $\approx 0.05\,\mathrm{mV}$ in the temperature range 20°C - 50°C. Due to the magnitude of the effect this cannot be responsible for the deviation.

6.4 Temperature dependency of Wilkinson ADC

Yet another possible part that could be affected by a temperature dependency is the Wilkinson ADC circuit. As described in Section 2.2.2, it consists of a capacitor for each ASIC, 32 comparator and 12-bit-counter pairs for each channel. For readout, the Wilkinson capacitor is charged with a constant current. This produces a voltage ramp that rises from $0.4\,\mathrm{mV}$ to $2.4\,\mathrm{mV}$ within $8\,\mu\mathrm{s}$ [17]. The capacitor remains charged for $\approx 16\,\mu\mathrm{s}$ (saturation regime) and then discharges. This is the Wilkinson-ramp. The voltage ramp is used as one input signal for all 32 comparators of a given channel. The other inputs are attached to 32 consecutive cells in the storage-array and the comparators output are each connected to a 12-bit counter. When a trigger-signal is issued the Wilkinson-capacitor starts charging and

the 32 counters start counting. A counter stops when the voltage of the voltage ramp is equal to that of the corresponding cell in the storage-array. The resulting counter-value is used as the ADC-value. This process is repeated a total of three times for a readout window of 96 samples. The position of the positive signal peak is always around sample 45 when recording transfer-functions. Thus, the second Wilkinson-ramp is of interest for the observed deviation.

The Wilkinson ADC circuit has direct influence on the digitized value and thus, is a prime candidate as the possible origin of the observed temperature dependency of the transfer-functions. The module SN0024 is used for this analysis. The Wilkinson-ramp for each ASIC can be probed at a test-point on the module. An oscilloscope (Agilent MSO-X 3054A) is used to monitor the Wilkinson-ramp and also store its waveform for later analysis. The probe points of the Wilkinson-ramp are not accessible without dissembling the module. To this end, a special rack has been developed by Duncan Ross (University of London), which allows the three boards of the module to be separated while remaining functional as a whole.

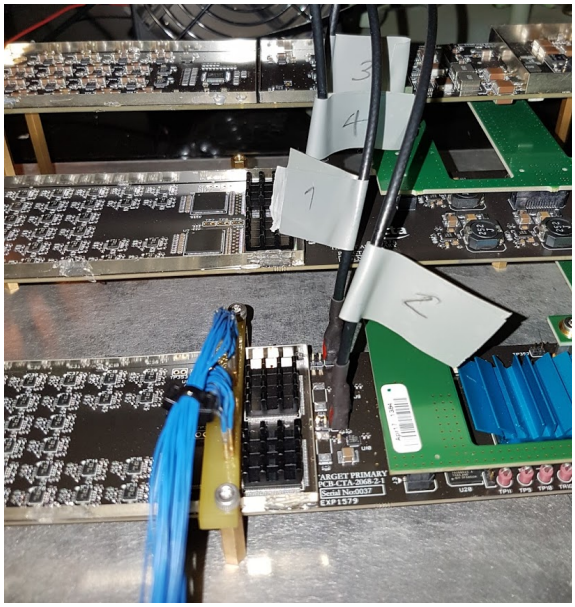

Figure 40: Module SN0024 on special rack that allows separation of the three module boards with cables 1-4 attached to probe points for Wilkinson-ramp of ASIC 0 - 3.

The Wilkinson-ramps are monitored with the aforementioned oscilloscope. When storing the waveform of the Wilkinson-ramp the average is calculated over 500 waveforms to remove noise. Only plots for ASIC 0 are shown in this Section. Plots for all four ASICs can be found in Appendix A.7. The waveform of the Wilkinson-ramp of ASIC 0 at 20°C can be seen in Figure 41 below.

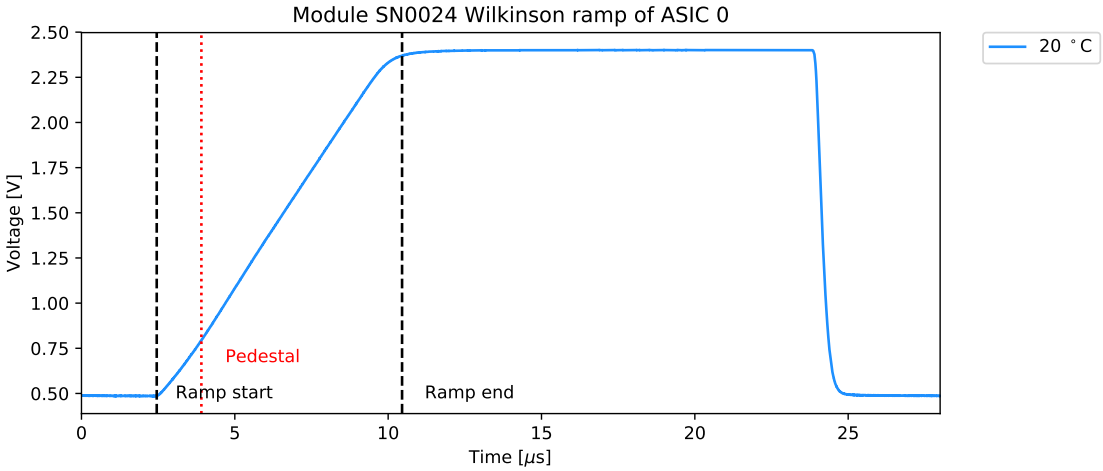

Figure 41: Voltage corrected second Wilkinson-ramp of module SN0024 ASIC 0 with highlighted position of the voltage ramps start and end position as well as the time after which the voltage of the pedestal is reached.

One can also monitor the Wilkinson-ramp directly at the Wilkinson-capacitor. However, this reduces the charging current since the probe introduces an additional path for the current to flow trough. This effect could be minimized by using a probe with high impedance but such a probe was not available at the time of measurement. Therefore, this method is not used.

The Wilkinson-ramp measured at the test point is a copy of the real Wilkinson-ramp signal. The voltages measured at the test points need to be rescaled. The schematic of the Wilkinson circuit states a maximum voltage of 2.4 V [17]. One can determine a correction factor for each ASIC by dividing the maximum voltage value of the measured ramp with the expected voltage. The voltage of the Wilkinson-ramp at 15 µs in Figure 41 is used as the maximum voltage.

From the four acquired and voltage corrected Wilkinson-ramps one can calculate the voltage increase per ADC-count. The start time t_{start} and voltage U_{start} of the voltage ramp is determined using a python script as seen in Figure 41 above. It takes 8 µs for the 12-bit counter to count from $0 - 4095$. Thus, the end time t_{end} and voltage U_{end} can also be determined. From this, one can calculate the slope of the voltage ramp. The resulting values can be found in Table 2 below.

ASIC	t_{start} [µs]	U_{start} [V]	t_{end} [µs]	U_{end} [V]	slope [mV/ADC]	slope [mV/µs]
0	2.4537	0.4868	10.4537	2.3706	0.4599	296.3270
1	2.4572	0.4830	10.4572	2.3335	0.4518	291.6867
2	2.4607	0.4627	10.4607	2.2016	0.4245	275.1960
3	—	—	—	—	—	—

Table 2: Extracted values of the second Wilkinson-ramps of module SN0024.

As seen in Table 2, data of ASIC 3 has not been recorded since it does not work properly on this module. The mean slope of all three voltage ramps is calculated to be (0.456 ± 0.004) mV/ADC as well as (294.0 ± 2.3) mV/µs. Thus, the assumption made in Section 6.2, that the slope is 0.4 mV/ADC is sound and suffices for a quick estimation. To observe a possible change of the Wilkinson-ramp with temperature it is again recorded at 50°C. The settings for the oscilloscope are not changed from the ones used for the measurements at 20°C. Both Wilkinson-ramps for 20°C and 50°C of ASIC 0 can be seen in Figure 42 below.

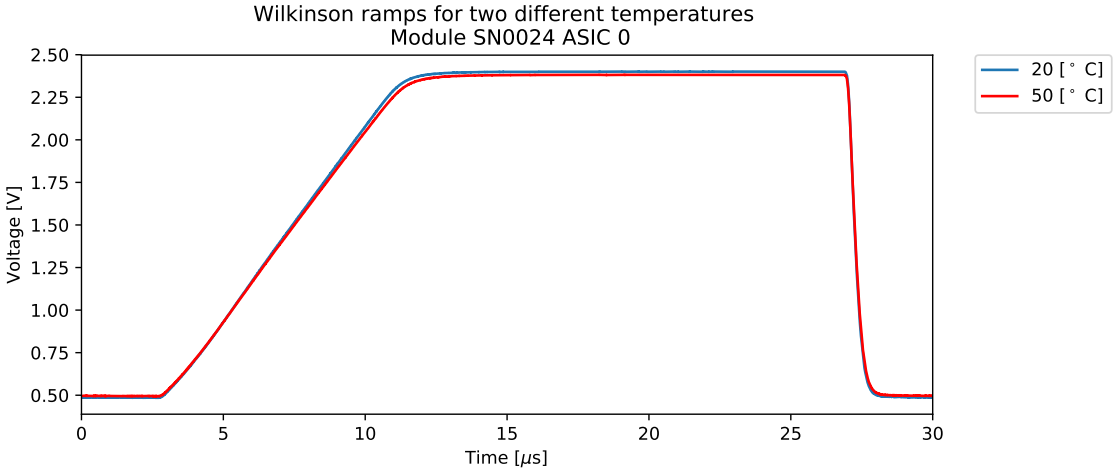

Figure 42: Second Wilkinson-ramp of module SN0024 ASIC 0 at 20°C and 50°C with corrected voltage values.

The Wilkinson-ramps at 50°C start at slightly different times than they did at 20°C. This is likely due to triggering issues of the oscilloscope. Therefore, the time axis for the Wilkinson-ramps at 50°C are shifted in such a way that the ramp starting points coincides with those of the corresponding Wilkinson-ramps at 20°C. As seen in Figure 42 above, the two ramps deviate from one another. To illustrate this deviation in a more visible manner, the difference between the ramp at 50°C and 20°C is calculated by subtracting the ramp at 20°C from the ramp at 50°C. The result for ASIC 0 can be seen in Figure 43 below.

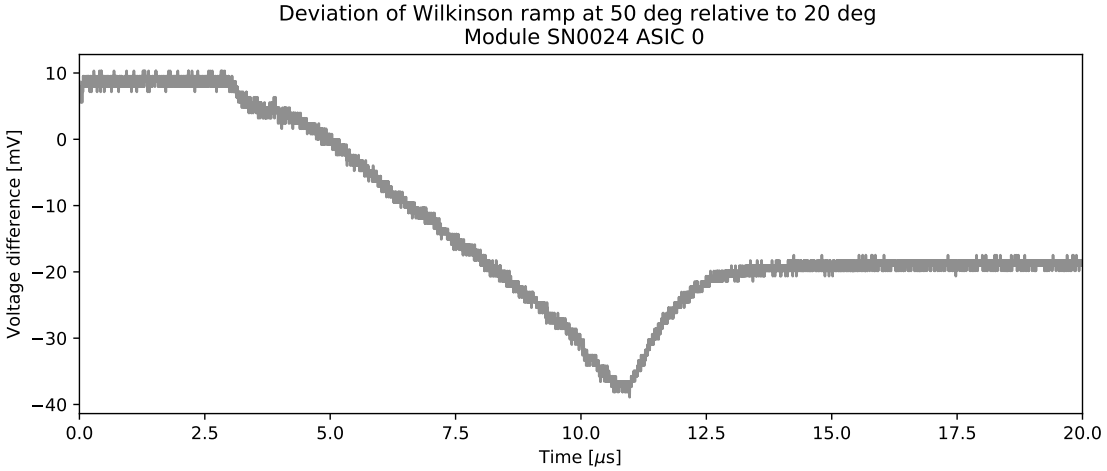

Figure 43: Difference between the Wilkinson-ramps for 50°C and 20°C of module SN0024 ASIC 0 with corrected voltage values.

The deviation seen in Figure 43 above suggests that the Wilkinson-ramp at 50°C begins at a higher voltage than the one at 20°C. This difference decreases over time and reaches a constant value when both Wilkinson-ramps begin to saturate.
From the data shown in Figure 43 one can estimate the effect on the deviation of the transfer-function. Using the slopes calculated in Table 2 above, both axes of Figure 43 are rescaled to the same form used in the deviation plots.

The voltage difference can be directly rescaled to ADC-counts by using the calculated slope [mV/ADC] for the corresponding ASIC. However, the signs of this axis needs to be flipped. This is due to the working principle of the Wilkinson ADC. If the value of the voltage deviation is positive, the Wilkinson-ramp for 50°C lies above the one at 20°C (compare Figure 42 and Figure 43). For a given to-be-digitized voltage value, the ramp for 50°C reaches this voltage value before the ramp at 20°C. So a smaller ADC-value is produced by the ramp at 50°C. Thus, the deviation between the ADC values is negative between 50°C and 20°C for a positive voltage difference and vice-versa.

The time t_{ped} after which the voltage-ramp reached the pedestal voltage is subtracted from the time axis. The time axis is rescaled to input amplitude by using the slope [mV/µs] for the corresponding ASIC. The pedestal time needs to be subtracted because the desired amplitude axis starts at 0 mV input amplitude which corresponds to the pedestal voltage in the r0-data. The result for ASIC 0 can be found in Figure 44 below.

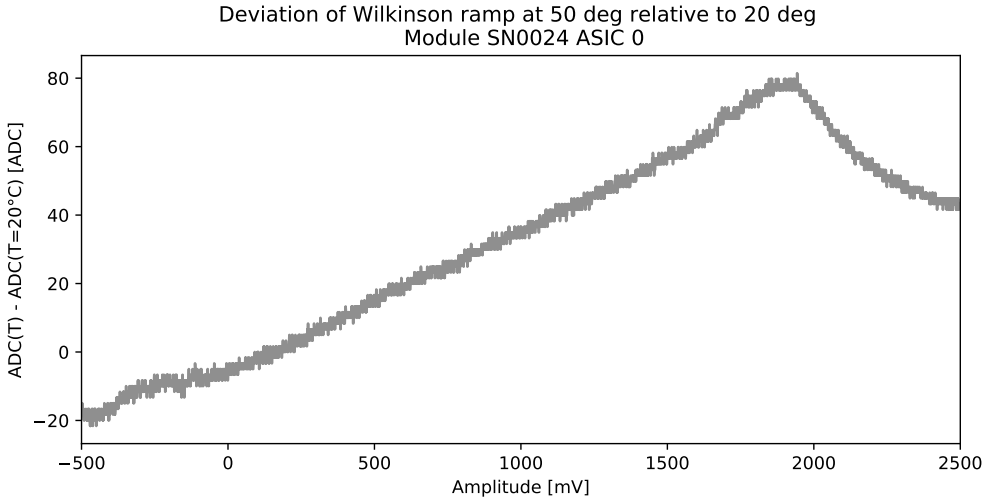

Figure 44: Difference between the Wilkinson-ramps for 50°C and 20°C of module SN0024 ASIC 0 with corrected voltage values. Rescaled to match axis of deviation plots.

The magnitudes of the deviations in Figure 44 above are close to the ones seen in the deviation plot (see Figure 45 below). There is also a similarity in the shape. Both the deviation plot and the estimated deviation start out negative and tend towards larger, positive deviations with increasing amplitude. However, the data illustrated in Figure 44 is just an estimation, relaying on two scaling parameters. These could be influenced by systematic errors in the assumptions made for the Wilkinson-ramps timing.

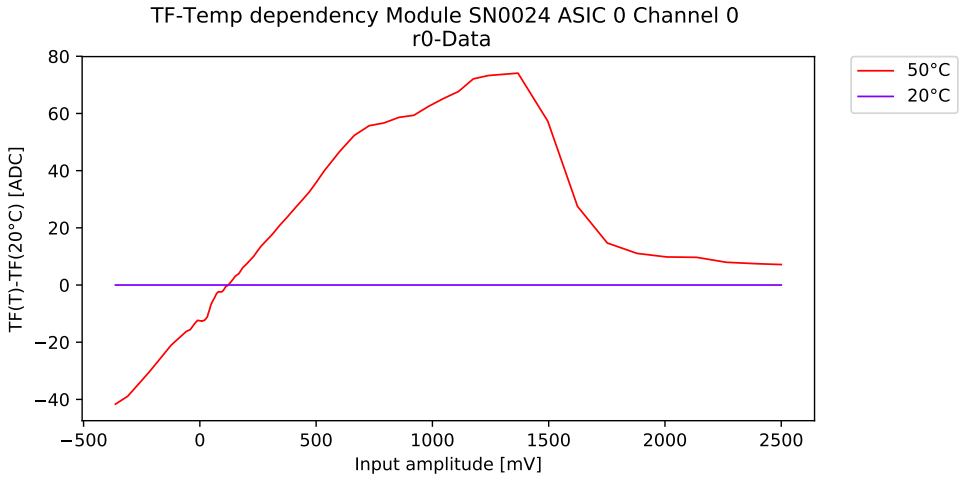

Figure 45: Deviation of the mean transfer-function at a given temperature TF(T) from TF(20°C), the one recorded at the reference temperature, for module SN0024 ASIC 0 channel 0 using r0-data.

This might contribute to the difference in slope seen when comparing both Figure 44 and Figure 45. However, the difference in slope cannot be explained by these systematics alone, which hints towards additional effects influencing the deviation of the transfer-functions. Since the orders of magnitude of the two effects are almost identical, the assumption that this is the most dominant contribution to the temperature dependency of the transfer-functions is not unjustified. One can now try to readjust the Wilkinson-ramps and study the resulting effect on the transfer-functions.

6.5 Readjustment of the Wilkinson-ramps

The observed change of the Wilkinson-ramps with the temperature corresponds with that of the transfer-functions in its magnitude. The hypothesis is made that this is the most dominant effect contributing to the temperature dependence of the transfer-functions. The validity of this hypothesis is now being tested by readjusting the Wilkinson-ramp depending on the temperature. Assuming the hypothesis is indeed correct, the deviation of the transfer-functions should disappear or decrease dramatically. A test is carried out with the temperatures 20°C and 50°C. If successful, the process also works at other temperatures.

TARGET C provides two internal parameters that can be changed to influence the Wilkinson-ramp. The first parameter is "ISEL" with a default value of 2300 DAC-counts. It controls a p-channel metal–oxide–semiconductor field-effect transistor (PMOS) that changes the charging current of the Wilkinson-capacitor. it is able to adjust the slope of the Wilkinson-ramps rising edge, which can be seen in Figure 46a below. The second parameter is called "VDISCHARGE", here referred to as "VDIS", with a default value of 0 DAC-counts. It controls the voltage the capacitor is discharged to at the end of the Wilkinson-ramp, resulting in a vertical shift of the voltage-ramp while keeping its slope mostly unchanged. The change of the Wilkinson-Ramp with VDIS can be seen in Figure 46b below.

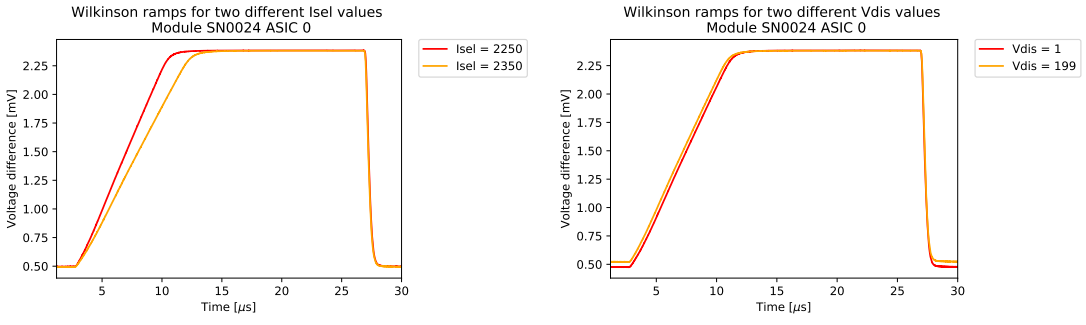

(a) Change of Wilkinson-ramp with ISEL. **(b)** Change of Wilkinson-ramp with VDIS.

Figure 46: Change of second Wilkinson-ramp with different Parameters of ISEL and VDIS for module SN0024 ASIC 0.

Using these two parameters, one can now try to make both Wilkinson-ramps for 20°C and 50°C overlap. To this end, a parameter scan for both parameters is conducted and their respective ideal values determined. The Wilkinson-ramp at 20°C is recorded as a reference using the default value ISEL = 2300. As seen in Figure 42 above, one needs to shift the Wilkinson-ramp down later on. With a default value of 0 one can only increase VDIS which in response can only shift the Wilkinson-ramp upwards (compare Figure 46b above). Thus, a new default value of 100 is chosen for VDIS.

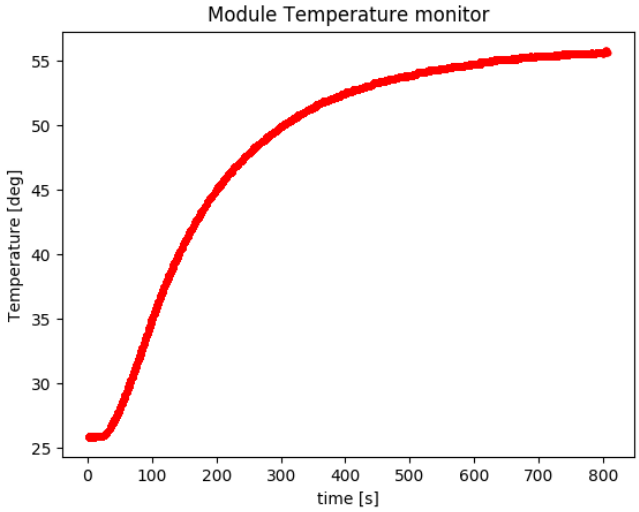

Figure 47: Module SN0024 primary board temperature over time after changing the temperatures chambers temperature from 20°C to 50°C.

After changing the temperature from 20°C to 50°C the module is given 15 min to adjust to the new ambient temperature. As seen in Figure 47 above, this time-span is sufficient. The parameter range between $2250 - 2350$ is scanned first for ISEL with the goal to align the two ramps in parallel. The deviation between both Wilkinson-ramps at 20°C and 50°C for the new default parameters can be seen in Figure 48 below.

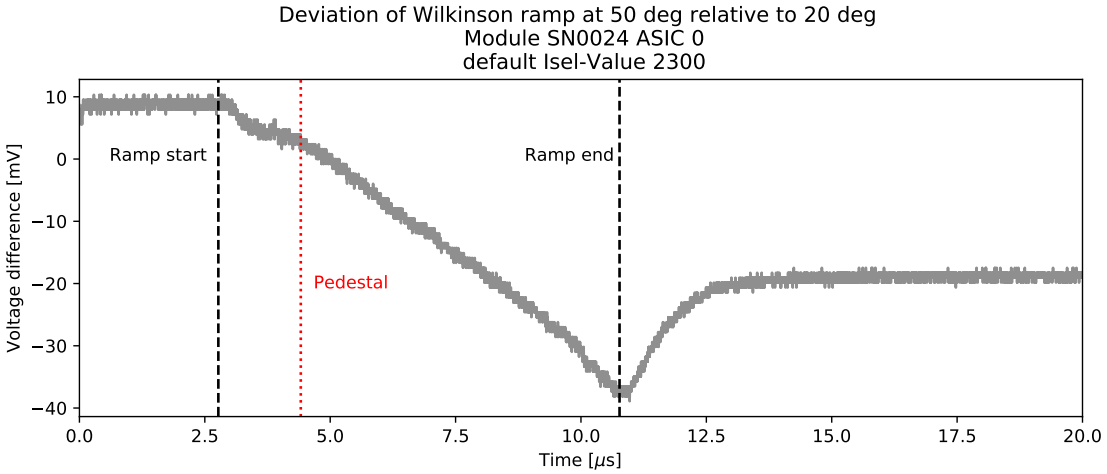

Figure 48: Difference between the Wilkinson-ramps for 50°C and 20°C of module SN0024 ASIC 0 with corrected voltage values and highlighted positions of ramp start, end and pedestal. ISEL 2300 and VDIS 100.

The difference between the ramp at 50°C and 20°C is used as a basis to determine ISELs optimal value for each ASIC. The standard deviation (STD) of all values in Figure 48 between the pedestal and the end of the voltage ramp is a good measure of how parallel the Wilkinson-ramps are. This value is calculated for all scanned ISEL values and the result for ASIC 0 can be seen in Figure 49 below.

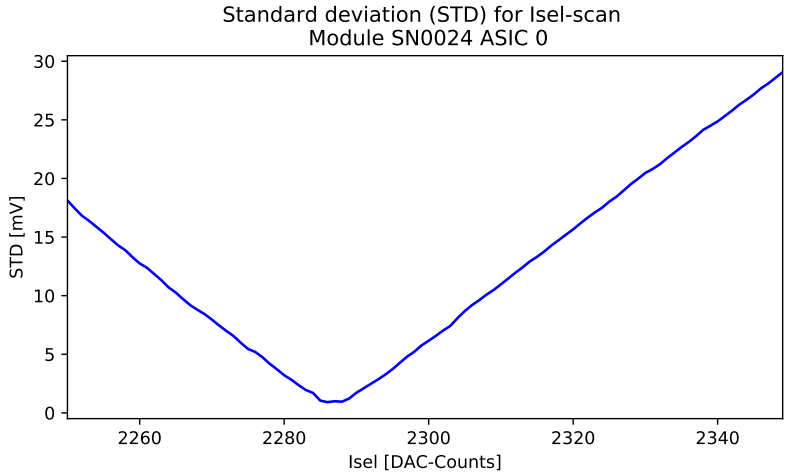

Figure 49: ISEL scan results for Module SN0024 ASIC 0.

The ISEL value with the smallest standard deviation is determined to be 2287 with a residual STD of 0.9167 mV. The resulting difference between the ramp at 50°C and 20°C with this parameter can be seen in Figure 50 below.

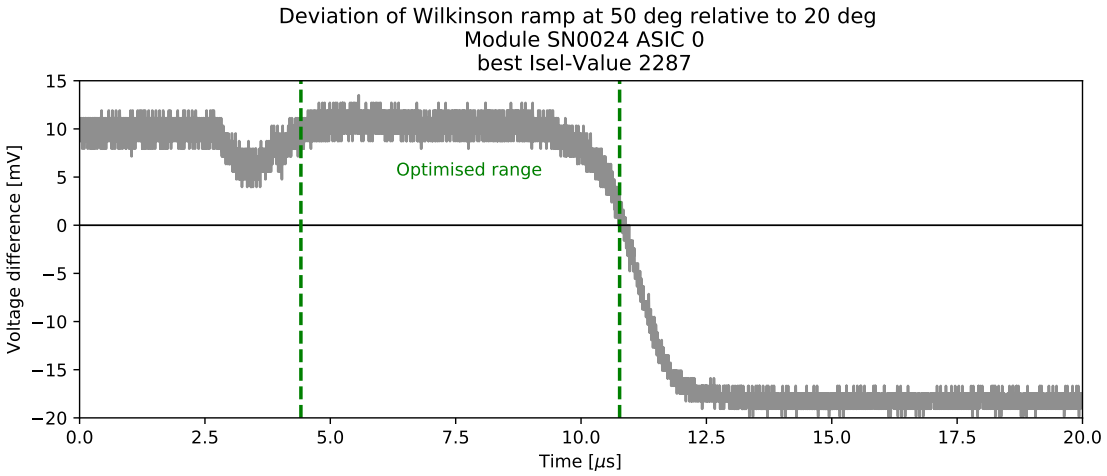

Figure 50: Difference between the Wilkinson-ramps for 50°C and 20°C of module SN0024 ASIC 0 with corrected voltage values and highlighted range used for optimization. ISEL 2287 and VDIS 100.

As seen in Figure 50 above, the voltage difference between the Wilkinson-ramps for 50°C and 20°C is now approximately constant between the pedestal and the end of the voltage-ramp. Thus, the Wilkinson-ramps in this region are parallel.
The analysis of the charge spectrum conducted in Section 5 suggests that especially small levels of illumination (small input amplitudes) are affected by the deviation of the transfer-functions. Thus, the percentage error in the deviation plots around the pedestal needs to be minimized. To this end, another parameter-scan is conducted for VDIS between $0 - 200$. The measurand to be minimized is the voltage deviation at the pedestal. A representation of which, depending on the set parameter, can be seen in Figure 51 below.

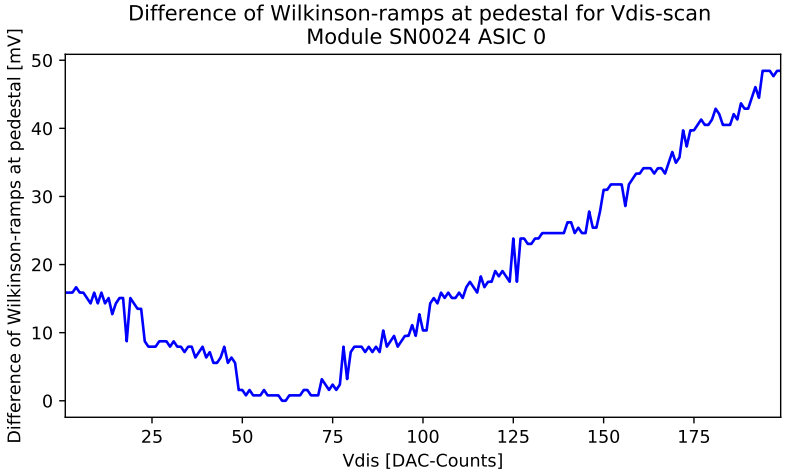

Figure 51: VDIS scan results for Module SN0024 ASIC 0.

For ASIC 0 the VDIS-value with the smallest deviation is 61 with no residual offset. The resulting voltage difference between the Wilkinson-ramps for 50°C and 20°C can be seen in Figure 52 below.

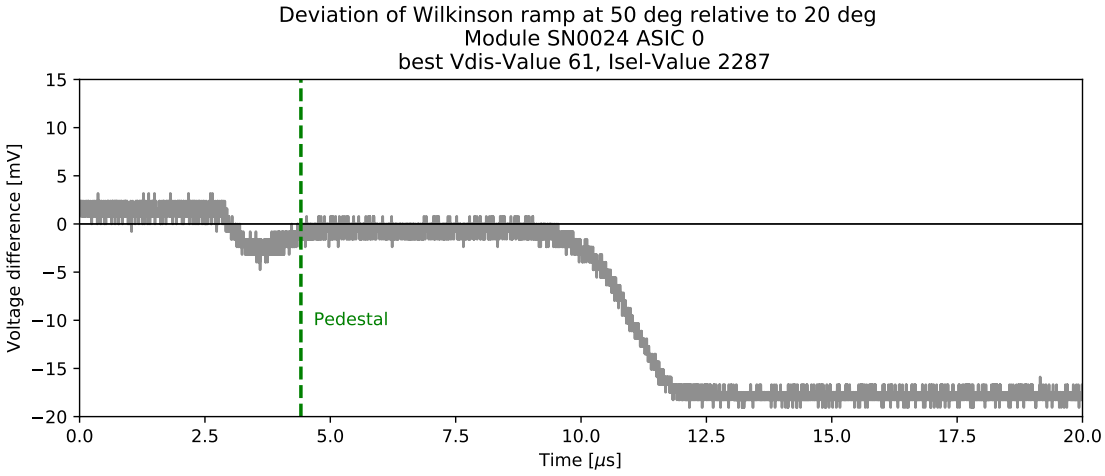

Figure 52: Difference between the Wilkinson-ramps for 50°C and 20°C of module SN0024 ASIC 0 with corrected voltage values and highlighted positions of pedestal. ISEL 2287 and VDIS 61.

As expected, all values in the chosen range between the pedestal and the end of the voltage-ramp now lie close to 0 mV. The complete Wilkinson-ramp with the optimal parameters can be seen in Figure 53 below.

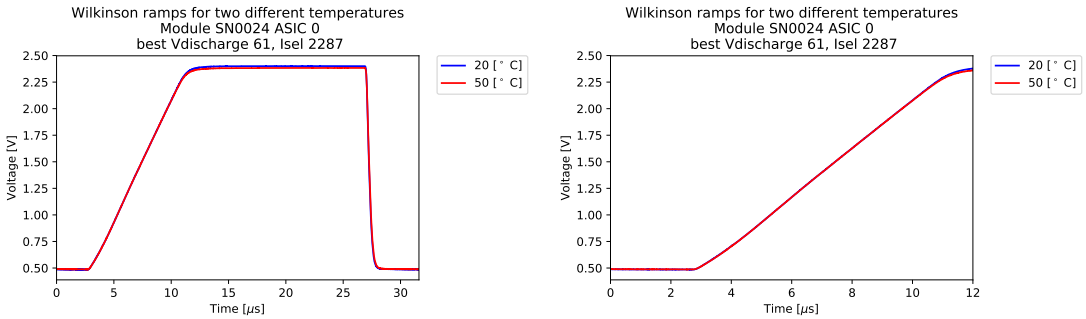

(a) Complete Wilkinson-ramp.

(b) Wilkinson-ramp zoomed in on the voltage-ramp.

Figure 53: Second Wilkinson-ramp of module SN0024 ASIC 0 at 20°C and 50°C with corrected voltage values and optimized ISEL and VDIS values.

As seen in Figure 53 above, the Wilkinson-ramps for ASIC 0 now overlap in the selected region using the newly determined parameter values for ISEL and VDIS. The parameter-scan results for all ASICs can be found in Table 3 below.

ASIC	**ISEL [DAC-counts]**	**Residual STD [mV]**	**VDIS [DAC-counts]**	**Residual offset [mV]**
0	2287	0.9167	61	0.0
1	2288	0.6655	65	1.5836
2	2289	0.6912	73	0.7837
3	—	—	—	—

Table 3: Parameter scan results for ISEL and VDIS of module SN0024 with STD of final ISEL parameter and residual difference of the pedestal to 0 mV.

With these parameters one can now observe the effect on the temperature dependency of the transfer-functions. These are recorded for module SN0024 at 20°C with ISEL 2300 and VDIS 100 as well as at 50°C using the parameters seen in Table 3 above. The measured deviation plot for module SN0024 can be found in Figure 54 below.

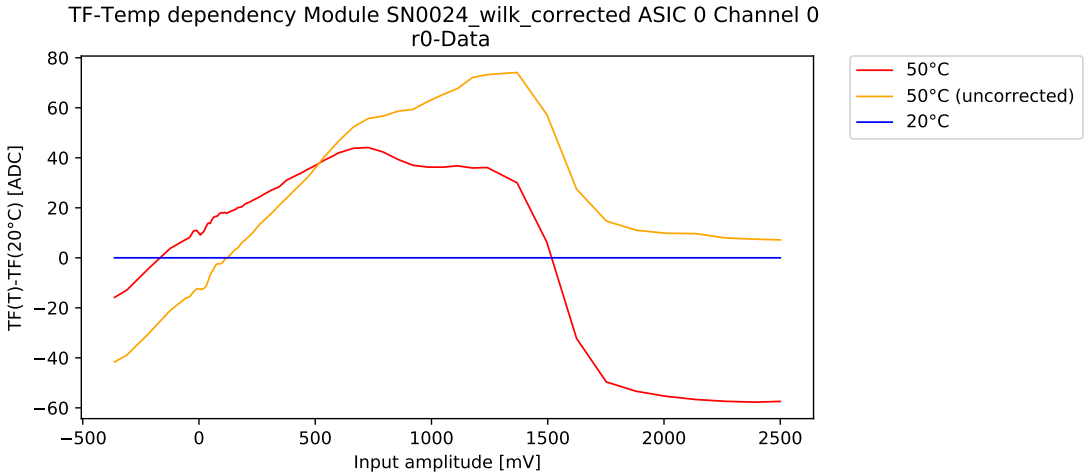

Figure 54: Deviation of mean transfer-function from reference transfer-function at 20°C for module SN0024 ASIC 0 channel 0 before and after using the corrected ISEL and VDIS parameters.

As seen in Figure 54 above, the deviation is not removed completely despite using the corrected parameters for ISEL and VDIS. However, when comparing this result with the uncorrected deviation plot seen in Figure 45 the deviation is approximately halved. Accordingly, the hypothesis put forward at the beginning is not correct and additional effects come into play concerning the deviation of the transfer-functions with temperature. Due to time restrains, the search for other candidates influencing the temperature dependency of the transfer-functions could not be continued. Other possible sources that could be investigated are highlighted in the outlook.

6.6 Hardsync transfer-function

Despite not identifying the exact origin of the temperature dependency another method can be put forward to further decrease the deviation with temperature using the Wilkinson-ramps. This method is described in further detail in this Section.
In the previous Section, the Wilkinson-ramps for both 20°C and 50°C have been aligned by changing ISEL and VDIS. Both these parameters provide a wide parameter space. Thus, it might be possible to compensate the effects of additional processes contributing to the deviation of the transfer-functions by an intentional misalignment of the Wilkinson-ramp. Under ideal circumstances one would record transfer-functions for each combination of ISEL and VDIS and select the values for which the resulting transfer-function deviation would be the smallest. However, this would be a very computational-, storage- and time intensive task. It takes $\approx$ 12 hours to record a transfer-function and calculate the required data with the available hardware as described in Section 3.2. Additionally a storage capacity of $\approx$ 170 GB is required to hold the recorded data. To perform a parameter-scan for ISEL and

then for VDIS in the range used in Section 6.5 would take over 185 days of CPU-time and $\approx 50\,\mathrm{TB}$ of storage for a single module. As an alternative one utilizes the SYNC output of the stand alone board. After 512 full writes to the storage-array, the module sends out a sync signal when the first cell of the storage-array is written to. The data-taking setup, described in Section 3.2 is modified to make use of this. The modules SYNC output is attached to the external-trigger input of the function generator. A signal-pulse is produced when the module has finished a complete storage-array write cycle. Therefore, the peak of the pulse is always located in the same cell of the storage-array. The exact cell is dependent on the trigger-delay set in the function generator as well as the length of the signal-path from the function generator to the ASIC inputs. Once this cell is identified the signal peaks ADC-value can just be looked up in this cell. Bypassing the fits done previously and looking up the ADC-value of a pre-defined sample saves a considerable amount of time compared to the procedure described in Section 3.2. However, by doing it this way, one can only determine the transfer-function of this particular storage-array cell where previously the transfer-functions for all storage-array cells have been determined. One expects no drastic impact because the temperature dependent differences between storage-array cells are small. The ideal values for ISEL and VDIS are determined by this single-cell transfer-function. How these values are determined and how they affect the temperature dependency of the module is now explained and investigated.

With the modified setup, outlined above, data is recorded for 2 s for every input amplitude. This results in ≈ 1000 events for each input amplitude. The cell, in which the signal peak lies needs to be identified before any further analysis. For a subset of 100 events the waveforms of all channels are fitted with an analytic approximation $f(x)$ of the double landau distribution used before via a python script. The fit function $f(x)$ can be found in Equation 3 below.

$$\begin{aligned} f(x) = A \cdot \exp\left[-\frac{1}{2}\left(\frac{x-B}{C} + \exp\left(-\frac{x-B}{C}\right)\right)\right] \\ + D \cdot \exp\left[-\frac{1}{2}\left(\frac{x-E}{F} + \exp\left(-\frac{x-E}{F}\right)\right)\right] \\ + G. \end{aligned} \tag{3}$$

Also an additional offset has been introduced to $f(x)$ to accommodate the pedestal offset in the r0-data. The initial parameters for the peak positions are set by determining the sample within the readout window with the maximum and minimum counts. The fit of a single event can be seen in Figure 55 below.

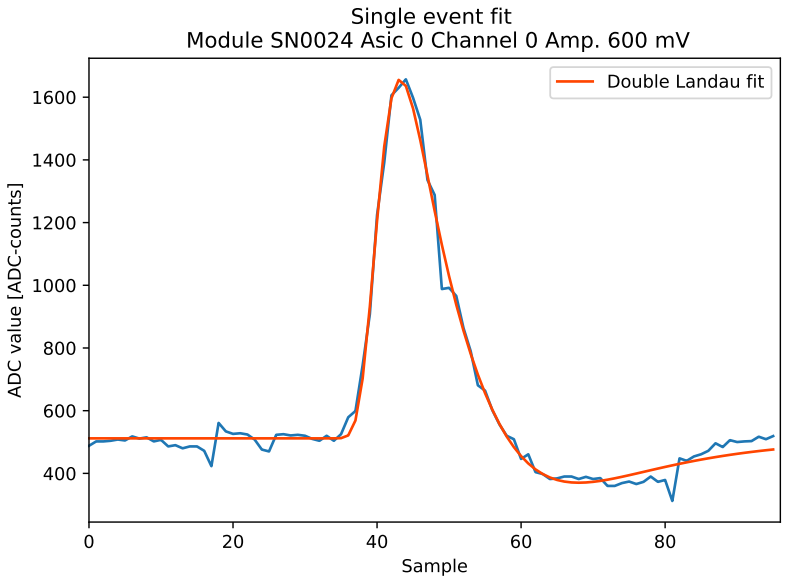

Figure 55: Single event fit for 600 mV input amplitude module SN0024 ASIC 0 channel 0 using r0-data.

The resulting positive peak positions in the storage-array as well as the readout-window for all channels of ASICs 0 - 2 are filled into a histogram which can be seen in Figure 56 below. Data from ASIC 3 is not used since it does not function correctly (compare Section 6.4).

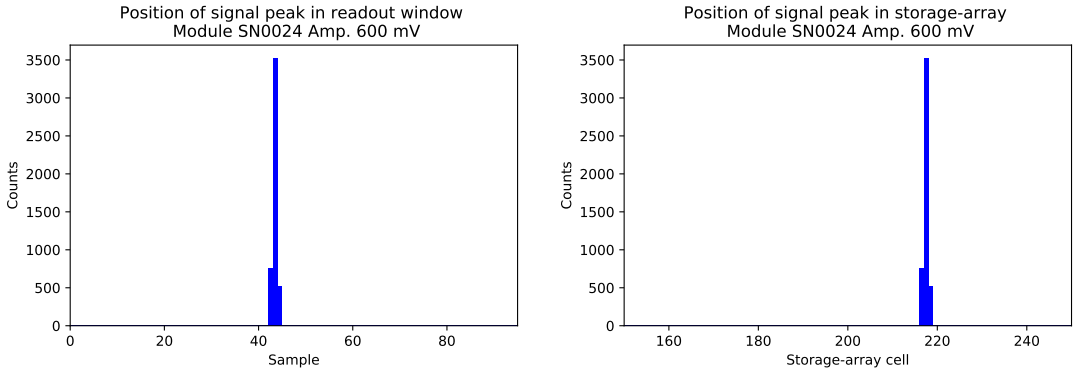

(a) Peak positions in the readout window. **(b)** Peak positions in the storage-array.

Figure 56: Histogram of all fitted peak positions in the storage-array and readout window for the first 100 events of module SN0024 ASIC 0 - 2 channel 0 - 15.

From the data displayed in Figure 56a above, one can see that the peak position is indeed relatively fixed both within the storage-array (see Figure 56b) and the readout window (see Figure 56a).

The sample within the readout window with the highest counts is sample 43 (cell 217 in the storage-array) which is now used to look up the ADC-value for every event. The error made by looking up the peaks value one sample to the right or to the left does not affect the parameter optimization process. The peak values for a given amplitude are determined and a mean value is calculated over all events for every channel. This process is significantly faster and less storage intensive than recording transfer-functions the way described in Section 3.2. This measurement is repeated at 50°C and the resulting transfer-function can be seen in Figure 57 below.

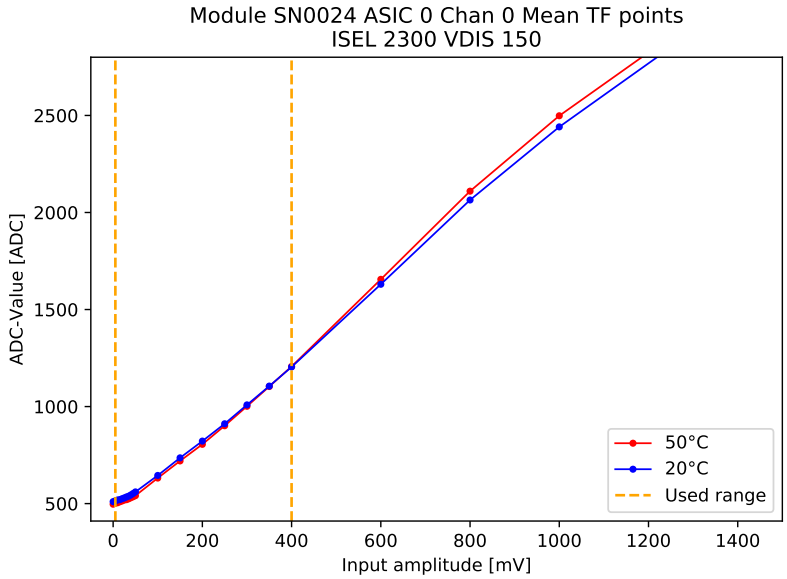

Figure 57: Recorded transfer-function for 20°C module SN0024 ASIC 0 channel 0 cell 217 with ISEL 2300, VDIS 150 and highlighted amplitude range used for optimization.

The calculated deviation of the transfer-functions, shown in Figure 57 above, can be seen in Figure 58 below. Again, the previously observed deviation is visible. A parameter-scan is conducted for ISEL in the range $2250 - 2350$ with the goal of parallelisation of the transfer-functions in the used input amplitude range indicated in Figure 57 above.

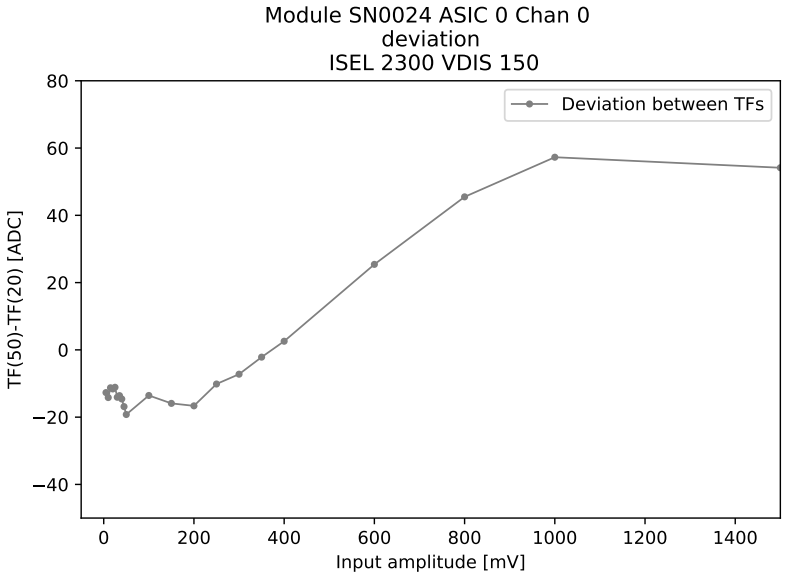

Figure 58: Histogram of all fitted peak positions for the first 100 events of module SN0024 ASIC 0-2 channel 0-15.

For the parameter scan a measure of how parallel both transfer-functions are is introduced. Let A_i be the i-th amplitude in the scan range between $1-400\,\mathrm{mV}$ (highlighted in Figure 57 above). Then one calculates the slope m_{i+1} between two consecutive amplitudes i and i+1 for both temperatures as well as their slope difference Δm_{i+1}. This is repeated for all N amplitudes in the scan-range. The absolute sum over all slope differences is calculated according to Equation 4 below.

$$\Delta S = \sum_{i=1}^{N_{amp}} |\Delta m_i| \cdot w_i \tag{4}$$

$$w_i = \frac{A_i - A_{i\text{-}1}}{A_1 - A_0} \tag{5}$$

Here, w_i is used as a weight to compensate for the changing step size between amplitudes. The parameter-scan results for ISEL and ASIC 0 channel 0 can be found in Figure 59 below.

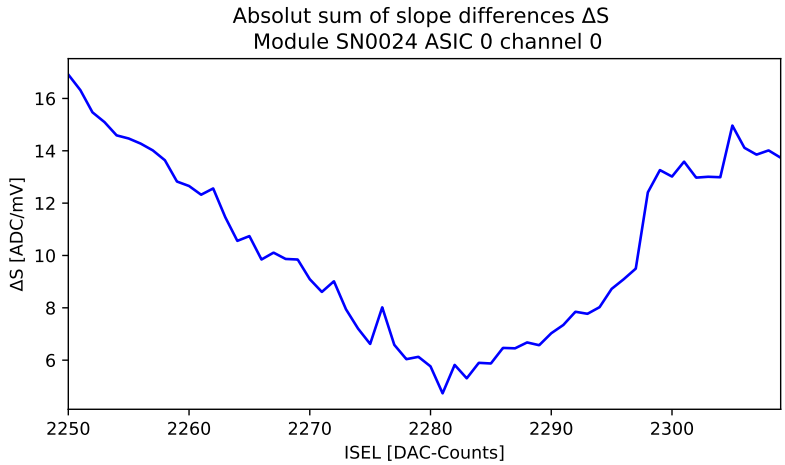

Figure 59: ISEL scan results for module SN0024 ASIC 0 channel 0.

The smallest value for ΔS of ASIC 0 channel 0 is achieved with ISEL 2281 DAC-counts. The transfer-function for this parameter can be found in Figure 60 below.

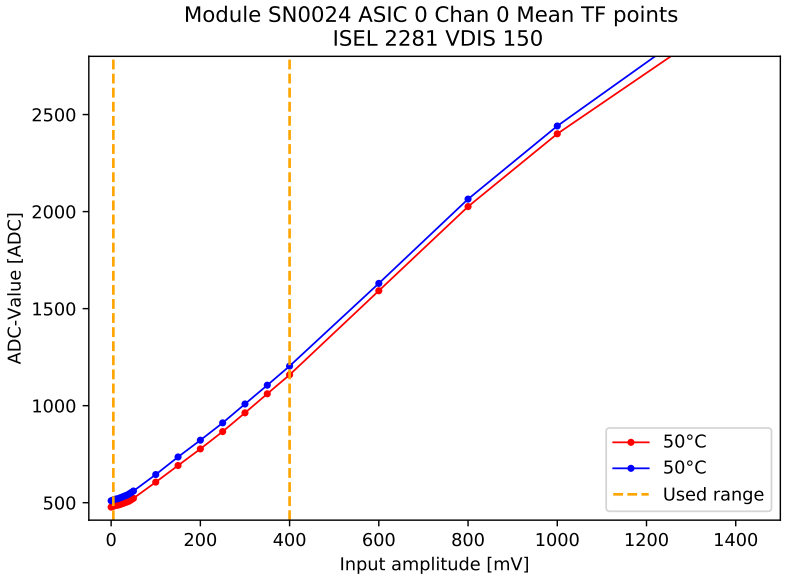

Figure 60: Recorded transfer-function for 20°C module SN0024 ASIC 0 channel 0 with ISEL 2281, VDIS 150 and highlighted amplitude range used for optimization.

As seen in Figure 60 above, the transfer-functions are now parallel to each other. In the next step, the parameter VDIS is adjusted in such a way that the distance between the two transfer-functions is minimized. Let d_i be the distance between the two transfer-

functions at the i-th amplitude. Then one can calculate the weighted distance ΔD of the transfer-functions as seen in Equation 6 below.

$$\Delta D = \sum_{i=0}^{N_{amp}} |\Delta d_i| \cdot \frac{1}{A_i} \tag{6}$$

ΔD is calculated for each VDIS parameter in the scan-range $0 - 200$ DAC-counts. The VDIS scan-results for ASIC 0 channel 0 can be found in Figure 61 below.

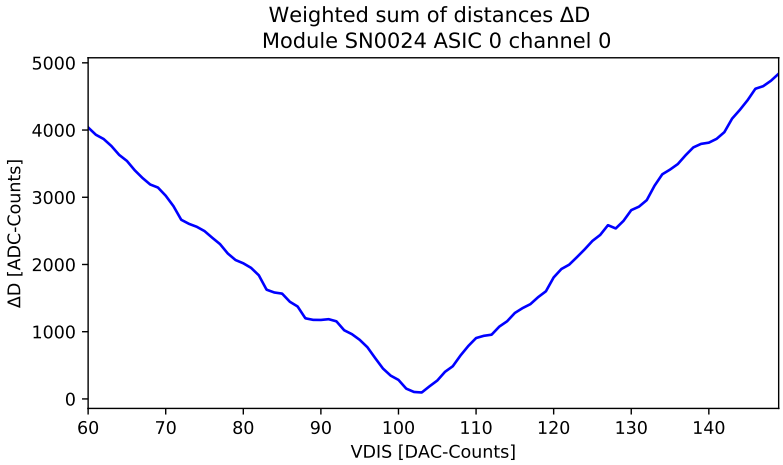

Figure 61: VDIS scan results for module SN0024 ASIC 0 channel 0.

The VDIS with the smallest ΔD is determined to be 103 for ASIC 0 channel 0 with a residual of 96 ADC-counts in the selected amplitude range. The resulting transfer-function for both the determined ISEL and VDIS parameter can be seen in Figure 62 below.

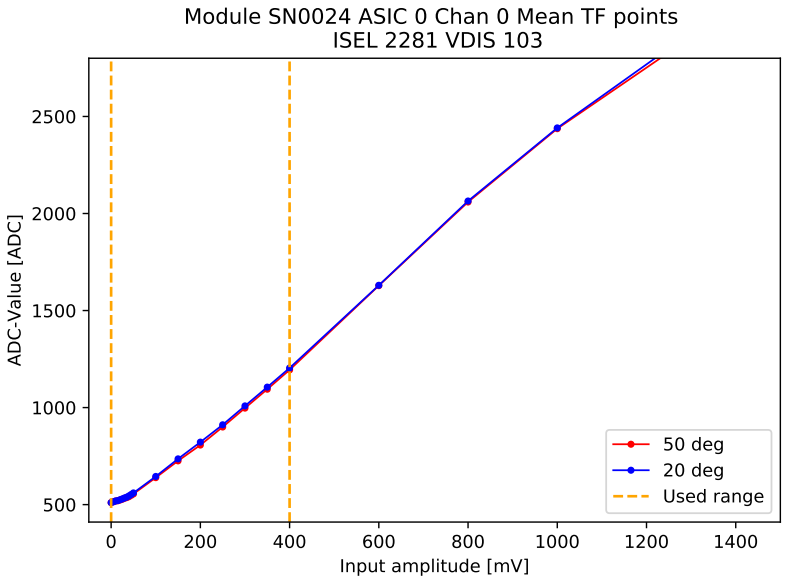

Figure 62: Recorded transfer-function for 20°C module SN0024 ASIC 0 channel 0 with ISEL 2300, VDIS 103 and highlighted amplitude range used for optimization.

As seen in Figure 62 above, the transfer-functions are now very well matched in the selected amplitude range. The acquired parameters as well as the resulting residuals can be found in Table 4 below.

ASIC	**ISEL [DAC-counts]**	**ΔS [ADC-counts/mV]**	**VDIS [DAC-counts]**	**ΔD [ADC-counts]**
0	2281	5	103	96
1	2284	5	109	71
2	2277	6	96	91
3	—	—	—	—

Table 4: Parameter scan results for ISEL and VDIS of module SN0024 with residuals of final ISEL and VDIS parameters.

Transfer-functions for module SN0024 at 20°C with ISEL 2300 and VDIS 150 as well as at 50°C with the parameters listed in Table 4 above are recorded. The resulting mean deviation plot for module SN0024 can be seen in Figure 63 below.

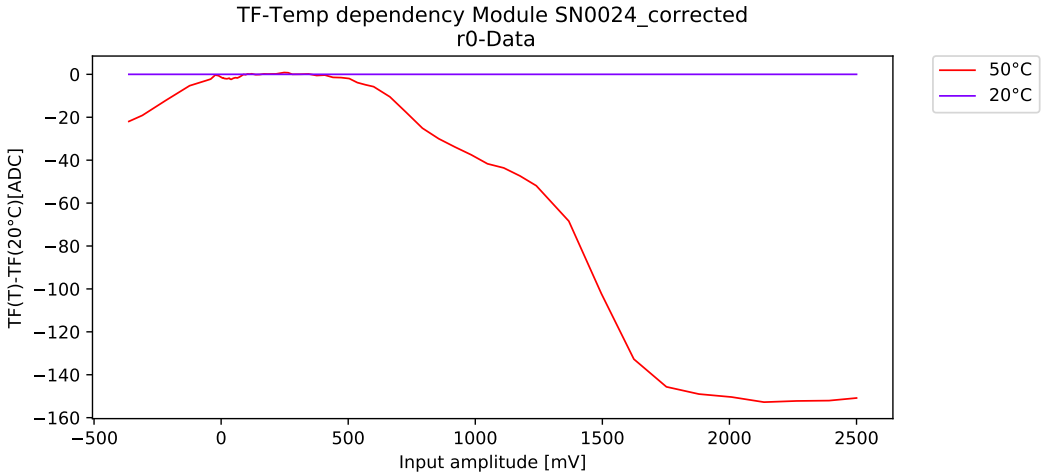

Figure 63: Deviation of the mean transfer-function TF(50°C) from TF(20°C), the one recorded at the reference temperature, for module SN0024 using r0-data.

The deviation of the transfer-functions, Figure 63 above, is greatly reduced in the selected amplitude region. The improvement is more noticeable when comparing the relative deviation with and without the corrected parameters. These can be seen in Figure 64 below.

When comparing both plots shown in Figure 64 below the relative deviation dominantly lies below 5 %. The biggest percentage deviations in both plots differ by more than an order of magnitude. An improvement has occurred, as expected, mainly around the pedestal. In addition, the percentage deviations for negative amplitudes also decreased despite not having been directly taken into account when determining the best parameters. In the case of r1-data the deviation always lies below 4 %. Since the selected input amplitude range can be changed, one can determine different parameter values for ISEL and VDIS depending on the input amplitude range that is to be observed.

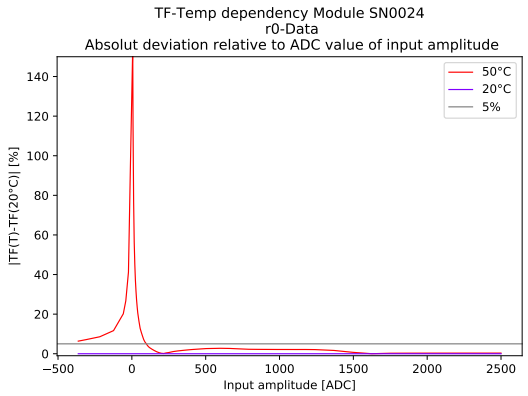

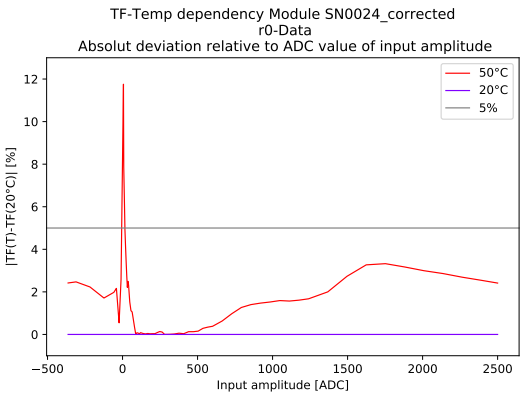

(a) Default ISEL and VDIS parameters values. **(b)** Corrected ISEL and VDIS parameter values.

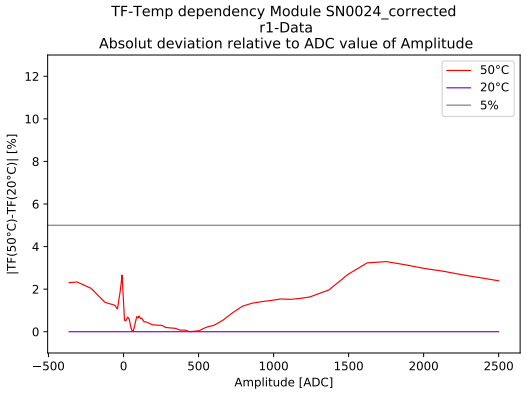

(c) Corrected ISEL and VDIS parameter values with r1-data.

Figure 64: Absolute percentage deviation of the mean transfer-function at a given temperature TF(T) from TF(20°C), the one recorded at the reference temperature, for module SN0024 using r0-data for both the default as well as the corrected ISEL and VDIS parameters.

In Section 5 above, the percentage deviation of module SN0024 is used to estimate the shift of the fractional intensity resolution with temperature. Using the percentage deviation of the same module after correcting for the temperature dependency of the transfer-functions, the improvement that the method investigated in this section yields can be calculated. The result can be seen in Figure 65 below.

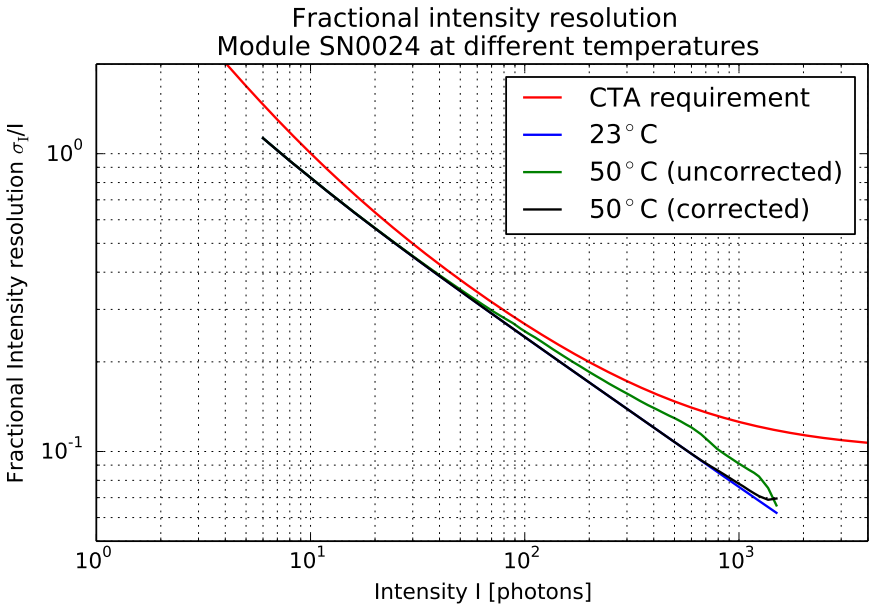

Figure 65: Module SN0024 fractional intensity resolution at 23°C (David Jankowsky), 50°C when no correction is applied and 50°C with new correction as well as highlighted CTA requirement [22].

Despite the fact that the parameter values for ISEL and VDIS are extracted using only the transfer-function of a single cell this method yields very good results and decreases the deviation of the transfer-functions as well as the fractional intensity resolution. The latter now follows the original curve at 20°C up to high intensities and again lies below the CTA requirement. The complete parameter scan, including data taking and evaluation, can be performed in ≈ 30 min. Therefore, this method is not only quick but also effective. The parameter scan can also be carried out with the assembled camera, as the modules do not have to be disassembled. In this case, the function generator is replaced with the LED-flashers onboard the camera housing which can illuminate the SiPM tiles in the assembled telescope.

6.7 Interpolation of temperature dependence

In this Section, another way to compensate for the temperature dependent transfer-functions is explored. As mentioned in the previous Section, the deviation of the transfer-function can easily be removed from stored data when both the board temperature as well as the transfer-function at that temperature is known. This would require recording transfer-functions for every module at a multitude of different temperatures. This however, is an impractical approach both in terms of the measurement and computing time required as well as in terms of storage usage. These problems can be solved by using an interpolation approach.

For this, transfer-functions are recorded at 20°C and 50°C for every module. Assuming a linear behavior of the deviation with temperature, one can utilize linear interpolation to acquire the deviation of a different temperature. The interpolated transfer-function $\mathrm{TF}_{\mathrm{pol}}(\mathrm{T})$ at temperature T can be calculated using

$$\mathrm{TF}_{\mathrm{pol}}(\mathrm{T}) = \frac{\mathrm{TF}(50°\mathrm{C}) - \mathrm{TF}(20°\mathrm{C})}{50°\mathrm{C} - 20°\mathrm{C}} \cdot (\mathrm{T} - 20°\mathrm{C}). \tag{7}$$

To demonstrate this procedure data recorded for SN0040 is used. For this module transfer-functions have already been calculated for a multitude of temperatures and one can compare the deviation-plot resulting from the interpolated deviation transfer-function ($\mathrm{TF}_{\mathrm{pol}}$) with the one resulting from the measured one (TF). A deviation plot showcasing this interpolation for ASIC 0 channel 0 at 30°C can be seen in Figure 66 below.

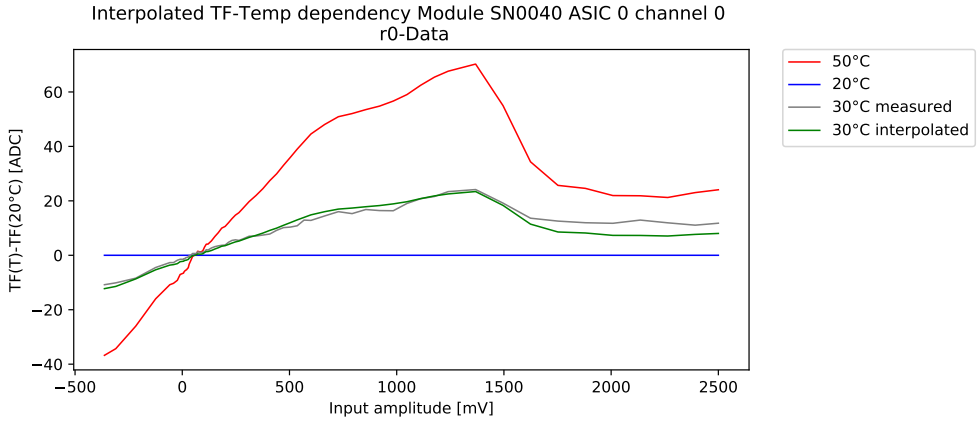

Figure 66: Deviation of the mean transfer-function at a given temperature TF(T) from TF(20°C), the one recorded at the reference temperature, for module SN0040 ASIC 0 channel 0 with interpolated and measured deviation at 30°C.

As seen in Figure 66 above, the deviation-plot for the interpolated transfer-function follows the measured one closely. Thus, the assumption that the deviation for SN0040 scales linearly with temperature is good. This is procedure is repeated with all measured temperatures greater than 20°C. The percentage deviation for all temperatures between the measured and interpolated transfer-function relative to the transfer-functions ADC-value can be seen in Figure 67 below.

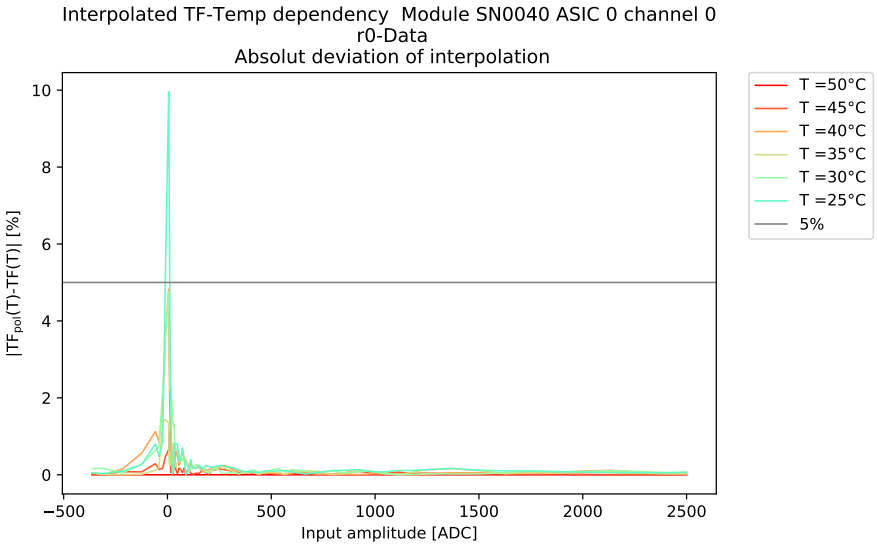

Figure 67: Absolute percentage deviation between the interpolated and measured transfer-function for different temperatures T for module SN0024 ASIC 0 channel 0.

The interpolation error increases towards lower temperatures but produces acceptable results with a relative deviation below 10% for all interpolated temperatures T. However, this methods performance is strongly dependent on the deviations temperature dependency. Non-linear behaviors can be observed for the modules SN0072 and SN0038, as seen in Appendix A.6, which limits the effectiveness of the interpolation method. Despite that, applying some correction of the correct form is better than not correcting for the temperature dependency of the transfer-functions at all. This method can be incorporated into default testing procedure for modules since transfer-functions are already recorded for 23°C and recording another at 50°C does not take too much time compared to the other investigated methods. The required corrections for other temperatures can then be calculated if needed.

A reduction in the temperature dependency of the transfer-functions can be achieved with all investigated methods. The interpolation method explored in this Section should be the easiest to implement for the current prototype camera, despite being less accurate, since only two transfer-functions need to be recorded. The interpolation method will be tested with the prototype camera in the future.

7 Dependency of timing resolution on illumination level

In addition to temperature dependent measurements conducted in previous Sections, the timing resolution of the camera is examined. Its dependency on the level of illumination is of particular interest and is investigated in this Section. At the current time, there has not been a standardized definition for the time resolution of CHEC-S, yet. Thus, a custom definition is presented in this thesis. Again, camera runs are used for this analysis. To record Run data with CHEC-S the camera is placed inside a dark box with a laser on the other end. The distance of the laser as well as its divergence are chosen such that the all pixels of CHEC-S are uniformly illuminated. As a result, the signal of the laser reaches each pixel at the same time for every event. Thus, information about the timing resolution of the camera can be extracted by observing changes of the pulse position within the readout window for a given channel A compared to a reference channel B. For these two channels A and B of CHEC-S the positions t_A and t_B are determined within the readout window on a per-event basis using a fit of the form seen in Equation 3. There might be cases, where the fit does not converge and returns invalid data. To remove these outliers, reasonable cuts on the peak position must be performed.

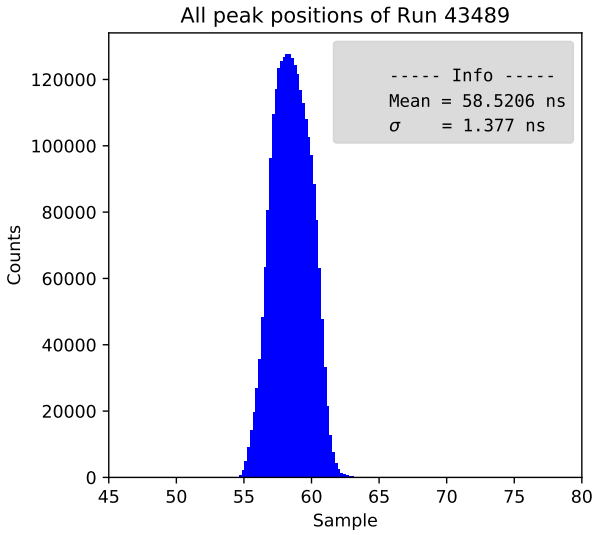

Figure 68: Histogram of all fitted peak positions for Run43489.

From the histogram of all fitted peak positions of Run43489, seen in Figure 68 above, a reasonable cut can be constructed. Only events with fitted peak position $50 < t_{pos} < 70$ are used. It is assumed that fitted peak positions outside this range are due to fails in the fit. Each Run provides the mean level of illumination in units of p.e.. Thus, events with smaller or larger signal may be contained within a Run. The CTA requires a timing resolution of 2 ns for all signal amplitudes larger than 5 p.e. or 20 mV, again assuming 4 mV/p.e.. To validate the compliance with this requirement events with a fitted amplitude

smaller than 20 mV are also neglected. For events passing the established cuts the time difference $\Delta t_{A,B}$ is calculated for each event in the Run-file and filled in a histogram. A pair of example histograms can be seen in Figure 69 below.

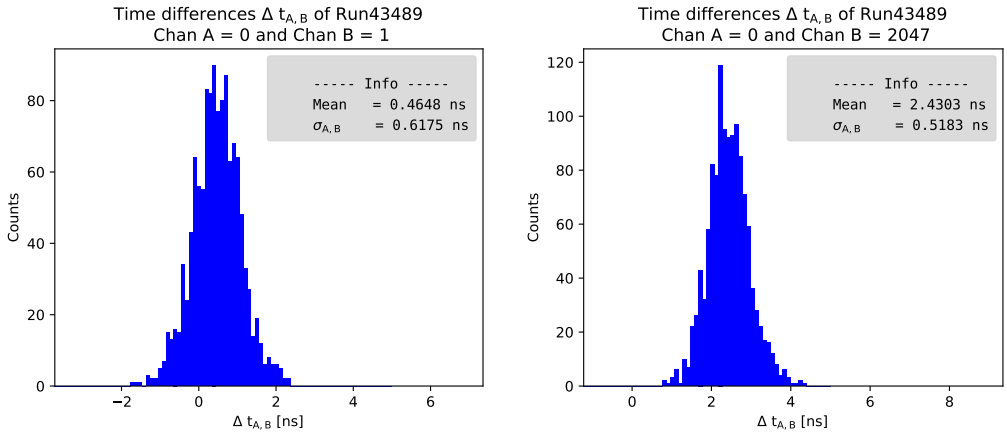

(a) Histogram of time differences $\Delta t_{A,B}$ Run43489 channel A = 0 and B = 1.

(b) Histogram of time differences $\Delta t_{A,B}$ Run43489 channel A = 0 and B = 2047.

Figure 69: Histograms of time differences $\Delta t_{A,B}$ between channel 0 and two other channels for all events of Run43489 with info about the mean value as well as the standard deviation $\sigma_{A,B}$.

The standard deviation $\sigma_{A,B}$ is used as the timing resolution between two given channels A and B. Also $\sigma_{A,B}$ is independent of differences in the signal path lengths between to given channels. These differences are caused by the physical camera- and PCB layout. Since this time difference is constant, it affects only the mean value of the histogram and leaves the standard deviation unaffected. The mean time resolution $\bar{\sigma}_{A,B}$ is calculated over all possible combinations of channel A and B for a given Run. One expects the time resolution to worsen for lower levels of illumination due to the single p.e. resolution of the silicon photo multiplier. The result for different Runs with different mean signal amplitude can be seen in Figure 70 below.

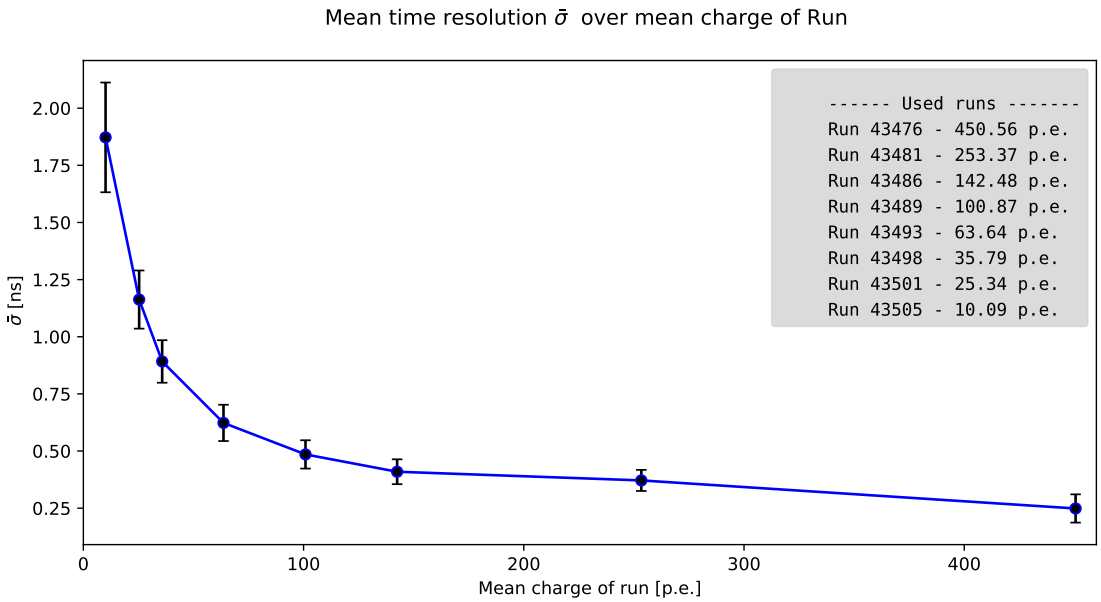

Figure 70: Mean time resolution of CHEC-S $\bar{\sigma}_{\mathrm{A,B}}$ over mean signal amplitude (charge) of run with the standard deviation of $\bar{\sigma}_{\mathrm{A,B}}$ as error bars.

As seen in Figure 70 above, the mean timing resolution worsens towards lower illumination levels as expected. An additional effect that could contribute to the observed decrease in time resolution is the laser used to illuminate the focal plane. The laser pulse consists of a sharp intensity peak ($\approx 50\,\mathrm{ps}$) followed by a relatively long tail ($\approx 2\,\mathrm{ns}$). For lower levels of illumination, the probability to find a photon in the initial sharp peak is lower than for higher illumination levels. Thus, the spread of photon arival times increases towards smaller levels of illumination. As seen in Figure 70 above, the mean timing-resolution still complies with the requirement set for CTA for the investigated levels of illumination. The standard deviation of all timing resolutions for a given Run increases towards lower illumination levels. Here, the spread of the level of illuminations included in the Run increases. As a increasing number of illuminations are contained within the Run, time resolutions between increasingly different illuminations are calculated. Thus, broadening the spectrum of possible values for time resolutions. The exact source for this signal amplitude dependency of the timing resolution should be investigated in future experiments.

8 Conclusion

In the scope of this thesis a temperature dependency of the transfer-functions has been discovered in the tested modules. This temperature dependency influences reconstructed charge spectra of the camera in such a way that peaks in the charge spectrum are shifted and therefore identified incorrectly by up to 16.90% depending on the level of illumination. The fractional intensity resolution calculated for a single module shifts with temperature and without applying a correction for the temperature effects may not meet the CTA requirement. To compensate for the temperature dependency of the transfer-functions three different approaches have been investigated. The most straight forward approach is to take transfer-functions at different temperatures for every module and use these to look up the needed corrections. This, however, is very time and storage intensive but yields the best possible results since the exact deviation is known.
The temperature dependency of the transfer-functions has been traced back to the Wilkinson ADC circuit. The dependency manifests itself as a shift between the Wilkinson-ramps at different temperatures. This can be counteracted by adjusting the two internal parameters ISEL and VDIS. Using these parameters the Wilkinson-ramps can be intentionally shifted such that the transfer-functions deviation in a restricted input amplitude range is effectively removed. This method has proven to be fast as well as accurate with a mean relative residual deviation below 5%. After applying the correction, the deviation of the fractional intensity resolution between 23°C and 50°C for a single module is greatly reduced and fulfills the CTA requirement. This method could also be used in the assembled camera.
The last presented method is a compromise between speed and accuracy. By assuming a linear relationship between the degree of deviation and temperature one can interpolate the deviation for a certain temperature. This requires taking transfer-functions at 23°C and 50°C during the calibration process of the modules.

Additionally, an illumination level dependency of the timing resolution of CHEC-S has been observed. Despite this, the timing resolution still meets the requirement of a 2 ns timing resolution for illumination levels above 5 p.e..

9 Outlook

The proposed methods to counteract the temperature dependency of the transfer-functions have been tested on single modules. A test of these methods for the whole camera and their effects is still pending. Also the temperature dependency cannot be completely traced back to the Wilkinson-ramp. Other, not yet understood effects come into play. Next steps would include further testing of the data readout-chain to isolate all components (comparators, amplifiers, etc.) and effects that could contribute to the observed temperature dependency. Which in turn could lead to more accurate methods for removing said deviation. Also changes in the cooling design of CHEC-S should be investigated in the future. Reducing or removing the temperature gradient in the camera while in operation (compare Figure 10) increases the effectiveness of all correction methods investigated in this thesis or even renders them obsolete.

A Appendix

A.1 Amplitudes used for transfer-functions

The following amplitudes (in mV) where used for the function generator signal to record transfer-functions:
0, 6, 8, 12, 16, 20, 24, 28, 32, 36, 40, 48, , 56, 64, 72, 80, 88, 96, 104, 112, 120, 136, 152, 168, 184, 200, 216, 232, 248, 264, 280, 312, 344, 376, 408, 440, 472, 504, 536, 568, 600, 664, 728, 792, 856, 920, 984, 1048, 1112, 1176, 1240, 1368, 1496, 1624, 1752, 1880, 2008, 2136, 2264, 2392 and 2500.

A.2 Initial parameters for event fit

The start parameters for both Landau distributions used for the event fits can be found in Table 5 below. Here, "Amp" is the amplitude that has been set for the function generator.

Parameter	**Initial value**
0_{pos}	Amp $\cdot 11.0$
1_{pos}	45
2_{pos}	3.0
0_{neg}	Amp $\cdot -1.5$
1_{neg}	79
2_{neg}	6.5

Table 5: Start parameters for fit function used for event fits.

In Table 5 above the parameter name i_k consists of the parameter number in root i and and identifier k for which of the two landau distributions (positive and negative amplitude) it is used.

A.3 Amplitudes used for undershoot fit

Pulse amplitude [mV]	Undershoot amplitude [mV]
48	−10
112	−23
200	−41
280	−58
600	−128
1048	−217
1496	−310
1752	−363

Table 6: Amplitudes used for undershoot fit with corresponding amplitudes of the undershoot.

A.4 Temperature distribution inside the camera

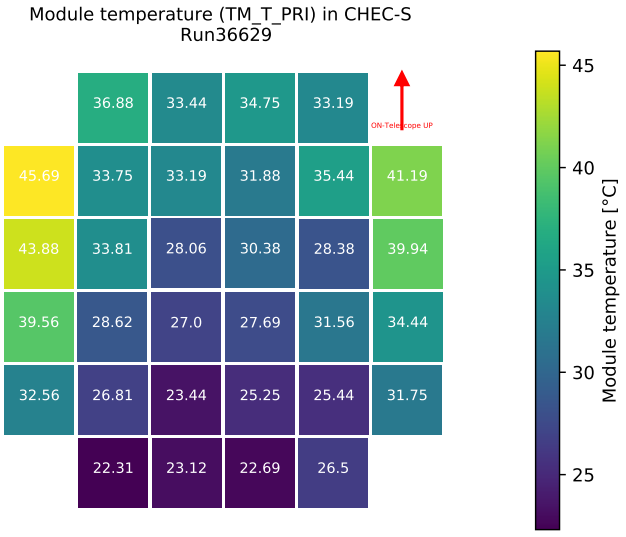

Figure 71: Temperature of TARGET-Modules for run 36629.

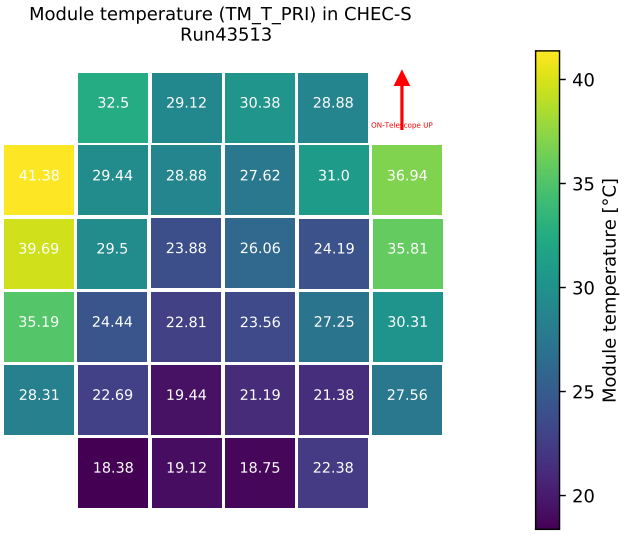

Figure 72: Temperature of TARGET-Modules for run 43513.

A.5 Deviation-plots for different channels of module SN0072

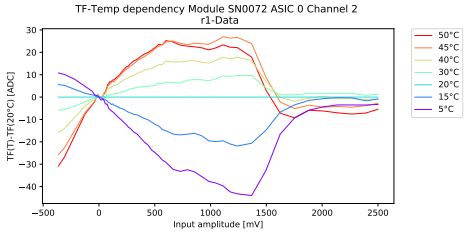

(a) Deviation SN0072 ASIC 0 channel 2.

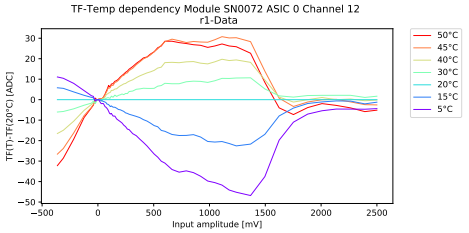

(b) Deviation SN0072 ASIC 0 channel 12.

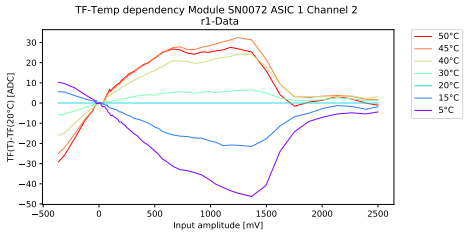

(c) Deviation SN0072 ASIC 1 channel 2.

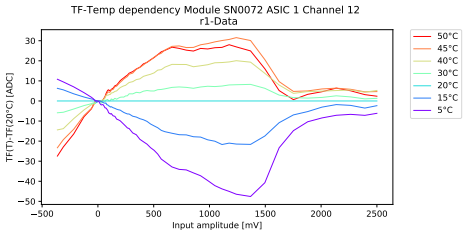

(d) Deviation SN0072 ASIC 1 channel 12.

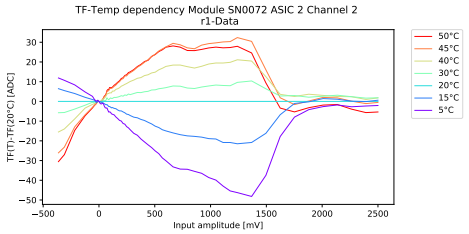

(e) Deviation SN0072 ASIC 2 channel 2.

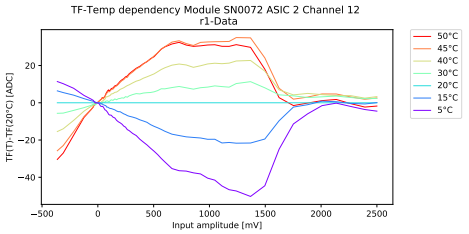

(f) Deviation SN0072 ASIC 2 channel 12.

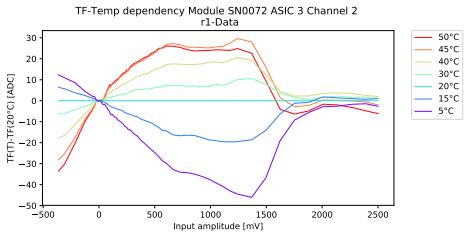

(g) Deviation SN0072 ASIC 3 channel 2.

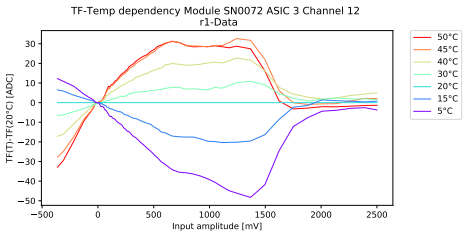

(h) Deviation SN0072 ASIC 3 channel 12.

Figure 73: Deviation of the mean transfer-function at a given temperature TF(T) from TF(20°C), the one recorded at the reference temperature, for module SN0072 for all ASICs and channels 2 and 12.

A.6 Deviation-plots for different modules

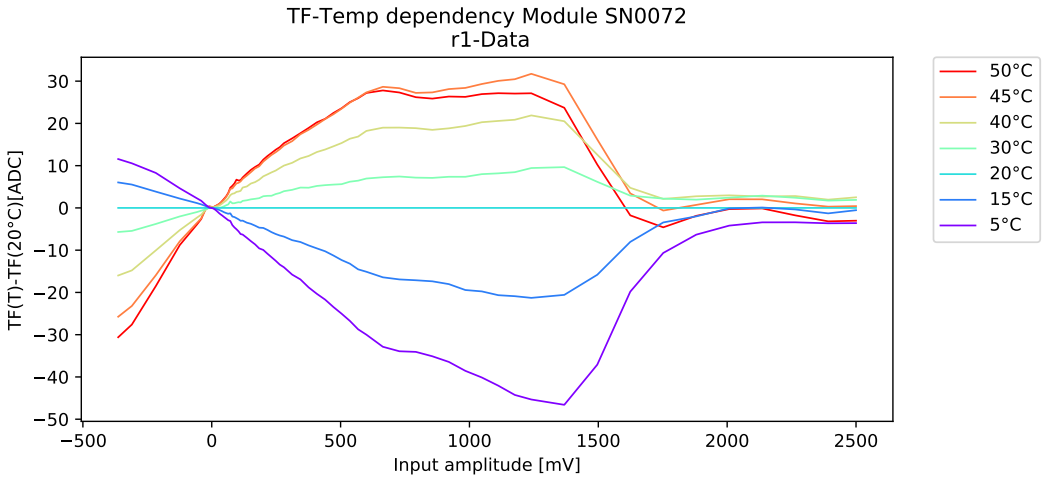

Figure 74: Deviation of the mean transfer-function at a given temperature TF(T) from TF(20°C), the one recorded at the reference temperature, for module SN0072.

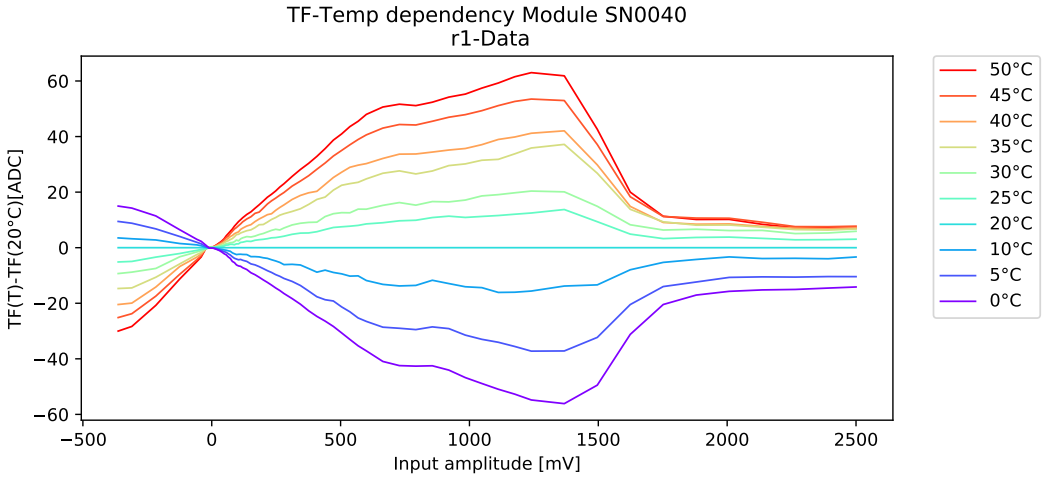

Figure 75: Deviation of the mean transfer-function at a given temperature TF(T) from TF(20°C), the one recorded at the reference temperature, for module SN0040.

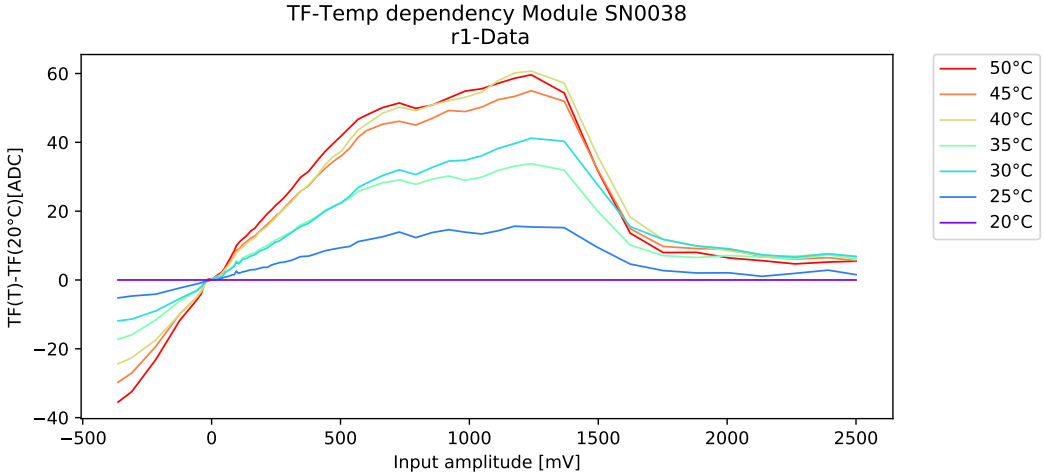

Figure 76: Deviation of the mean transfer-function at a given temperature TF(T) from TF(20°C), the one recorded at the reference temperature, for module SN0038.

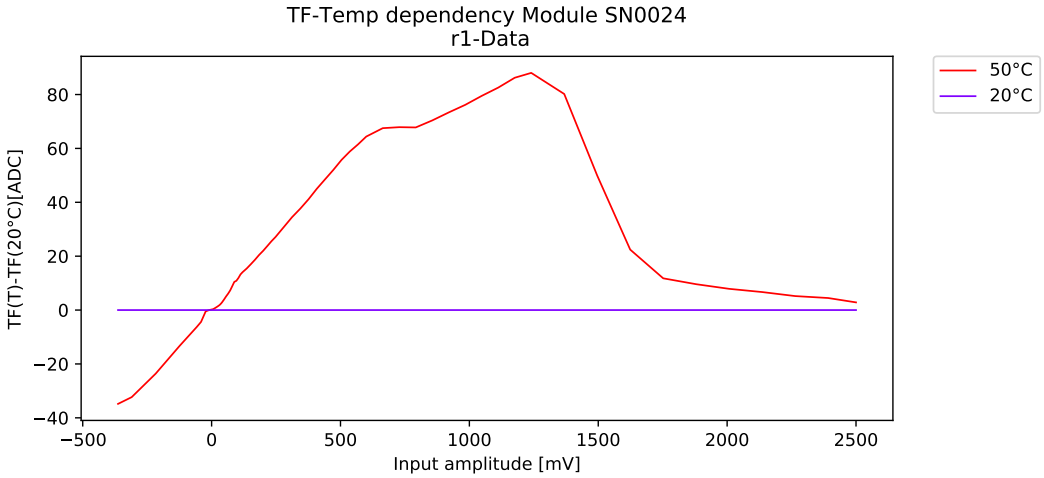

Figure 77: Deviation of the mean transfer-function at a given temperature TF(T) from TF(20°C), the one recorded at the reference temperature, for module SN0024.

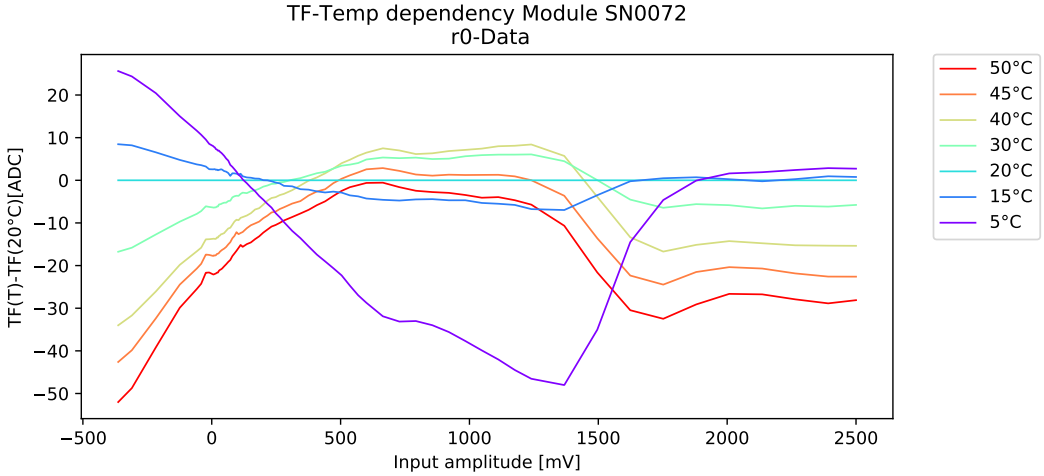

Figure 78: Deviation of the mean transfer-function at a given temperature TF(T) from TF(20°C), the one recorded at the reference temperature, for module SN0072 using r0-data.

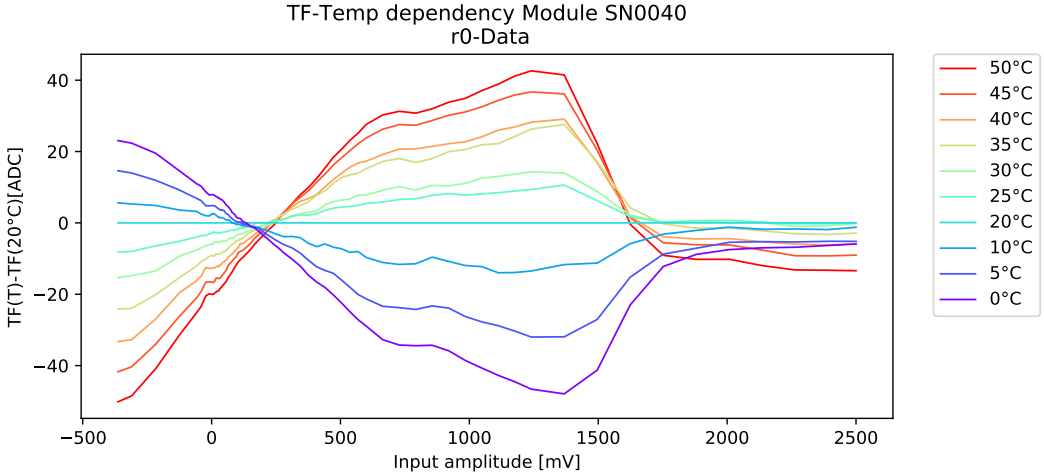

Figure 79: Deviation of the mean transfer-function at a given temperature TF(T) from TF(20°C), the one recorded at the reference temperature, for module SN0040 using r0-data.

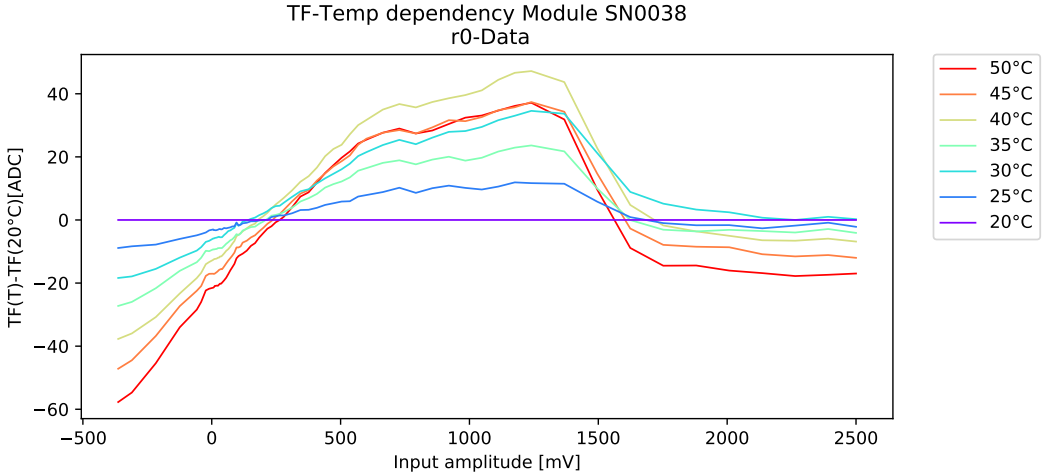

Figure 80: Deviation of the mean transfer-function at a given temperature TF(T) from TF(20°C), the one recorded at the reference temperature, for module SN0038 using r0-data.

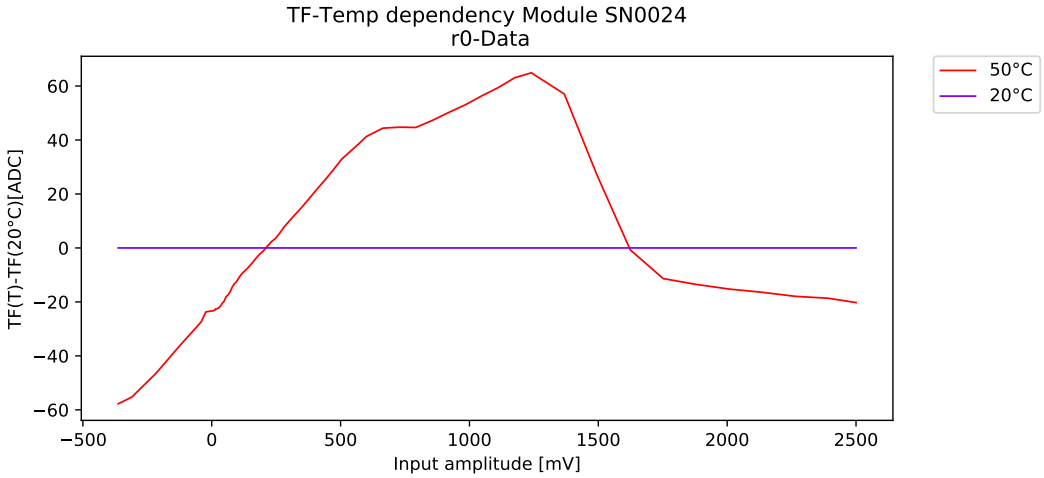

Figure 81: Deviation of the mean transfer-function at a given temperature TF(T) from TF(20°C), the one recorded at the reference temperature, for module SN0024 using r0-data.

A.7 Wilkinson-ramps of module SN0024

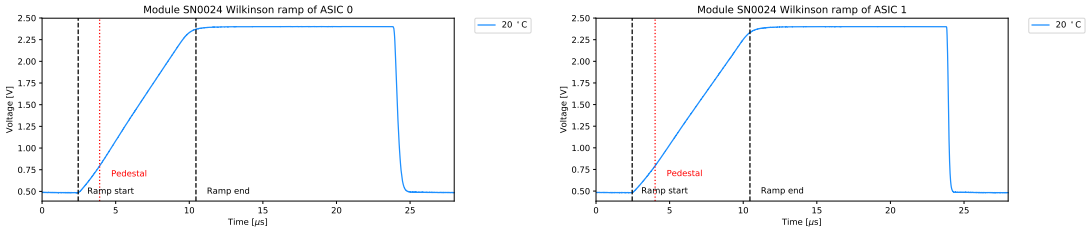

(a) SN0024 ASIC 0.

(b) SN0024 ASIC 1.

(c) SN0024 ASIC 2.

(d) SN0024 ASIC 3.

Figure 82: Second Wilkinson-ramp of module SN0024 ASIC 0-3 with start and end position of the ramp indicated.

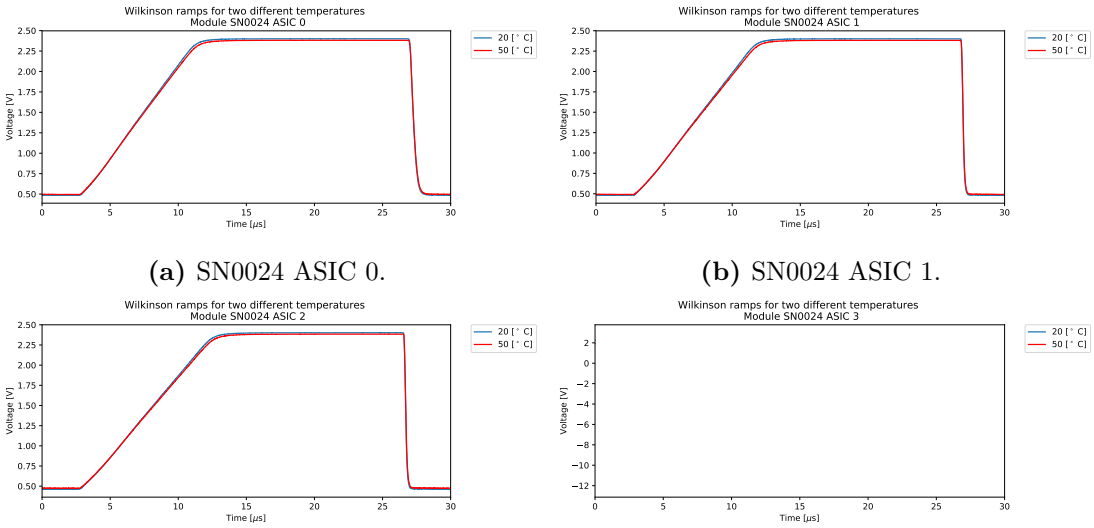

(a) SN0024 ASIC 0.

(b) SN0024 ASIC 1.

(c) SN0024 ASIC 2.

(d) SN0024 ASIC 3.

Figure 83: Second Wilkinson-ramp of module SN0024 ASIC 0-3 at 20°C and 50°C with corrected voltage values.

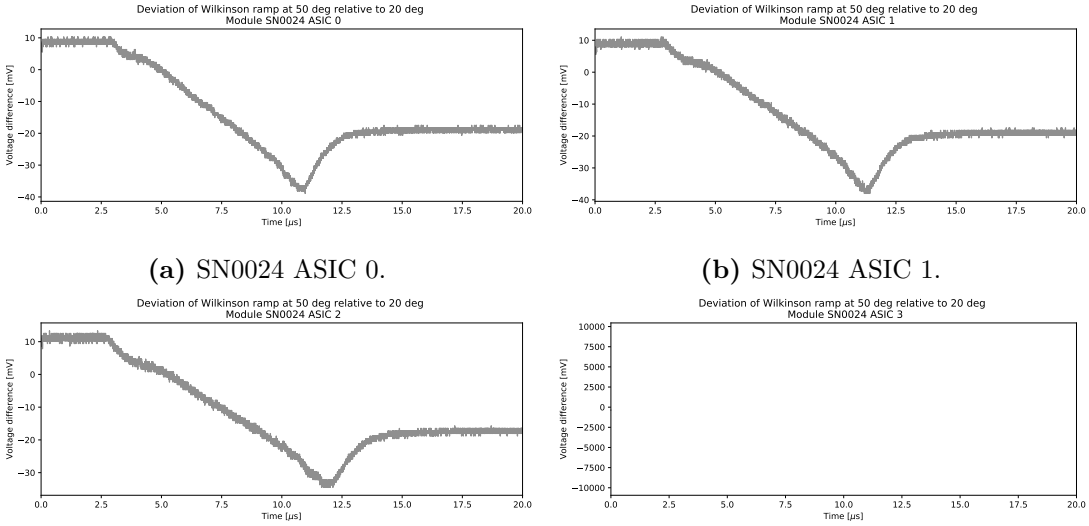

(a) SN0024 ASIC 0.

(b) SN0024 ASIC 1.

(c) SN0024 ASIC 2.

(d) SN0024 ASIC 3.

Figure 84: Difference between the Wilkinson-ramps for 50°C and 20°C of module SN0024 ASIC 0 with corrected voltage values.

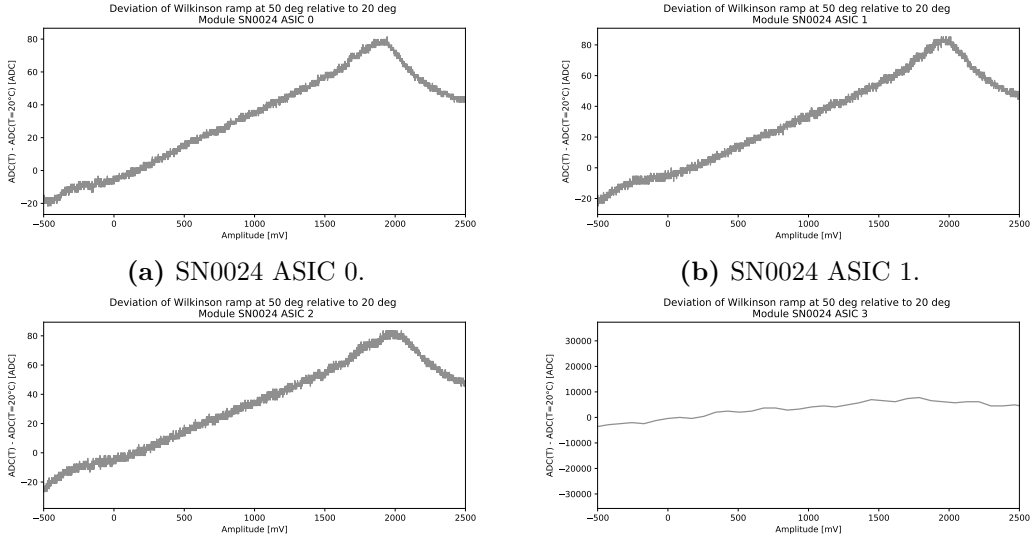

(a) SN0024 ASIC 0.

(b) SN0024 ASIC 1.

(c) SN0024 ASIC 2.

(d) SN0024 ASIC 3.

Figure 85: Difference between the Wilkinson-ramps for 50°C and 20°C of module SN0024 ASIC 0 with corrected voltage values. Rescaled to match axis of deviation plots.

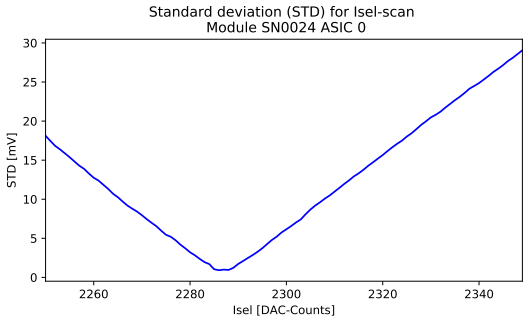

(a) SN0024 ASIC 0.

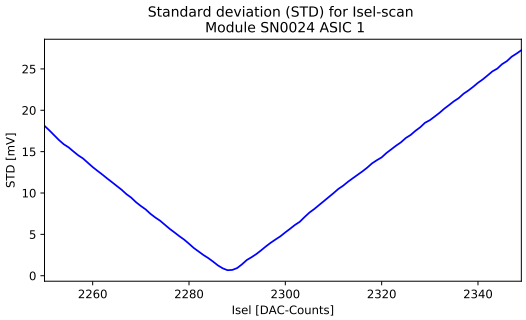

(b) SN0024 ASIC 1.

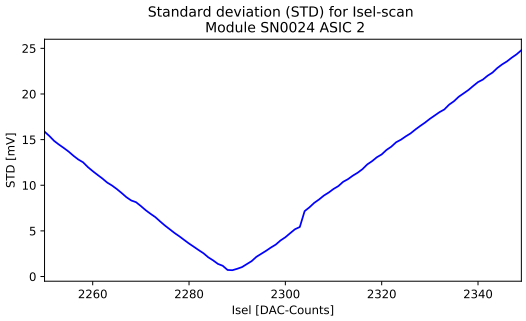

(c) SN0024 ASIC 2.

Figure 86: ISEL scan results for module SN0024 ASIC 0-2.

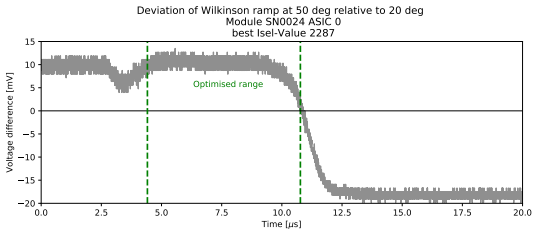

(a) SN0024 ASIC 0 ISEL 2287.

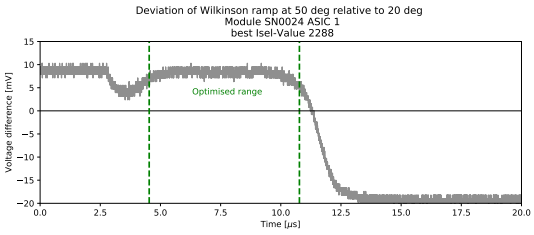

(b) SN0024 ASIC 1 ISEL 2288.

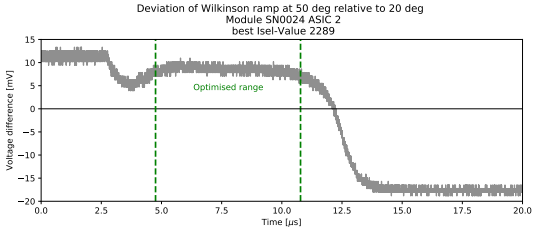

(c) SN0024 ASIC 2 ISEL 2289.

Figure 87: Difference between the Wilkinson-ramps for 50°C and 20°C of module SN0024 ASIC 0-2 with corrected voltage values and highlighted range used for optimization with VDIS 100.

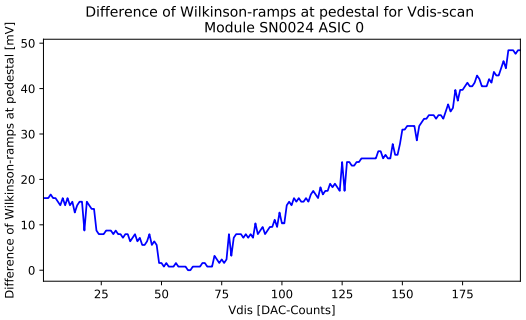

(a) SN0024 ASIC 0 ISEL 2287.

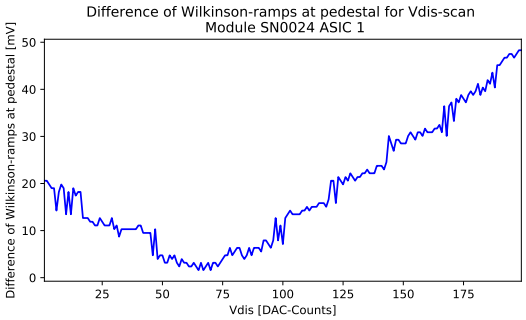

(b) SN0024 ASIC 1 ISEL 2288.

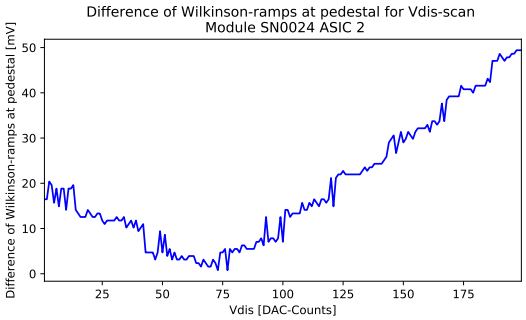

(c) SN0024 ASIC 2 ISEL 2289.

Figure 88: VDIS scan results for module SN0024 ASIC 0-2.

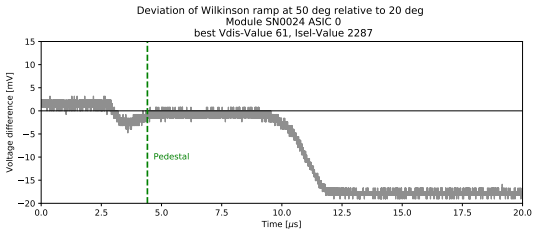

(a) SN0024 ASIC 0 ISEL 2287 VDIS 61.

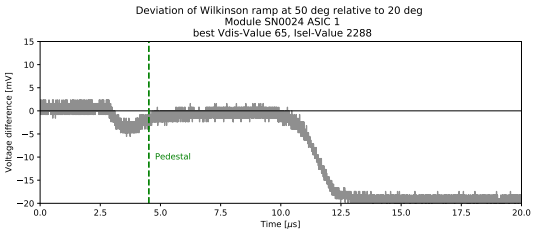

(b) SN0024 ASIC 1 ISEL 2288 VDIS 65.

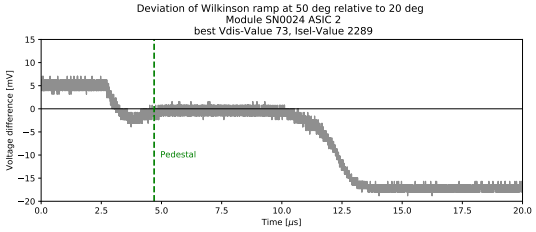

(c) SN0024 ASIC 2 ISEL 2289 VDIS 73.

Figure 89: Difference between the Wilkinson-ramps for 50°C and 20°C of module SN0024 ASIC 0-2 with corrected voltage values and highlighted position of pedestal. ISEL 2287 and optimized VDIS parameter.

References

[1] T. CTA Consortium, "Cherenkov Telescope Array: The Next Generation Gamma-ray Observatory," *arXiv e-prints*, Sept. 2017.

[2] S. Mangano, "Cherenkov Telescope Array Status Report," *arXiv e-prints*, May 2017.

[3] "Homepage of the CTA Observatory from 3rd January 2019." https://www.cta-observatory.org.

[4] M. S. Longair, *High Energy Astrophysics*. Cambridge University Press, third ed.

[5] O. Le Blanc, G. Fasola, J. M. Huet, R. White, A. Dmytriiev, H. Sol, A. Zech, A. Abchiche, J. P. Amans, T. P. Armstrong, M. Barcelo, D. Berge, A. M. Brown, G. Buchholtz, P. M. Chadwick, P. Clark, G. Cotter, L. Dangeon, F. De Frondat, P. Deiml, J. L. Dournaux, C. Duffy, S. Einecke, S. Flis, S. Funk, G. Giavitto, J. Gironnet, J. A. Graham, T. Greenshaw, J. A. Hinton, I. Jégouzo, M. Kraus, J. S. Lapington, P. Laporte, S. A. Leach, S. Lloyd, I. A. Minaya, R. Morier, A. Okumura, H. Prokoph, D. Ross, G. Rowell, C. B. Rulten, H. Schoorlemmer, J. Schmoll, S. T. Spencer, M. Stephan, R. Stuik, H. Tajima, J. Thornhill, L. Tibaldo, J. Vink, J. J. Watson, J. Williams, A. Zink, and J. Zorn, "Final characterisation and design of the Gamma-ray Cherenkov Telescope (GCT) for the Cherenkov Telescope Array," in *Ground-based and Airborne Telescopes VII*, vol. 10700 of *Society of Photo-Optical Instrumentation Engineers (SPIE) Conference Series*, p. 1070010, July 2018.

[6] D. Mazin, J. Cortina, M. Teshima, and t. CTA Consortium, "Large Size Telescope Report," *ArXiv e-prints*, Oct. 2016.

[7] S. Vercellone, "The next generation Cherenkov Telescope Array observatory: CTA," *Nuclear Instruments and Methods in Physics Research A*, vol. 766, pp. 73–77, Dec. 2014.

[8] C. Bigongiari and CTA Consortium, "The Cherenkov Telescope Array," *Nuclear and Particle Physics Proceedings*, vol. 279, pp. 174–181, Oct. 2016.

[9] J. Zorn, R. White, J. J. Watson, T. P. Armstrong, A. Balzer, M. Barcelo, D. Berge, R. Bose, A. M. Brown, M. Bryan, P. M. Chadwick, P. Clark, H. Costantini, G. Cotter, L. Dangeon, M. Daniel, A. De Franco, P. Deiml, G. Fasola, S. Funk, M. Gebyehu, J. Gironnet, J. A. Graham, T. Greenshaw, J. A. Hinton, M. Kraus, J. S. Lapington, P. Laporte, S. A. Leach, O. Le Blanc, A. Malouf, P. Molyneux, P. Moore, H. Prokoph, A. Okumura, D. Ross, G. Rowell, L. Sapozhnikov, H. Schoorlemmer, H. Sol, M. Stephan, H. Tajima, L. Tibaldo, G. Varner, and A. Zink, "Characterisation and testing of CHEC-M-A camera prototype for the small-sized telescopes of the Cherenkov telescope array," *Nuclear Instruments and Methods in Physics Research A*, vol. 904, pp. 44–63, Oct. 2018.

[10] A. M. Brown, A. Abchiche, D. Allan, *et al.*, "The GCT camera for the Cherenkov Telescope Array," in *Society of Photo-Optical Instrumentation Engineers (SPIE) Conference Series*, p. 99065K, July 2016.

[11] R. White, "CHEC: a Compact High Energy Camera for the Cherenkov Telescope Array," *Journal of Instrumentation*, vol. 12, p. C12059, Dec. 2017.

[12] S. Funk, D. Jankowsky, H. Katagiri, *et al.*, "TARGET: A Digitizing And Trigger ASIC For The Cherenkov Telescope Array," *ArXiv e-prints*, Oct. 2016.

[13] M. K. Daniel, R. J. White, D. Berge, J. Buckley, *et al.*, "A Compact High Energy Camera for the Cherenkov Telescope Array," *ArXiv e-prints*, July 2013.

[14] A. De Franco, R. White, D. Allan, *et al.*, "The first GCT camera for the Cherenkov Telescope Array," *ArXiv e-prints*, Sept. 2015.

[15] R. White, H. Schoorlemmer, and f. t. CTA GCT project, "A Compact High Energy Camera (CHEC) for the Gamma-ray Cherenkov Telescope of the Cherenkov Telescope Array," *arXiv e-prints*, Sept. 2017.

[16] L. Tibaldo, J. A. Vandenbroucke, A. M. Albert, *et al.*, "TARGET: toward a solution for the readout electronics of the Cherenkov Telescope Array," *ArXiv e-prints*, Aug. 2015.

[17] A. Zink. Personal information.

[18] J. Schaefer, "Parameter optimization of the T5TEA-ASIC for the Cherenkov Telescope Array."

[19] A. Albert, S. Funk, T. Kawashima, *et al.*, "TARGET 5: a new multi-channel digitizer with triggering capabilities for gamma-ray atmospheric Cherenkov telescopes," *ArXiv e-prints*, July 2016.

[20] A. N. Otte, J. Biteau, H. Dickinson, S. Funk, *et al.*, "Development of a SiPM Camera for a Schwarzschild-Couder Cherenkov Telescope for the Cherenkov Telescope Array," *ArXiv e-prints*, Sept. 2015.

[21] M. Kraus, "The Cosmic-Ray Electron Anisotropy Measured with H.E.S.S. and Characterization of a Readout System for the SST Cameras of CTA." `https://ecap.nat.fau.de/wp-content/uploads/2018/07/2018_Kraus_Dissertation.pdf`.

[22] "Fractional intensity resolution requirement for cta." `https://jama.cta-observatory.org/`. (Accessed on 06/03/2019).

[23] "Datasheet of LT3045EDD PMIC-Voltage regulator." https://www.analog.com/media/en/technical-documentation/data-sheets/3045fa.pdf.

Danksagung

Ich möchte mich hiermit bei all jenen Personen bedanken, die zu dem Erfolg dieser Arbeit beigetragen haben. Im speziellen gilt mein Dank den folgenden Personen:

- **Prof. Dr. Stefan Funk:** Für das Angebot dieses äußerst interessanten Themas.
- **Dr. Adrian Zink:** Für seine ständige Hilfsbereitschaft, seine Geduld mit mir und den interessanten Ausflügen zum MPIK.
- **Peter Deiml:** Für das freundliche hinweisen auf etliche Grammatik- und Rechtschreibfehler.
- **Jason Watson:** Für seine schnelle Antwortzeiten, bei Fragen zu bereitgestellten Skripten.
- **Meinen Kollegen:** Für die super Arbeitsatmosphäre und der stets guten Laune im Büro.
- **Meinen Eltern:** Für Ihre anhaltende und beispiellose Unterstützung während meines gesamten Studiums.

Erklärung

Hiermit bestätige ich, dass ich diese Arbeit selbstständig und nur unter Verwendung der angegebenen Hilfsmittel angefertigt habe.

Erlangen, den 12. 03. 2018